

Multi-scale modeling of bone remodeling

Dissertation

zur Erlangung des Grades
Doktor der Ingenieurwissenschaften (Dr.-Ing.)
der Naturwissenschaftlich-Technischen Fakultät III
Chemie, Pharmazie, Bio- und Werkstoffwissenschaften
der Universität des Saarlandes

vorgelegt von

Dipl.-Ing. Tobias Ebinger, M.Sc.

Saarbrücken

2009

Tag der Einreichung: 23.04.2009
Tag des Kolloquiums: 21.07.2009

Dekan: Prof. Dr.-Ing. Stefan Diebels
Gutachter: Prof. Dr.-Ing. Stefan Diebels
Prof. Dr. Eduard Arzt

Preface

The research work presented in this thesis was carried out at the Chair of Applied Mechanics at Saarland University.

To begin with, I would like to thank my doctoral adviser Professor Dr.-Ing. Stefan Diebels. When I was a student assistant at the Chair of Applied Mechanics at University of Stuttgart he already directed my attention to the numerical simulation of materials with inherent length scale. So I am grateful for the possibility to recess the investigations at Saarland University. The various ideas he put up for discussion have inspired and enriched this thesis.

Moreover, I would like to thank Professor Dr. Eduard Arzt for accepting to be co-referee of this thesis.

Furthermore, I would like to thank all the people who have in one way or the other contributed to this research. I thank all my colleagues for the good and encouraging collaboration. Especially I would like to mention Professor Dr.-Ing. Holger Steeb, who made a contribution to the thesis by a large number of discussions, Dr. med. Thorsten Tjardes providing CT data of the human femur and my student assistant Yassen Dobrev, who supported the work by preparing the CT data towards a useable Finite Element model.

Finally, I owe my family – especially my wife Miriam – a debt of gratitude for the encouragement and for the needful and appreciative support of the thesis.

Saarbrücken, April 2009

Tobias Ebinger

Abstract

The number of hip operations performed by inserting implants has continuously increased in recent years. In Germany 110 673 femoral head fractures of female persons were diagnosed in the year 2004. To minimize the surgical intervention, the femoral head is saved whenever possible and fixated by screws or nails. Thereby, the induced stiffness change leads to an adaptation of the material with respect to the new loading situation. The very same adaptation can cause a repeated failure of the femoral head.

The present work introduces a numerical model, which is able to anticipate the adaptation process so that it is possible to make a statement about the failure probability in advance. The model considers the anisotropy of the bone material as well as the influence of its microstructure.

The model will be implemented into two different Finite Element codes. Finally, the capability of the model is demonstrated on some numerical examples.

Zusammenfassung

Die Zahl der Hüftoperationen, bei denen Implantate eingesetzt werden, ist in den letzten Jahren kontinuierlich gestiegen. Allein in Deutschland wurde im Jahr 2004 bei 110 673 weiblichen Personen eine Oberschenkelhalsfraktur festgestellt. Um den chirurgischen Eingriff so gering wie möglich zu halten, wird – wenn möglich – der Femurkopf erhalten und mittels Schrauben oder Nägeln fixiert. Die dadurch implizierte Steifigkeitsänderung geht einher mit einer Anpassung des Materials bezüglich der neuen Belastungssituation. Eben diese Anpassung kann jedoch zu einem abermaligen Versagen führen.

Die vorliegende Arbeit stellt ein numerisches Modell vor, das in der Lage ist, die Anpassung zu antizipieren, so dass sich bereits im Vorfeld Aussagen über die Versagenswahrscheinlichkeit machen lassen. Das Modell berücksichtigt dabei sowohl die Anisotropie als auch die Mikrostruktur des Knochenmaterials.

Dieses Modell wird in zwei unterschiedlichen Finite Elemente Codes umgesetzt. Abschließend demonstrieren einige Beispiele die Leistungsfähigkeit des Modells.

Contents

1	Introduction	1
2	Biomechanical background	7
2.1	Bone morphology	7
2.2	Remarks on bone remodeling in adulthood	9
2.3	Historical review of adaptive bone remodeling	10
3	Continuum theories	13
3.1	<i>Cauchy</i> continuum theory	14
3.2	<i>Cosserat</i> continuum theory	18
4	Beam theories	25
4.1	<i>Euler-Bernoulli</i> beam theory	26
4.2	<i>Timoshenko</i> beam theory	28

5	FE² approach	31
5.1	FE ² approach using FOH	34
5.1.1	Projection	35
5.1.2	Homogenization	40
5.2	FE ² approach using SOH	44
5.2.1	Projection	45
5.2.2	Homogenization	48
6	Application to bone remodeling	51
6.1	Growth, remodeling and morphogenesis	51
6.2	Remodeling	53
6.3	Reorientation	55
7	Numerical implementation	59
7.1	Two-dimensional implementation (SOH)	60
7.1.1	Remodeling	60
7.1.2	Reorientation	61
7.2	Three-dimensional implementation (FOH)	65
7.2.1	Remodeling	65
7.2.2	Reorientation	66

<i>CONTENTS</i>	iii
8 Numerical examples	69
8.1 Numerical examples calculated by PANDAS	69
8.1.1 Comparison of ansatz functions	71
8.1.2 Influence of parameters on boundary layer effect	80
8.1.3 The influence of the initial conditions	86
8.1.4 Interaction of model with inserted screw	92
8.2 Numerical examples calculated by LS-DYNA	95
8.2.1 Check of adaptation process	97
8.2.2 Check of boundary layer effect and size effect	100
8.2.3 Check of mesh independency	105
8.2.4 Application to model geometry	109
8.2.5 Sketch of including CT data	113
9 Conclusion	117
9.1 Summary	117
9.2 Future work	120

List of Figures

2.1	Physis of bone	8
3.1	Kinematics of <i>Cauchy</i> continuum theory	14
3.2	<i>Tonti</i> diagram of <i>Cauchy</i> continuum theory	17
3.3	Kinematics of <i>Cosserat</i> continuum theory	18
3.4	<i>Tonti</i> diagram of <i>Cosserat</i> continuum theory	23
4.1	Kinematics of <i>Euler-Bernoulli</i> beam theory	26
4.2	<i>Tonti</i> diagram of <i>Euler-Bernoulli</i> beam theory	27
4.3	Kinematics of <i>Timoshenko</i> beam theory	28
4.4	<i>Tonti</i> diagram of <i>Timoshenko</i> beam theory	29
5.1	Basic idea of FE^2 approach	33
5.2	Attached microstructure in first order homogenization	35
5.3	Internal and external boundaries of beam elements	37

5.4	Deformation modes in first order homogenization	40
5.5	Tonti diagram of FE ² approach using FOH	43
5.6	Attached microstructure in second order homogenization	45
5.7	<i>Cosserat</i> deformation mode	47
5.8	Split of <i>Cosserat</i> deformation mode	48
6.1	Circumferential growth and atrophy	57
6.2	Rotational update	58
7.1	Case differentiation for orientation update	62
8.1	Boundary value problem of shear test	73
8.2	Numerical results of reference solution	74
8.3	Absent axial symmetry of thickness change d_1 and d_2	74
8.4	Numerical results of τ at cutting line	76
8.5	Numerical results of τ at cutting line (detail)	76
8.6	Numerical results of \overline{M}_{32} at cutting line	77
8.7	Numerical results of \overline{M}_{32} at cutting line (detail)	77
8.8	Numerical results of δ at cutting line	79
8.9	Numerical results of δ at cutting line (detail)	79
8.10	Numerical results of φ^{TVE} at cutting line	80

8.11	Different load carrying behavior of microstructures	82
8.12	Boundary layer effect scaling size of TVE (l/δ constant)	83
8.13	Boundary layer effect scaling length l (δ constant)	84
8.14	Boundary layer effect scaling thickness δ (l constant)	85
8.15	Converged solutions for different initial orientations	88
8.16	Converged solutions for different initial thicknesses	89
8.17	Comparison of principal directions	90
8.18	Boundary value problem of shear test (Neumann BC)	90
8.19	Converged solutions for different initial thicknesses (stress BC)	91
8.20	Boundary value problem of pull out test	92
8.21	Converged solutions for different thread depths	94
8.22	Boundary value problem for testing of the adaptation process	98
8.23	Adaptation: reorientation	99
8.24	Adaptation: thickness change and stimuli	101
8.25	Boundary value problem for investigation of size effects	102
8.26	Influence of geometrical scaling	106
8.27	Boundary value problem for investigation of size effects	107
8.28	Average beam thickness plotted for different discretizations	108
8.29	Average beam thickness of cubic domain	108

8.30	Boundary value problem of model geometry	110
8.31	Three-dimensional model	111
8.32	Numerical results of model geometry ($\alpha_P = 30^\circ$)	112
8.33	Distribution of Hounsfield Unit (HU)	115
8.34	FE model of human femur	116

Chapter 1

Introduction

The macroscopic behavior of porous materials, e. g. foams, geomaterials as well as biological tissues like cancellous bone, is strongly influenced by the microstructure related to the pore space [38, 39]. It is well known that these materials cannot be described by a standard continuum mechanical setting on the macroscale neglecting the internal architecture of the microstructure. Such materials with inherent length scale show boundary-layer effects leading to size effects, i. e. increasing stiffness of specimens for shrinking size, cf. [19, 53], or vice versa decreasing stiffness for shrinking size, cf. [65, 64, 78].

In the 1960s the relation of lattice materials to macroscopic *Cosserat* formulations was already shown [1, 2, 28] and was e. g. a point of discussion at the IUTAM symposium at Freudenstadt (Germany) in 1967. In this framework homogenization procedures were proposed in order to link the discrete microstructure of the porous solid material to the extended continuum formulation, cf. [19, 31, 32, 79] and for granular material [6, 18, 24].

On the one hand open-cell foams, including cancellous bone, may be described by beam models on the microscale which give insight into the governing deformation mechanisms, e. g. [65, 66], but on the other hand these microscopic models become numerically inefficient for large structures due

to the large number of degrees of freedom (DOF). Models directly based on the voxel mesh derived by μ CT [4, 47, 61, 69, 74] are numerically even more expensive and therefore usually limited to dimensions much smaller than the dimensions of clinical interest, e. g. in case of a complete femur. Effective properties corresponding to the microscopic beam model can be obtained by homogenization procedures. In this case averages of the forces and moments in the beams are computed either analytically [36, 65] or numerically [44] leading to macroscopic expressions for stress- and strain-like quantities. E. g. considering the standard *Cauchy* continuum theory, the stress- and strain-like quantities are the stress tensor and the strain tensor while for the *Cosserat* continuum theory there are in addition the couple stress tensor and the curvature tensor. Usually symmetry assumptions are incorporated which correspond to a specimen of infinite extension and, therefore, do not allow to take the boundary layers and size effects into account [45]. These effects are only included if the homogenization is carried out on a volume element which is of small size and not representative for the whole specimen. That means that the volume element is either representative in a weak sense only requiring local periodicity [75] or the volume element is a so-called Testing Volume Element (TVE) [46] completely without any requirements with regard to periodicity. For both types of volume elements stresses of higher order, the so-called couple stresses, have to be taken into account [20], which again require an extended continuum mechanical setting on the macroscale, e. g. a *Cosserat* or couple stress model.

An application of the couple stress model to the remodeling simulation of cancellous bone can be found in [3]. The extended macroscopic continuum theory depends on the implementation of the microscopic beam formulation: within the couple stress theory it is the implementation of the *Euler-Bernoulli* beam formulation, which is from a kinematical point of view the one-dimensional reduction of the general three-dimensional case (rotations are calculated as the derivative of the displacement field). Within the *Cosserat* theory it is the implementation of the *Timoshenko* beam formulation, which can be derived by one-dimensional reduction of the three-dimensional *Cosserat* element (rotations cannot be calculated as the derivative of the displacement field only due to extra rotations). Mixing up of both theories yields unreasonable results due to different interpretation of the rotational field [20]. Thus, the couple stress theory may only be applied in case of slender beams corresponding to slender trabeculae while the *Cosserat* theory also works for more compact

beams.

On the one hand, macroscopic models allow for computations on a large engineering scale, see e. g. [10, 14, 50, 51, 62, 68], but on the other hand, the formulation of the constitutive equations and especially the determination of the material parameters is still problematic. Therefore, the homogenization approach in combination with a macroscopic finite element computation delivers a promising alternative. As mentioned before, the homogenization can be carried out either numerically or analytically. However, the more complex the microstructure is the more difficult it is to find an analytical solution without any restrictions and simplifications for the microstructure as outlined by Adachi et al. [3]. Thus, in the present study the macroscopic finite element computation is combined with the numerical homogenization. This approach is known as FE^2 [29, 35, 49]. *Ebinger* et al. [21, 22] applied this approach in the framework of a *Cosserat* continuum. They showed that the boundary-layers and size effects described by the standard linear elastic constitutive equations of the *Cosserat* model are captured by the FE^2 approach.

In the present contribution the FE^2 approach is applied to hard biological tissues like cancellous bone. In order to include phenomena like growth and remodeling of bones, a simple growth model is applied on the microscale. Therefore, the beams of the underlying microstructure may increase their thickness according to a mechanical stimulus. This model draws from the macroscopic models of growth developed in the framework of thermodynamics of open systems, cf. [14, 50, 51, 62]. Typically these models allow for a mass production term which is responsible for the growth process. In the present model, anisotropic information is automatically included in a natural way due to the anisotropic arrangement of the beams in the microstructure. That means that the anisotropic information is not included in the form of a structural tensor or fabric tensor as done by other authors [58, 59, 81]. Furthermore, remodeling phenomena are included by evolving principal directions of the anisotropic microstructure, i. e. by the reorientation of the microstructural elements. The present model is a phenomenological one which does not distinguish between different types of microstructures like open cell structures, plated structures and prismatic structures [36, 68]. However, the microstructure is able to represent all types mentioned, whereby large unrealistic beam diameters indicate that the open cell structure will transform

into a plated or even a prismatic one.

The goal of the present contribution is to discuss the influence of higher order effects on the remodeling and adaptation of cancellous bone. Remodeling in bones occurs for instance after prosthetic operations. A negative consequence of an implanted prosthesis is a disturbance of the bio-mechanical equilibrium state. Thus, the system of the bone-microstructure and the artificial prosthesis are remodeled and adapted to the loading conditions. It is obvious, that the overall remodeling process strongly depends on the type of the disturbance or, to be more precise, on the change of stiffness of the bone-implant system. Clearly, a new equilibrium state will be obtained after the rebuilding time and this state depends on the prosthetics and the inherent loading transfer. From a general point of view, the basic concept of mechanically stimulated bone adaptation has been understood for a long time and traces back to the famous work of *Wolff* [80] and *Roux* [73] in the 19th century. Nevertheless, the underlying mechanisms, i. e. the interaction of the osteocyte network, the bone-forming osteoblasts and the bone-resorbing osteoclasts, and furthermore, the biochemical processes which "drive" the cells were unknown at that time and up to now have not completely been understood, cf. *Frost* [34].

With respect to the large amount of implants (750 000 hip implant operations have been necessary worldwide in 1993, cf. [5]) it becomes more and more important to understand and predict the remodeling process in bones. In this context, we also have to mention fracture-like accidents of osteoporethic patients (e. g. fractures of the neck of the femur, fractures of the body of vertebra etc.).

The thesis is organized as follows: after an introduction and an overview over different approaches for the numerical simulation of bone remodeling in chapter 1, chapter 2 gives an introduction into basic bone biology presenting the essential terms with respect to bone remodeling. The description of bone morphology is followed by a description of bone morphogenesis. Due to the special application in mind, i. e. the remodeling induced after prosthetic operations, it is followed by some general remarks on bone remodeling in adulthood. The chapter closes with a short historical review of adaptive bone remodeling from the first systematic observations up to the present.

The FE^2 approach, presented in chapter 5, can be understood as an extension of classical continuum theories. Therefore a short survey of the continuum theories used in the following is given in the third chapter, namely the *Cauchy* continuum theory and the *Cosserat* continuum theory.

Due to the difficulty in the formulation of macroscopic constitutive equations when considering the spongy bone as a homogeneous material, the trabecular microstructure of bone can be approximated by beam structures. Thus, chapter 4 gives a short survey of classical beam theories, the *Euler-Bernoulli* beam theory and the *Timoshenko* beam theory.

Combining the advantages of a macroscopic formulation, which considers the material as homogeneous, with the advantages of a microscopic formulation using beam elements, in which case it is much easier to formulate constitutive equations, chapter 5 presents the FE^2 approach. This approach is an extension of the classical continuum theories. Within the approach the constitutive equations are replaced by a projection of information from macro- to microscale, microscopic constitutive equations and a homogenization procedure transferring the microscopic information back to the macroscale. Due to the strong influence of the macroscopic continuum theory in mind on the FE^2 approach, the approach is presented based on a *Cauchy* continuum theory as well as based on a *Cosserat* continuum theory.

Chapter 6 deals with the application of the FE^2 approach to bone remodeling.

Chapter 7 is concerned with the numerical implementation of the adaptation processes. Again the implementation is presented separately for the two continuum theories under investigation.

Chapter 8 presents some numerical examples demonstrating the capability of the model with respect to bone remodeling.

Finally, the thesis closes with a summary and an outlook towards further steps needed to make the model suitable for the clinical daily routine.

Chapter 2

Biomechanical background

In this chapter an introduction of basic bone biology is presented introducing the essential terms with respect to bone remodeling. First a description of bone morphology (form and structure) will be given, to be continued by a description of bone morphogenesis (embryologic development of structure). Due to the special application in mind, i. e. the remodeling induced after prosthetic operations, it is followed by some general remarks on bone remodeling in adulthood. The chapter closes with a short historical review of adaptive bone remodeling from the first systematic observations up to the present.

2.1 Bone morphology

In general, the anatomy of a long bone like the human femur is described in terms relative to the physis, which is a bony scar remaining after skeletal maturity is reached and the growth plate has closed. The region between the physis and the end of the bone is referred to as the epiphysis. The other side of the physis, the distal side of the proximal physis and the proximal side of the

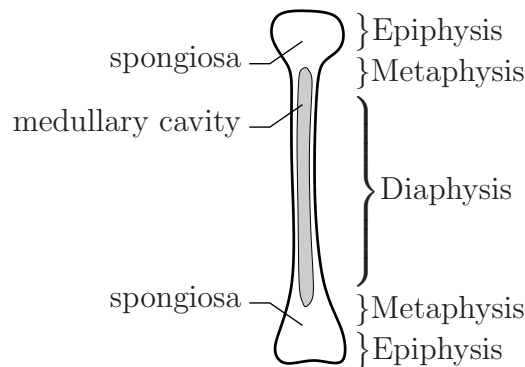


Figure 2.1: Physis of bone

distal physis, is called the metaphysis. The remaining region of bone between the proximal and distal metaphysis of a long bone is called the diaphysis. The boundary between the metaphysis and diaphysis is demarcated by a morphological transition from primarily cancellous bone in the metaphysis to primarily cortical bone in the diaphysis. The regions are shown in Fig. 2.1.

Bone as a material can be classified based on observations on different length scales.

On the highest level bone can be classified according to the architecture into cortical bone (compacta) and cancellous bone (spongiosa). Cortical bone is distinguished by a porosity lower than 15 % while the porosity of cancellous bone is in the range of 50 % up to 90 %. Cancellous bone has an open-celled porous structure and is found in long bones primarily in the epiphyseal and metaphyseal regions. The empty space between the individual spiculae, referred to as trabeculae, is filled with red bone marrow generating red blood cells (erythrocytes).

On a smaller level bone exhibits two different forms of ultrastructure: the lamellar bone and the osteonal bone.

On the cellular scale three different kind of cells can be observed being important with respect to bone remodeling. The basic cellular component of mature adult bone is the osteocyte. The osteocyte is responsible for the

exchange of constituents between bone matrix and surrounding fluid. The osteoblasts provide for the apposition of bone. The apposition is accomplished by the osteoblast forming the various organic components of bone matrix, mostly collagen, and secreting them through the cell wall. The third group of cells are the osteoclasts being responsible for bone resorption. By fixation to the bone to be resorbed, the bone matrix becomes convoluted so that the extra cell surface area enables the required secretion of enzymes breaking down the extracellular matrix.

Bone is composed of many different substances falling into the two categories of organic and inorganic materials. The two primary organic components are collagen fibers and an amorphous ground substance which holds the collagen in place as it mineralizes. In the case of bone, the collagen fibers are embedded in an inorganic crystalline material made up of primarily calcium and phosphate. Although the exact chemical composition may exhibit a degree of variation, it is widely accepted to be similar in form to hydroxyapatite ($Ca_{10}(PO_4)_6(OH)_2$). The information about the composition of bone is used in quantitative computer tomography (qCT) to relate the *Hounsfield* unit (HU) distribution towards the bone mineral density (BMD). Thereby, the HU is a measure for the X-ray absorption in computer tomography.

2.2 Remarks on bone remodeling in adulthood

Even after the pubertal growth spurt has been completed, osteoblasts and osteoclasts are still active and continue to form new bone while old bone is resorbed. The purpose of this metabolically expensive activity is subject of research. However, one suggestion is that old bone gradually becomes dehydrated and needs to be replaced, another suggestion is that the accumulation of damage in form of micro cracks diminishes the bone material properties until replacement with new bone is required. Independent of the real underlying purpose one can say that from a mechanical point of view the material properties are improved with respect to the individual loading conditions by

bone resorption followed by new bone formation.

On a macroscopical phenomenological level the apposition and resorption processes are regulated by mechanical loading, allowing bone to adapt its structure in response to the mechanical demands it experiences. In principle there are two possibilities for adaptation. The first one is by altering the external shape of the bone to suit the loading environment, the other one by altering the internal structure taking place on the trabecular surface of cancellous bone or on the haversian canals of cortical bone. Corresponding to the terminology of *Frost* [33] the former is called surface remodeling, external remodeling or modeling while the latter one is called internal remodeling or simply remodeling. Although both types of adaptation are active at the same time, the current work is restricted to considerations of internal remodeling.

2.3 Historical review of adaptive bone remodeling

The following section presents a literature review of the state of the art continuum models describing the remodeling behavior of bone. For a better understanding historical fundamental papers directly influencing the continuum formulations are presented in addition. Increasing power of computers allows for the simulation of bone remodeling based on the voxel geometry resolving the microstructure. However, such models being continuous only on a smaller scale than the macroscopic scale remain out of consideration.

The first systematical investigation of the mechanical influence on trabecular structure traces back to the Swiss anatomist *von Meyer* [60]. His drawings of the internal trabecular structure were studied by the German civil engineer *Culman*, who has got similar patterns by analyzing the principal stress trajectories of a *Fairbairn* crane, also called *Culman's crane* [16]. *Wolff* formulated the idea of trabecular alignment regulated by stress trajectories in what he termed the trajectorial theory [80]. As a consequence of the theory the trabeculae cross each other perpendicular, which was in contradiction

to the drawings of *von Meyer*. Incorporating the ideas of *Wolff* into his theory *Roux* generalized the observation towards what he called 'functional adaptation' of biologic structures and organs by 'adaptation of an organ to its function by practicing the latter' [73]. Starting from the ideas of *Roux*, *Pauwels* tried to quantify the functional demands leading to bone hypertrophy or atrophy in terms of the stress level [67]. He assumed the existence of an optimal stress level, which has to be present in the bone tissue to ensure a balanced state of bone resorption and deposition. A stimulus exceeding this optimal value will lead to increasing osteoblastic activity, which will then giving rise to bone hypertrophy. Vice versa values below the optimal value will lead to bone atrophy. *Kummer* contributed to the investigation of bone remodeling by a photoelastic model of the proximal femur yielding a better understanding of the trajectorial nature of bone [52]. *Frost* presented a different bone remodeling theory being able to explain clinical results [34] which show the tendency that fractured long bones healing in a bent configuration straighten out during long-term usage. This model was later on reformulated in terms of strain gradients by *Martin* and *Burr* [57].

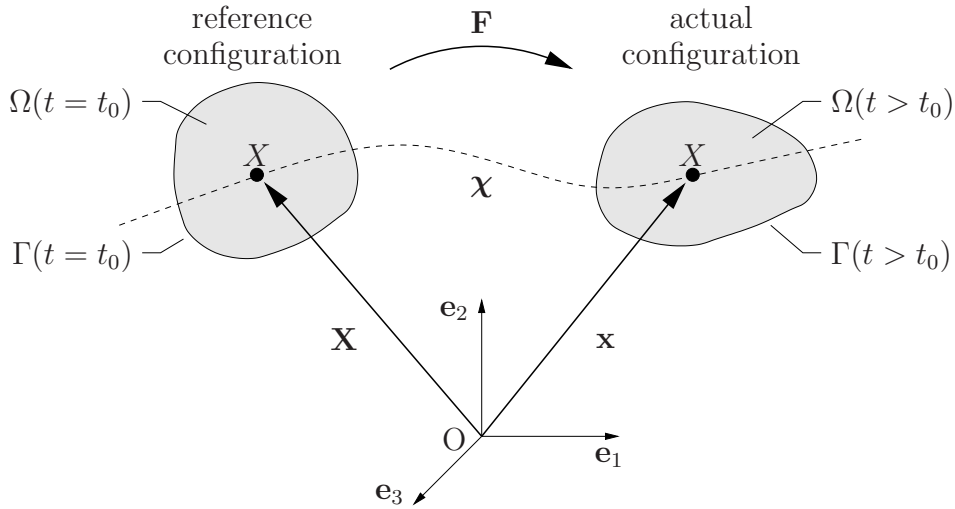
The first continuum model for bone adaptation to mechanical loading was the (phenomenological) theory of adaptive elasticity due to *Cowin* and *Hegedus* [14], *Hegedus* and *Cowin* [42] and *Cowin* and *Nachlinger* [15]. From *Cowin's* point of view [13], the greatest success was the development of a thermodynamic open-system model of tissue adaptation. This model has been followed, or assumed as a starting point, by most subsequent models of tissue adaptation. A survey of these models can be found in [41].

Chapter 3

Continuum theories

The FE² approach, presented in chapter 5, can be understood as an extension of classical continuum theories. Therefore a short survey of the continuum theories used in the following is given in this chapter. Thereby, apart from the constitutive equations (CE), all further equations – namely the balance equations (BE), kinematical equations (KE) and boundary conditions (BC) – will be used later in the framework of the FE² concept.

Due to the special application of the model in mind – the application with respect to bone remodeling, where the processes are relatively slow so that they may be considered as quasi-static – dynamic effects are eliminated from the equations by restricting the equations to the quasi-static case. Furthermore, the present work concentrates on the deformation up to failure. In this range the deformations are relatively small so that the following equations are restricted to small deformations.

Figure 3.1: Kinematics of *Cauchy* continuum theory

3.1 *Cauchy* continuum theory

Within the *Cauchy* continuum theory (also called standard continuum theory) the smallest observed entity is the material point X . The material point is able to reflect the physical properties and it is represented by a mathematical point.

The spatial deformation map χ assigns a one-to-one position \mathbf{x} in the actual configuration at time $t > t_0$ to each point X of the reference configuration with position \mathbf{X} at time $t = t_0$, see Fig. 3.1,

$$\mathbf{x} = \chi(\mathbf{X}, t), \quad \mathbf{X} = \chi(\mathbf{X}, t_0). \quad (3.1)$$

The deformation gradient \mathbf{F} maps a line element $d\mathbf{X}$ of the reference configuration into a line element $d\mathbf{x}$ of the actual configuration

$$d\mathbf{x} = \mathbf{F} \cdot d\mathbf{X} \quad (3.2)$$

resulting in the definition of the deformation gradient

$$\mathbf{F} = \frac{\partial \mathbf{x}(\mathbf{X}, t)}{\partial \mathbf{X}}. \quad (3.3)$$

The kinematics of the *Cauchy* continuum theory is presented in Fig. 3.1.

Introducing the displacement field \mathbf{u} as the difference between the position vectors of actual and reference configuration,

$$\mathbf{u} = \mathbf{x} - \mathbf{X}, \quad (3.4)$$

the deformation gradient \mathbf{F} can be stated in dependency of the displacement field \mathbf{u} by

$$\mathbf{F} = \mathbf{I} + \text{Grad } \mathbf{u} \quad (3.5)$$

using the abbreviation

$$\text{Grad}(\bullet) = \frac{\partial(\bullet)}{\partial \mathbf{X}}. \quad (3.6)$$

Strain tensors are defined by the difference of scalar products of line elements with respect to actual and reference configuration. The *Green-Lagrangean* strain tensor \mathbf{E} is defined by

$$d\mathbf{x} \cdot d\mathbf{x} - d\mathbf{X} \cdot d\mathbf{X} = d\mathbf{X} \cdot 2\mathbf{E} \cdot d\mathbf{X} \quad (3.7)$$

leading to the expression

$$\mathbf{E} = \frac{1}{2} (\mathbf{F}^T \mathbf{F} - \mathbf{I}). \quad (3.8)$$

Linearization of the equation yields the linearized strain tensor $\boldsymbol{\varepsilon}$

$$\boldsymbol{\varepsilon} = \text{sym}(\text{Grad } \mathbf{u}) = \frac{1}{2} (\text{Grad } \mathbf{u} + \text{Grad}^T \mathbf{u}). \quad (3.9)$$

The balance of momentum in the quasi-static case neglecting body forces reads

$$\text{div } \mathbf{T} = \mathbf{0}, \quad (3.10)$$

while the balance of moment of momentum yields the symmetry of the *Cauchy* stress tensor, $\mathbf{T} = \mathbf{T}^T$.

Furthermore, the *Dirichlet* and *Neumann* boundary conditions have to be fulfilled on the according boundaries

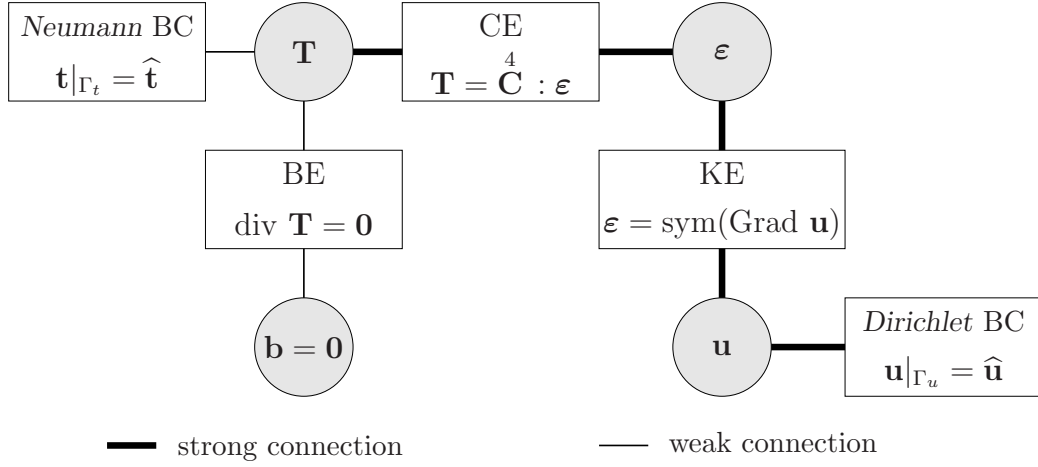
$$\mathbf{u}|_{\Gamma_u} = \widehat{\mathbf{u}} \text{ on } \Gamma_u, \quad \mathbf{t}|_{\Gamma_t} = \widehat{\mathbf{t}} \text{ on } \Gamma_t, \quad \Gamma_u \cup \Gamma_t = \Gamma, \quad \Gamma_u \cap \Gamma_t = \emptyset, \quad (3.11)$$

whereby \mathbf{t} is the force vector, which is related to the stress tensor \mathbf{T} by the Cauchy theorem

$$\mathbf{t} = \mathbf{T} \cdot \mathbf{n}. \quad (3.12)$$

\mathbf{n} is the outward directed normal vector.

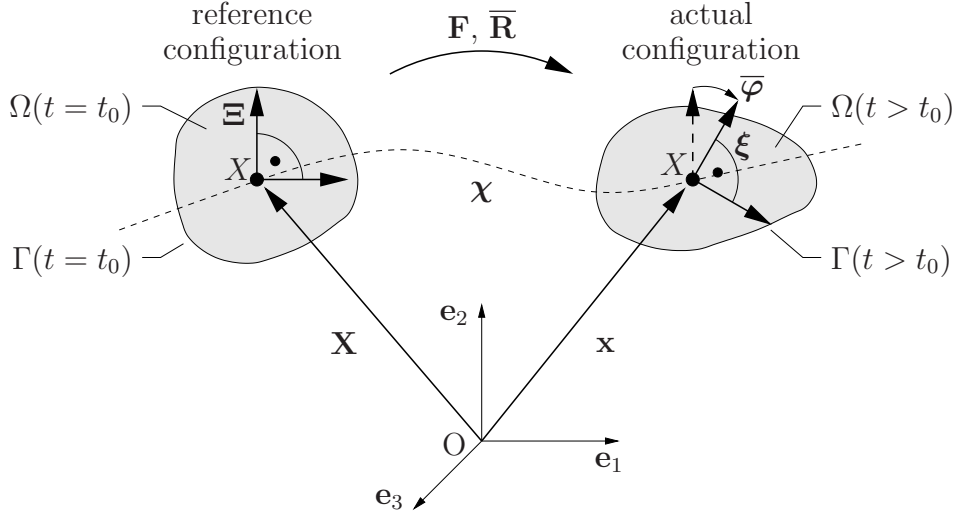
Closing the set of equations, constitutive equations are required relating the

Figure 3.2: *Tonti* diagram of *Cauchy* continuum theory

stress tensor \mathbf{T} towards the strain tensor $\boldsymbol{\varepsilon}$, which in a linear framework can be written in the form

$$\mathbf{T} = \overset{4}{\mathbf{C}} : \boldsymbol{\varepsilon}. \quad (3.13)$$

The set of equations is presented within the *Tonti* diagram pointing out the relations between the different fields, see Fig. 3.2. Therein the body forces \mathbf{b} are set to zero, see Eq. 3.11. Furthermore, strong connections mean that the relation is fulfilled in a strong sense within the standard Finite Element Method (displacement driven) and weak connection that the relation is fulfilled in a weak sense accordingly.

Figure 3.3: Kinematics of *Cosserat* continuum theory

3.2 *Cosserat* continuum theory

Within the *Cosserat* continuum theory (also called micropolar continuum theory [28]) the material point is assumed to be a rigid body with small but finite extension. That means that the rotation of the material point is not fully described by the skew symmetric part of the deformation gradient and, therefore, an extra independent variable $\bar{\varphi}$ is defined, which describes the rigid body rotation of the material point. The rigid body rotation may be visualized by directors attached to the center of the observed entity, whereby the directors are normalized and perpendicular to each other. The translational motion of the directors is fixed to the translation of the material point. Furthermore, the directors are not able to change their length and remain perpendicular to each other. The kinematics of the *Cosserat* continuum theory is presented in Fig. 3.3.

The deformation gradient \mathbf{F} still describes the mapping of a material line element $d\mathbf{X}$ with respect to the reference configuration into a line element $d\mathbf{x}$ with respect to the actual configuration (Eqs. 3.3 and 3.5).

The so-called micromotion describes the relation between the director $\boldsymbol{\xi}$ with respect to the actual configuration and the director $\boldsymbol{\Xi}$ with respect to the reference configuration

$$\boldsymbol{\xi} = \bar{\mathbf{R}}(\mathbf{X}, t) \cdot \boldsymbol{\Xi}. \quad (3.14)$$

$\bar{\mathbf{R}}$ is a proper orthogonal tensor reflecting the rigid body rotation with the following properties

$$\bar{\mathbf{R}} \cdot \bar{\mathbf{R}}^T = \mathbf{I} \quad \text{and} \quad \det \bar{\mathbf{R}} = +1. \quad (3.15)$$

The *Cosserat* strain tensor $\bar{\mathbf{E}}$ with respect to the reference configuration is motivated by comparison of scalar products of line elements with directors with respect to the actual and the reference configuration

$$\begin{aligned} \boldsymbol{\xi} \cdot d\mathbf{x} - \boldsymbol{\Xi} \cdot d\mathbf{X} &= (\bar{\mathbf{R}} \cdot \boldsymbol{\Xi}) \cdot (\mathbf{F} \cdot d\mathbf{X}) - \boldsymbol{\Xi} \cdot d\mathbf{X} \\ &= \boldsymbol{\Xi} \cdot (\bar{\mathbf{R}}^T \cdot \mathbf{F} - \mathbf{I}) \cdot d\mathbf{X} \\ &=: \boldsymbol{\Xi} \cdot \bar{\mathbf{E}} \cdot d\mathbf{X} \end{aligned} \quad (3.16)$$

leading to the definition of the *Cosserat* strain tensor with respect to the reference configuration

$$\bar{\mathbf{E}} := \bar{\mathbf{R}}^T \cdot \mathbf{F} - \mathbf{I}. \quad (3.17)$$

Equation 3.17 can be linearized by restricting the rotation tensor towards small rotations. Starting point is the *Euler-Rodrigues* form of the spatial rotation

$$\bar{\mathbf{R}} = \mathbf{a} \otimes \mathbf{a} + \cos \varphi (\mathbf{I} - \mathbf{a} \otimes \mathbf{a}) + \sin \varphi (\mathbf{a} \times \mathbf{I}). \quad (3.18)$$

Therein \mathbf{a} is the rotation axis and φ the rotation angle. In the case of small rotations it holds

$$\sin \varphi \approx \varphi \quad \text{and} \quad \cos \varphi \approx 1. \quad (3.19)$$

Thus, the linearized rotation tensor $\bar{\mathbf{R}}_{lin}$ has the form

$$\bar{\mathbf{R}}_{lin} = \mathbf{I} + (\mathbf{a} \times \mathbf{I}) \varphi = \mathbf{I} + \overset{3}{\mathbf{E}} : (\mathbf{a} \otimes \mathbf{I}) \varphi = \mathbf{I} - \overset{3}{\mathbf{E}} \cdot \bar{\boldsymbol{\varphi}}, \quad (3.20)$$

whereby $\overset{3}{\mathbf{E}}$ is the so-called *Ricci* tensor also called permutation tensor. Then the linearized *Cosserat* strain tensor $\bar{\boldsymbol{\varepsilon}}$ reads

$$\bar{\boldsymbol{\varepsilon}} = \text{Grad } \mathbf{u} + \overset{3}{\mathbf{E}} \cdot \bar{\boldsymbol{\varphi}}. \quad (3.21)$$

Due to the unsymmetry of the *Cosserat* strain tensor $\bar{\boldsymbol{\varepsilon}}$, the tensor can be split into a symmetric part $\text{sym}(\bar{\boldsymbol{\varepsilon}})$ and a skew symmetric part $\text{skw}(\bar{\boldsymbol{\varepsilon}})$

$$\bar{\boldsymbol{\varepsilon}} = \text{sym}(\bar{\boldsymbol{\varepsilon}}) + \text{skw}(\bar{\boldsymbol{\varepsilon}}). \quad (3.22)$$

The symmetric part $\text{sym}(\bar{\boldsymbol{\varepsilon}})$ is identical to the linearized strain tensor of the *Cauchy* continuum theory (Eq. 3.9)

$$\text{sym}(\bar{\boldsymbol{\varepsilon}}) = \frac{1}{2} (\text{Grad } \mathbf{u} + \text{Grad}^T \mathbf{u}) \quad (3.23)$$

while the skew symmetric part $\text{skw}(\bar{\boldsymbol{\varepsilon}})$ implies the difference between con-

tinuum rotation $-\frac{1}{2}(\text{Grad } \mathbf{u} - \text{Grad}^T \mathbf{u})$ and free rotation $-\overset{3}{\mathbf{E}} \cdot \bar{\boldsymbol{\varphi}}$

$$\text{skw}(\bar{\boldsymbol{\varepsilon}}) = \frac{1}{2}(\text{Grad } \mathbf{u} - \text{Grad}^T \mathbf{u}) + \overset{3}{\mathbf{E}} \cdot \bar{\boldsymbol{\varphi}}. \quad (3.24)$$

In addition to the *Cosserat* strain tensor another deformation measure is needed describing the spatial change of the micromotion $\bar{\mathbf{R}}$. The so-called third order curvature tensor defined with respect to the reference configuration is introduced by

$$\overset{3}{\mathbf{K}} = (\bar{\mathbf{R}}^T \cdot \text{Grad } \bar{\mathbf{R}})^{\underline{3}}. \quad (3.25)$$

Using the following identity

$$\text{Grad } \mathbf{I} = \text{Grad}(\bar{\mathbf{R}}^T \cdot \bar{\mathbf{R}}) = \overset{3}{\mathbf{0}} \quad (3.26)$$

the skew symmetry of the curvature tensor with respect to the both first basis systems can be shown. Thus, one can build the rejuvenation of the third order tensor $\overset{3}{\mathbf{K}}$ by the *Ricci* tensor $\overset{3}{\mathbf{E}}$ without loss of information

$$\bar{\mathbf{K}} = -\frac{1}{2}(\overset{3}{\mathbf{E}} : \overset{3}{\mathbf{K}})^{\underline{2}}. \quad (3.27)$$

The linearized second order curvature tensor $\bar{\boldsymbol{\kappa}}$ is derived by linearization of the third order curvature tensor

$$\overset{3}{\mathbf{K}}_{lin} = \text{Grad}(-\overset{3}{\mathbf{E}} \cdot \bar{\boldsymbol{\varphi}}) = -\left[\overset{3}{\mathbf{E}} \cdot \text{Grad } \bar{\boldsymbol{\varphi}}\right]^{\underline{3}} \quad (3.28)$$

and applying the rejuvenation afterwards

$$\bar{\boldsymbol{\kappa}} = -\frac{1}{2} (\overset{3}{\mathbf{E}} : \overset{3}{\mathbf{K}}_{lin})^2 = \frac{1}{2} \left[\overset{3}{\mathbf{E}} : (\overset{3}{\mathbf{E}} \cdot \text{Grad } \bar{\boldsymbol{\varphi}})^{\otimes 2} \right] = \text{Grad } \bar{\boldsymbol{\varphi}}. \quad (3.29)$$

The balance of momentum in the quasi-static case neglecting body forces reads

$$\text{div } \mathbf{T} = \mathbf{0}, \quad (3.30)$$

which is identical to the balance equation derived for the *Cauchy* continuum. However, the balance of moment of momentum reads

$$\mathbf{I} \times \mathbf{T} + \text{div } \mathbf{M} = \mathbf{0}. \quad (3.31)$$

\mathbf{M} is the so-called couple stress tensor, which is the dual quantity with respect to the linearized curvature tensor $\bar{\boldsymbol{\kappa}}$. $\mathbf{I} \times \mathbf{T}$ is the axial vector, which is assigned to the skew symmetric part of the stress tensor \mathbf{T} .

Furthermore, the *Dirichlet* and *Neumann* boundary conditions have to be fulfilled on the boundaries

$$\begin{aligned} \mathbf{u}|_{\Gamma_u} &= \widehat{\mathbf{u}} \text{ on } \Gamma_u, & \mathbf{t}|_{\Gamma_t} &= \widehat{\mathbf{t}} \text{ on } \Gamma_t, & \Gamma_u \cup \Gamma_t &= \Gamma, & \Gamma_u \cap \Gamma_t &= \emptyset, \\ \bar{\boldsymbol{\varphi}}|_{\Gamma_{\bar{\varphi}}} &= \widehat{\bar{\boldsymbol{\varphi}}} \text{ on } \Gamma_{\bar{\varphi}}, & \mathbf{m}|_{\Gamma_m} &= \widehat{\mathbf{m}} \text{ on } \Gamma_m, & \Gamma_{\bar{\varphi}} \cup \Gamma_m &= \Gamma, & \Gamma_{\bar{\varphi}} \cap \Gamma_m &= \emptyset. \end{aligned} \quad (3.32)$$

Again, closing the set of equations, constitutive equations are required relating the stress tensor \mathbf{T} towards the strain tensor $\bar{\boldsymbol{\varepsilon}}$ and the couple stress tensor \mathbf{M} towards the curvature tensor $\bar{\boldsymbol{\kappa}}$, which can be written in the form

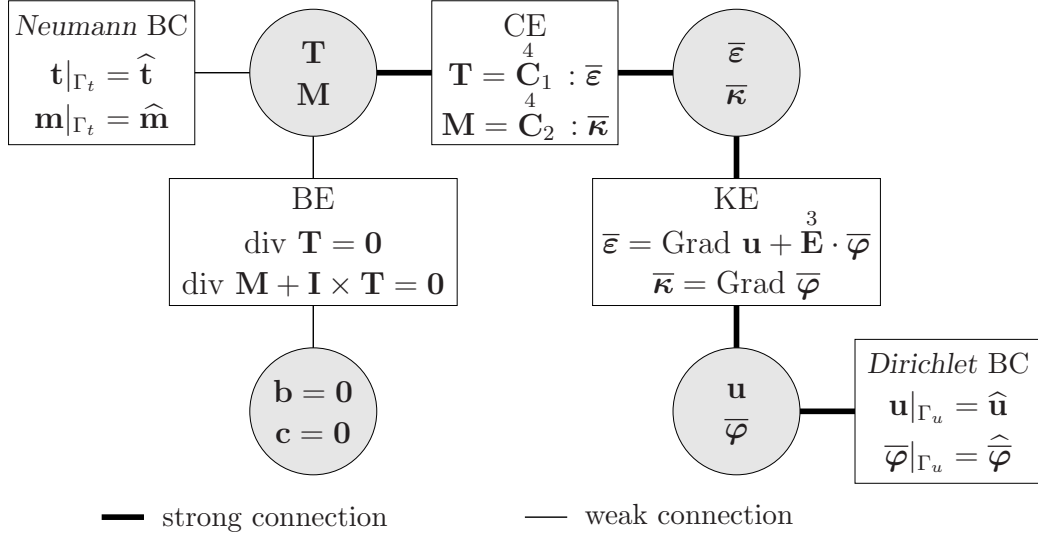


Figure 3.4: Tonti diagram of Cosserat continuum theory

$$\mathbf{T} = \overset{4}{\mathbf{C}}_1 : \bar{\boldsymbol{\varepsilon}} \quad \text{and} \quad \mathbf{M} = \overset{4}{\mathbf{C}}_2 : \bar{\boldsymbol{\kappa}}. \quad (3.33)$$

The Tonti diagram representing the Cosserat continuum theory is shown in Fig. 3.4.

Apart from the first publication concerning the Cosserat continuum theory, the work presented by the brothers Cosserat [11], a more detailed description of the theory can be found e. g. in [25, 26, 27, 28].

Chapter 4

Beam theories

Two major difficulties arise in the formulation of the constitutive equations describing the growth and remodeling processes. The first difficulty results from the complex anisotropic deformation behavior of the microstructure represented by the constitutive equation: they are a function of the trabecular geometry consisting of trabecular length, thickness and orientation. The second difficulty is the formulation of evolution equations. On a microscopic level, e. g. for a single trabecula, the processes are studied in detail, so that evolution equations can be motivated by observations from experiments. In contrast to that, on a macroscopic level the evolution equations have to be formulated purely phenomenologically, usually without the possibility to evaluate the equations by comparison to experimental data.

Thus, many models describing the remodeling of bone work on the microscopic geometry, e. g. they are derived by micro computer tomography (μ CT). However, due to the large amount of degrees of freedom (DOF), this method is very time consuming at the present moment, so that computations for a complete femur can rarely be found in literature.

Reducing the number of DOF the microscopic model of open-cell foam-like structures can be approximated by beam structures.

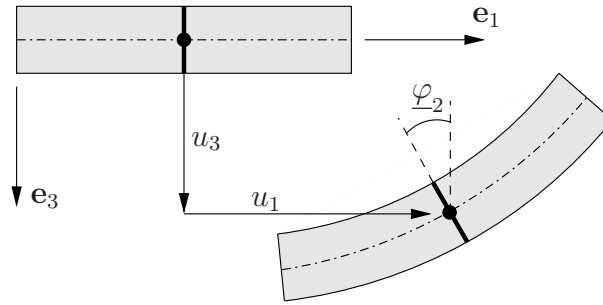


Figure 4.1: Kinematics of *Euler-Bernoulli* beam theory

In the following two beam theories, namely the well-known *Euler-Bernoulli* beam theory and the *Timoshenko* beam theory [9], are shortly repeated.

4.1 *Euler-Bernoulli* beam theory

The basic kinematic hypothesis of the *Euler-Bernoulli* beam theory states that the normal to the beam axis remains plane and normal during deformation and the normal is inextensible. Thus, the rotation $\underline{\varphi}$ of the cross-section becomes a dependent variable and is equal to the continuum rotation, see Fig. 4.1,

$$\underline{\varphi}_2 = -\frac{d\underline{u}_3}{dx_1} \quad \text{and} \quad \underline{\varphi}_3 = \frac{d\underline{u}_2}{dx_1}. \quad (4.1)$$

Thereby, the quantities belonging to the beam theory are marked with an underscore to avoid mixing up with quantities belonging to continuum theories as described in chapter 3.

The *Euler-Bernoulli* beam theory can be derived by one-dimensional reduction of the *Cauchy* continuum theory. Owing to this relation the kinematical equations (KE), constitutive equations (CE) and balance equations (BE) are

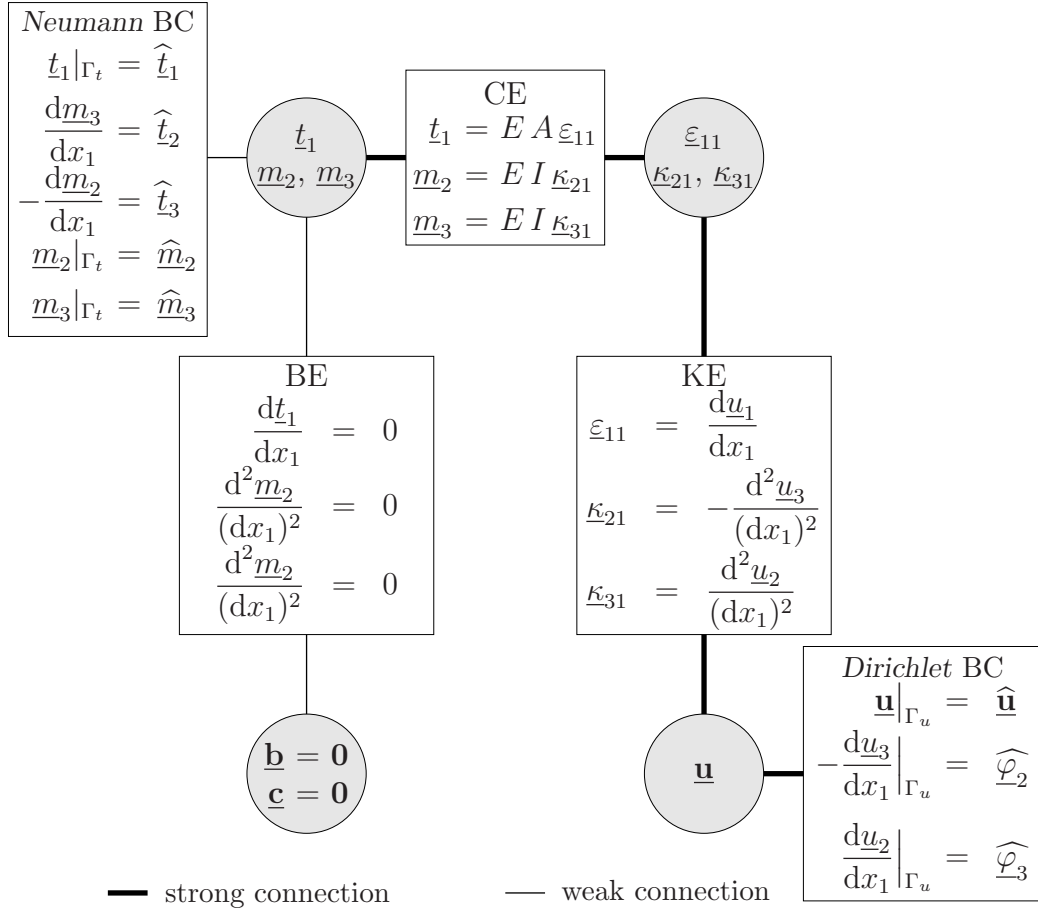
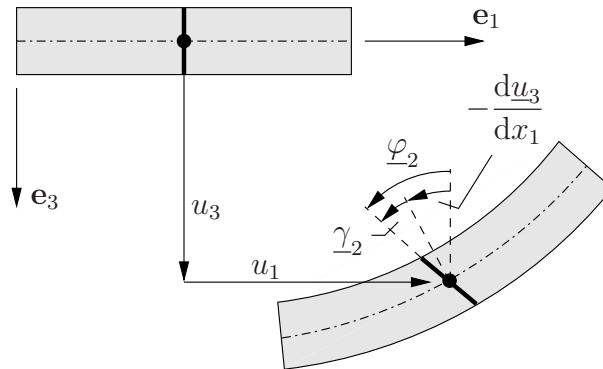


Figure 4.2: Tonti diagram of Euler-Bernoulli beam theory

the same as given in section 3.1. However, beam theories are formulated rather using stress resultants than stress quantities. This is taken into account in the Tonti diagram of the Euler-Bernoulli beam theory, see Fig. 4.2. The results are presented in matrix notation eliminating unnecessary quantities. Effects of skew bending are not considered because of the round cross sectional area (deviation moment of the geometrical moment of inertia equals zero).

Figure 4.3: Kinematics of *Timoshenko* beam theory

4.2 *Timoshenko* beam theory

The basic kinematic hypothesis of the *Timoshenko* beam theory states that the normal to the beam axis remains plane during deformation and the normal is inextensible. However, in contrast to the *Euler-Bernoulli* beam theory, the normal is not required to remain normal during deformation. Thus, the overall rotation $\underline{\varphi}$ is composed of the continuum rotation and an extra rotation caused by shear deformation, see Fig. 4.3,

$$\underline{\gamma}_2 = \frac{du_3}{dx_1} + \underline{\varphi}_2 \quad \text{and} \quad \underline{\gamma}_3 = -\frac{du_2}{dx_1} + \underline{\varphi}_3. \quad (4.2)$$

The *Timoshenko* beam theory can be derived by one-dimensional reduction of the *Cosserat* continuum theory. Owing to this relation the kinematical equations (KE), constitutive equations (CE) and balance equations (BE) are the same as given in section 3.2. Again the resulting equations using stress resultants are presented in the *Tonti* diagram (Fig. 4.4).

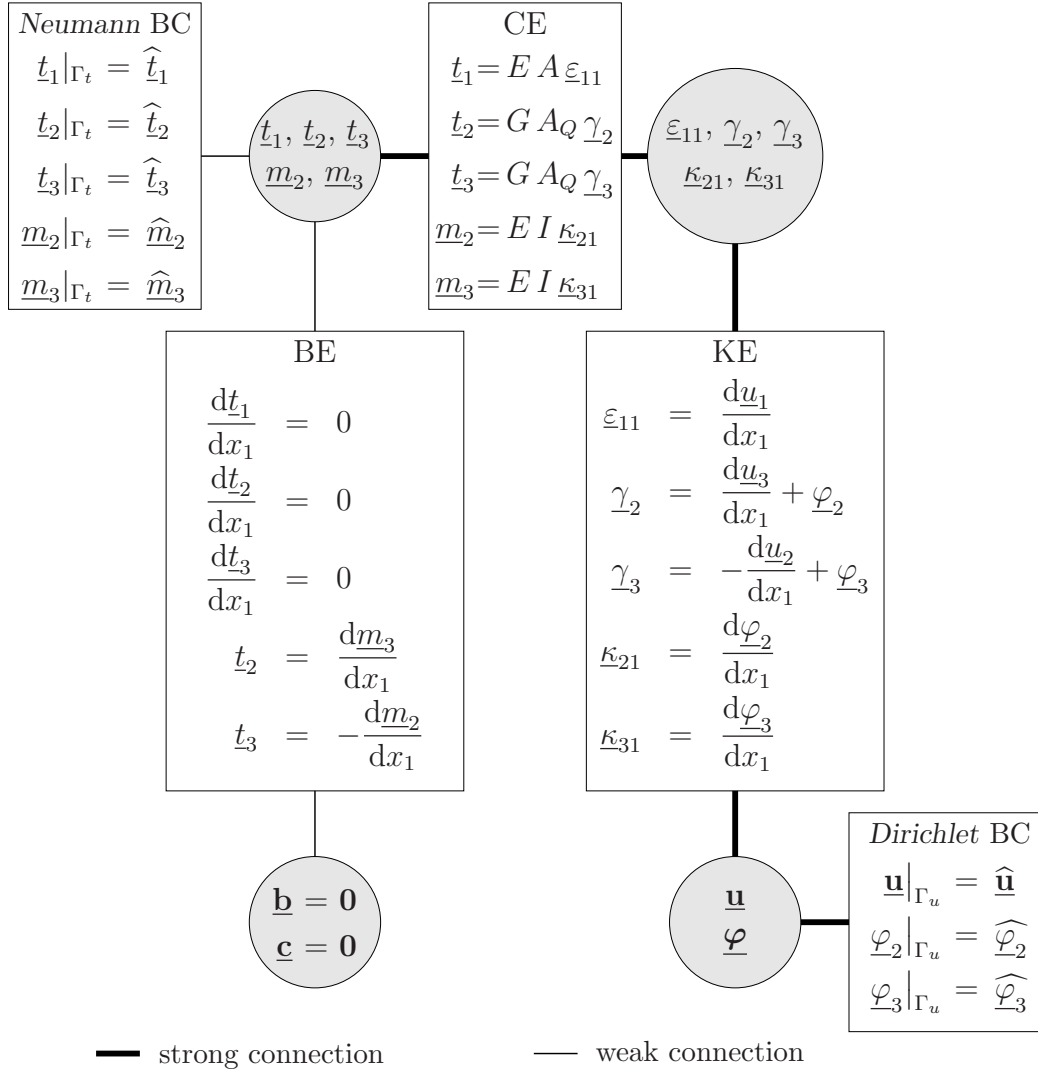


Figure 4.4: Tonti diagram of Timoshenko beam theory

Chapter 5

FE² approach

Compared to microscopic models (models resolving the exact beam-like microstructure either by voxel elements [4, 47, 61, 69, 74] or by beam elements [55, 70, 76]) macroscopic models based on continuum theories are numerically very efficient due to the reduced number of degrees of freedom (DOF). However, due to the difficulties mentioned in the previous chapter, namely the formulation of the constitutive equations, one aims to replace the complex constitutive equations by much simpler constitutive equations, e. g. in the context of trabecular bone to replace the constitutive equations describing the behaviour of an assembly of trabeculae by constitutive equations for a single trabecula. Thereby two advantages are important: the first is the split of information, the second the larger amount of available studies concerning the constitutive behaviour of a single trabecula or even smaller parts compared to assemblies of trabeculae. In this context split of information means separating effects into a part depending on the geometry and a part depending on the constitutive relations.

Using a continuum theory with constitutive equations on a smaller scale requires a homogenization procedure to transform quantities from the smaller scale to the larger scale and an inverse homogenization procedure, in the following called projection, to transform quantities from the larger scale to the

smaller scale. This idea of including constitutive equations of a smaller scale into a macroscopic continuum model is known from literature as FE^2 approach. In the FE^2 approach a microstructure with a certain size is attached to the integration point of a macroscopic FE discretization of the continuum model. Kinematical quantities at the integration point, e. g. strains, are projected to the boundary of the attached microstructure. Then, a *Dirichlet* boundary value problem is solved for the attached microstructure yielding the stress response. By homogenization of the stress-like quantities one gets the stress answer on the macroscopic level.

The FE^2 is restricted by the consideration that kinematical and stress-like quantities are known to the observer only on the surface of the attached microstructure. That means that the displacements resulting from projection of macroscopic strains are applied to points on the surface of the attached microstructure only.

Each homogenization process is connected with a loss of information. In first order homogenization (FOH) the homogenized quantity is just the average of the quantity. In second order homogenization (SOH) higher order information is included usually by taking the average gradient of the quantity into account in addition to the average quantity. Within the FE^2 approach it has to be guaranteed that the information provided by the continuum theory can be handled by the attached microstructure. Thus, in the following the FE^2 approach based on first order homogenization and second order homogenization are presented separately.

The basic idea of the FE^2 approach is sketched in Fig. 5.1.

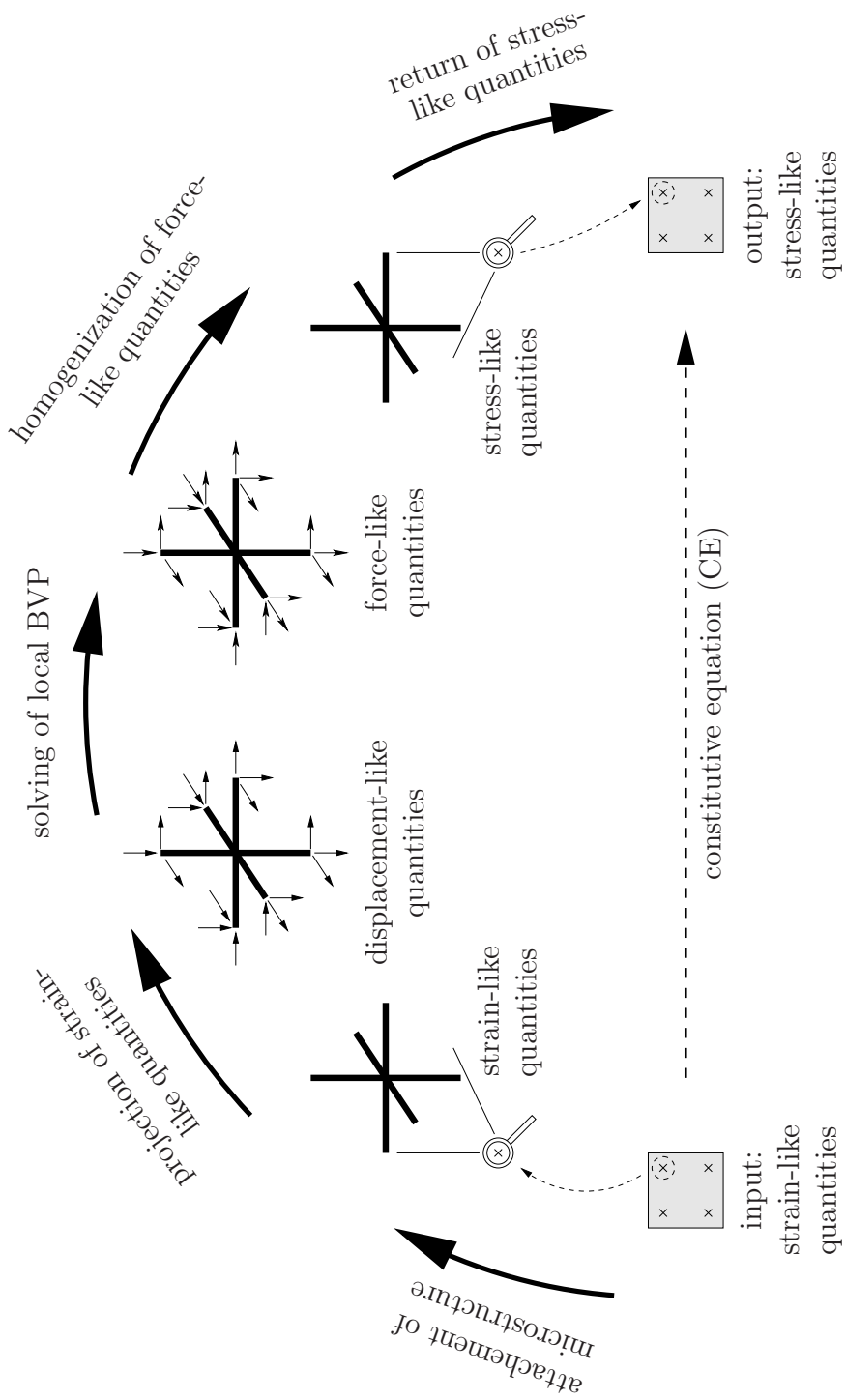


Figure 5.1: Basic idea of FE² approach

5.1 FE^2 approach using first order homogenization (FOH)

In the first order homogenization only the average of a certain quantity is calculated. All higher order effects, e. g. the curvature as the gradient of the strain tensor, are considered as fluctuations and cancel out during the homogenization procedure. Thus, on the macroscopic level a continuum theory has to be chosen which does not require information on higher order effects. This condition is fulfilled by the *Cauchy* continuum theory, which includes neither higher order information of the strain tensor nor of the stress tensor. This still enables to choose an arbitrary beam formulation for the beams of the attached microstructure. In the following the *Euler-Bernoulli* beam theory is chosen to model the beams of the attached microstructure. This is motivated by the kinematical relationship between *Cauchy* continuum theory and *Euler-Bernoulli* beam theory. However, the *Timoshenko* beam theory could also be used instead of it.

The next problem is to find an adequate microstructure, which can be attached to the macroscopic integration point. Many studies have been performed and discussed in the literature about the size of such a microstructure often called representative volume element (RVE). However, they all make use of the condition that the microstructure has to be representative in a statistical sense. In the present work a weaker requirement on the attached microstructure is used: the microstructure is only required to reflect the principal deformation behaviour. This allows for a much smaller microstructure compared to the strong requirement for representative microstructures. According to *Huet* this microstructure is referred to as testing volume element (TVE) [46].

The chosen microstructure is shown in Fig. 5.2. The microstructure is motivated by the observation that the trabeculae cross each other by an angle of about 90° . As will be shown later, moments on the boundary of the attached microstructure cannot be taken into account in first order homogenization. Thus, at all beam ends on the boundary are assumed to be hinges indicated by circles.

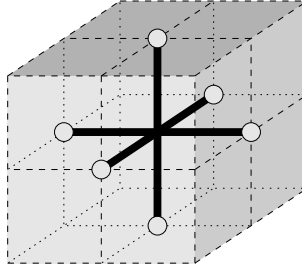


Figure 5.2: Attached microstructure in first order homogenization

5.1.1 Projection

The strain-like quantities are considered to be known at the integration point of the macroscopic FE discretization. In the context of the *Cauchy* continuum theory, this is the strain tensor only. Keeping in mind that only small deformations are assumed the distinction between different strain measures is not necessary. After attaching the microstructure to the integration point, the strain information is projected to the boundary of it. Thereby the projection can be understood as the inverse of homogenization. In homogenization an average value is calculated for a certain quantity over a certain volume. Information of higher order is assumed to be fluctuation and therefore cancels out during homogenization. Thus, in the inverse procedure (projection) information about the fluctuation is not available and therefore only the average quantity is projected to the boundary. Based on equation 3.9 the projection is calculated by

$$\bar{\mathbf{u}} = \boldsymbol{\varepsilon} \cdot \bar{\mathbf{x}}, \quad (5.1)$$

whereby $\bar{\mathbf{x}}$ is the vector from the center of the microstructure to the boundary often called branch vector. Eq. 5.1 yields the *Dirichlet* boundary conditions for the microstructural boundary value problem prescribing the microscopic displacement field $\bar{\mathbf{u}}$ on the boundary of the TVE. Due to the chosen beam-like microstructure the equation has to be solved only for the six nodes on the boundary of the microstructure

$$\bar{\mathbf{u}}_i = \boldsymbol{\varepsilon} \cdot \bar{\mathbf{x}}_i. \quad (5.2)$$

For a better understanding of the projection in the following the homogenization of the strain tensor is presented, although the relation between strain field and homogenized strain tensor is never really needed within the FE² approach.

The homogenization is performed by volumetrical averaging over the domain Ω in the form

$$\langle \bullet \rangle = \frac{1}{V} \int_{\Omega} (\bullet) dv. \quad (5.3)$$

Using the divergence theorem for a continuously distributed quantity

$$\int_{\Omega} \text{grad}(\bullet) dv = \int_{\partial\Omega} (\bullet) \otimes \mathbf{n} da, \quad (5.4)$$

whereby $\partial\Omega$ is the surface of the domain and \mathbf{n} the outward directed normal vector on the surface of the domain, the homogenized strain tensor can be calculated from the displacement field \mathbf{u} at the surface of the domain

$$\langle \boldsymbol{\varepsilon} \rangle = \frac{1}{V} \int_{\Omega} \boldsymbol{\varepsilon} dv = \frac{1}{V} \int_{\Omega} \text{grad} \mathbf{u} dv = \frac{1}{V} \int_{\partial\Omega} \mathbf{u} \otimes \mathbf{n} da \quad (5.5)$$

using the symmetry of the gradient of the displacement field ($\text{grad} \mathbf{u} = \text{grad}^T \mathbf{u}$) due to the projection of a symmetric strain tensor, see Eq. 5.1, instead of using the general equation (Eq. 3.9) for the calculation of the strain tensor. However, this relation is restricted to the case of a continuously distributed quantity in the inner of the domain. For the chosen microstructure consisting of six beam elements it is not the case. Thus, in analogy to the

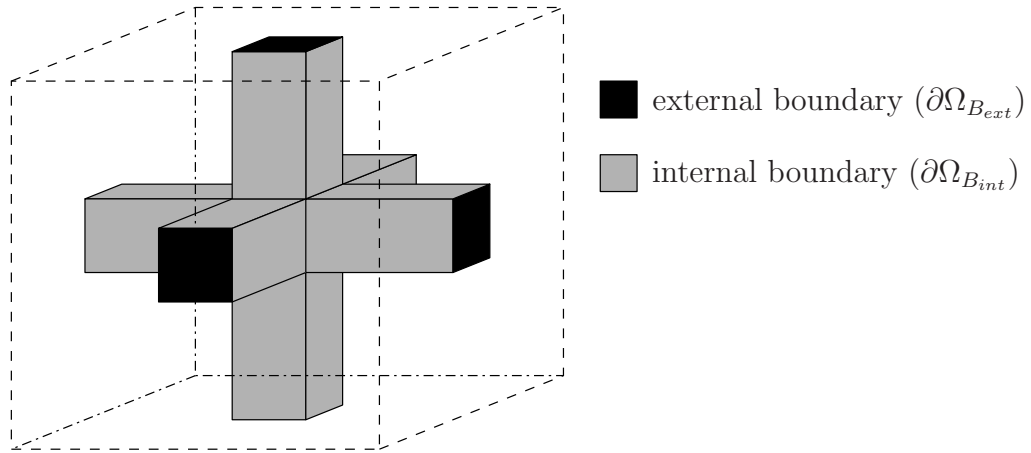


Figure 5.3: Internal and external boundaries of beam elements

case of continuously distributed matter, this equation is used as a definition for the discontinuous case

$$\langle \boldsymbol{\varepsilon} \rangle := \frac{1}{V_B} \int_{\partial\Omega_{B_{ext}}} \mathbf{u} \otimes \mathbf{n} da_{B_{ext}}. \quad (5.6)$$

Thereby V_B is the volume content of the beams, $\partial\Omega_{B_{ext}}$ the external boundary defined by the beam ends, which coincides with the hull of the microstructure (hence the six beam ends), and $da_{B_{ext}}$ an incremental surface element of that boundary, see Fig. 5.3.

In the following the involved kinematical error will be shown using the divergence theorem in the case of discontinuously distributed matter. The basic idea is to split the homogenization into two separate parts. The first is the homogenization of the strain in the inner of the beam elements

$$\langle \boldsymbol{\varepsilon} \rangle_B := \frac{1}{V_B} \int_{\partial\Omega_B} \mathbf{u} \otimes \mathbf{n} da_B. \quad (5.7)$$

The second part is the homogenization of the strain in the surrounding domain $\langle \boldsymbol{\varepsilon} \rangle_S$. By definition it is assumed that both homogenized strain tensors are identical

$$\langle \boldsymbol{\varepsilon} \rangle_S := \langle \boldsymbol{\varepsilon} \rangle_B. \quad (5.8)$$

Thus, the homogenized strain tensor $\langle \boldsymbol{\varepsilon} \rangle$ considering the complete TVE is equal to the homogenized strain tensor calculated for the domain of the beam elements $\langle \boldsymbol{\varepsilon} \rangle_B$

$$\langle \boldsymbol{\varepsilon} \rangle = \frac{1}{V_B} \int_{\partial\Omega_B} \mathbf{u} \otimes \mathbf{n} da_B. \quad (5.9)$$

Taking into account the symmetry of the microstructure and the kinematics of the beam formulation, which means in that case expressing the displacements in a beam cross section by displacement and rotation of the center line of each beam element, the integral can be simplified by splitting the boundary into two parts: the beam surface, which coincides with the external boundary of the microstructure (the outer beam ends), and the internal beam surface (the cylindrical hull of the beam elements)

$$\langle \boldsymbol{\varepsilon} \rangle = \frac{1}{V_B} \left[\begin{aligned} & \int_{\partial\Omega_{B_{ext}}} \mathbf{u}(\bar{\mathbf{u}}) \otimes \mathbf{n} da_{B_{ext}} + \int_{\partial\Omega_{B_{ext}}} \mathbf{u}(\bar{\boldsymbol{\varphi}}) \otimes \mathbf{n} da_{B_{ext}} + \\ & \int_{\partial\Omega_{B_{int}}} \mathbf{u}(\bar{\mathbf{u}}) \otimes \mathbf{n} da_{B_{int}} + \int_{\partial\Omega_{B_{int}}} \mathbf{u}(\bar{\boldsymbol{\varphi}}) \otimes \mathbf{n} da_{B_{int}} \end{aligned} \right]. \quad (5.10)$$

Fig. 5.4 shows the deformation modes resulting from the projection of the macroscopic strain tensor: three stretch modes corresponding to the diagonal

entries of the strain tensor and three shear modes corresponding to the three independent off-diagonal entries of the symmetric strain tensor.

Due to the symmetry of the microstructure the rotation of the beam's cross section at opposite beam ends is always equal and the normals at the beam ends show into opposite directions. Thus the second term in the integral vanishes. Furthermore the assumed constant radius of the circular beam elements implies that the third term vanishes because the center line displacement $\bar{\mathbf{u}}$ is constant within the cross section so that for each point of the cross section a point with normal into opposite direction can be found by mirroring on its center. Thus equation 5.10 reduces into the form

$$\langle \boldsymbol{\varepsilon} \rangle = \frac{1}{V_B} \left[\int_{\partial\Omega_{B_{ext}}} \mathbf{u}(\bar{\mathbf{u}}) \otimes \mathbf{n} da_{B_{ext}} + \int_{\partial\Omega_{B_{int}}} \mathbf{u}(\bar{\boldsymbol{\varphi}}) \otimes \mathbf{n} da_{B_{int}} \right]. \quad (5.11)$$

As long as the microstructure is loaded by stretch only, which means a deformation into the directions of the beam axes, there is no difference between the simplified evaluation (Eq. 5.6) and the exact evaluation (Eq. 5.11). However, in case of macroscopic shear deformation enforcing bending of the beam elements so that the beam rotations $\bar{\boldsymbol{\varphi}}$ are not equal to zero, the difference becomes obvious. In tabular 5.1 the difference between simplified calculation and exact calculation for shear modes is shown for the *Euler-Bernoulli* beam theory as well as for the *Timoshenko* beam theory.

The results given in tabular 5.1 show that the simplified calculation of the homogenized shear strain $\langle \varepsilon_{ik} \rangle$ has nothing to do with the real homogenized shear strain: the *Euler-Bernoulli* beam element is not able to reflect a deformation mode with a remaining shear strain after homogenization. The *Timoshenko* beam element is able to reflect such a deformation mode, but the result is completely different from the simplified calculation. Furthermore it is interesting that for the simplified calculation both beam formulations yield the same result, which is a strong argument for using the kinematically simpler *Euler-Bernoulli* beam element.

Due to the results one may argue that the simplified homogenization cannot

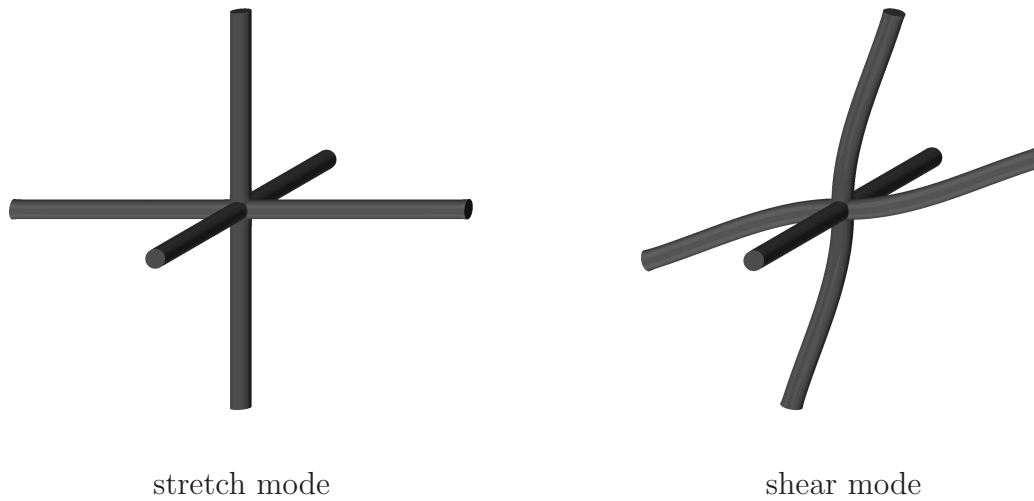


Figure 5.4: Deformation modes in first order homogenization

be used within the FE^2 approach. However, the microstructure is only required to be representative in a weak sense as mentioned before. That means that the microstructure should be able to reflect the different deformation modes, but it is not required that homogenization of the real microscopic strain field yields the macroscopic strain field. That means that macroscopic load carrying by shear may be transferred into microscopic load carrying by stretch and curvature. Furthermore, this small example demonstrates that the material parameters used by the model should not directly be taken from measurements from single trabeculae. Better results may be derived using parameter identification based on macroscopic experimental data.

5.1.2 Homogenization

Solving the microstructural boundary value problem the distribution of the stresses is known in the inner of the beam elements. Thus, by homogenization of the stresses the macroscopic stress answer can be calculated.

Using the following identity

	simplified <i>Euler-Bernoulli</i> (Eq. 5.6)	simplified <i>Timoshenko</i> (Eq. 5.6)	exact <i>Euler-Bernoulli</i> (Eq. 5.11)	exact <i>Timoshenko</i> (Eq. 5.11)
$\langle \varepsilon_{ik} \rangle_{ext}$	$\frac{1}{3} \frac{\bar{w}}{l}$	$\frac{1}{3} \frac{\bar{w}}{l}$	$\frac{1}{3} \frac{\bar{w}}{l}$	$\frac{1}{3} \frac{\bar{w}}{l}$
$\langle \varepsilon_{ki} \rangle_{ext}$	$\frac{1}{3} \frac{\bar{w}}{l}$	$\frac{1}{3} \frac{\bar{w}}{l}$	$\frac{1}{3} \frac{\bar{w}}{l}$	$\frac{1}{3} \frac{\bar{w}}{l}$
$\langle \varepsilon_{ik} \rangle_{int}$	–	–	$-\frac{1}{3} \frac{\bar{w}}{l}$	$-\frac{1}{3} \frac{1}{2} \bar{\beta}$
$\langle \varepsilon_{ki} \rangle_{int}$	–	–	$-\frac{1}{3} \frac{\bar{w}}{l}$	$-\frac{1}{3} \frac{1}{2} \bar{\beta}$
$\langle \varepsilon_{ik} \rangle$	$\frac{1}{3} \frac{\bar{w}}{l}$	$\frac{1}{3} \frac{\bar{w}}{l}$	0	$\frac{1}{3} \left(\frac{\bar{w}}{l} - \frac{\bar{\beta}}{2} \right)$

Table 5.1: Error involved in projection

$$\operatorname{div}(\mathbf{x} \otimes \mathbf{T}) = \mathbf{x} \otimes \operatorname{div} \mathbf{T} + (\operatorname{grad} \mathbf{x}) \cdot \mathbf{T}^T \quad (5.12)$$

and the balance of momentum (Eq. 3.10) it follows for the transposed stress tensor

$$\langle \mathbf{T}^T \rangle = \frac{1}{V} \int_{\Omega} \mathbf{T}^T \, dv = \frac{1}{V} \int_{\Gamma} \mathbf{x} \otimes \mathbf{t} \, da. \quad (5.13)$$

Transposition of the terms on the left and right yields

$$\langle \mathbf{T} \rangle = \frac{1}{V} \int_{\Gamma} \mathbf{t} \otimes \mathbf{x} \, da, \quad (5.14)$$

which means that the homogenized stress tensor can be calculated from quantities known on the surface of the microstructure as desired by the FE² approach. Taking into account that for the chosen microstructure the surface, where the stresses take non-zero values, consists of the six beam ends the surface integral over the surface can be replaced by the sum over these nodes

$$\langle \mathbf{T} \rangle = \frac{1}{V} \sum_{i=1}^n \bar{\mathbf{t}}_i \otimes \bar{\mathbf{x}}_i. \quad (5.15)$$

Therein $\bar{\mathbf{t}}_i$ represents the stress resultant at the beam end with index i and $\bar{\mathbf{x}}_i$ is the so-called branch vector pointing from the center of the TVE towards the beam end with index i .

Usually it is proven that the homogenization procedure fulfills the *Hill-Mandel* condition, which requires the equivalence of the exact microscopic and the homogenized macroscopic energy calculated from the homogenized stress and strain tensor. However, it is not possible to calculate the correct homogenized strain tensor from quantities on the boundary of the microstructure. A calculation of the homogenized strain tensor consulting the strain distribution in the inner of the microstructure is possible (as shown in this section under topic 5.1.1), but actually this is not desirable, because the basic idea of the TVE is that access to the quantities of interest is only possible on the boundary of it (like usually in material testing) even if the FE simulation provides the possibility to calculate the quantities in the inner of the TVE. Nevertheless the homogenization procedure is formulated in that way that the *Hill-Mandel* condition is fulfilled.

The calculated homogenized stress tensor is energetically conjugated with respect to the homogenized strain tensor, which can be completely different from the macroscopic strain tensor as shown before. As a consequence the macroscopic energy must not be calculated from the macroscopic strain and homogenized stress tensor.

The complete set of equations needed in the FE² approach using first order homogenization is presented once again in the form of the *Tonti* diagram (Fig. 5.5).

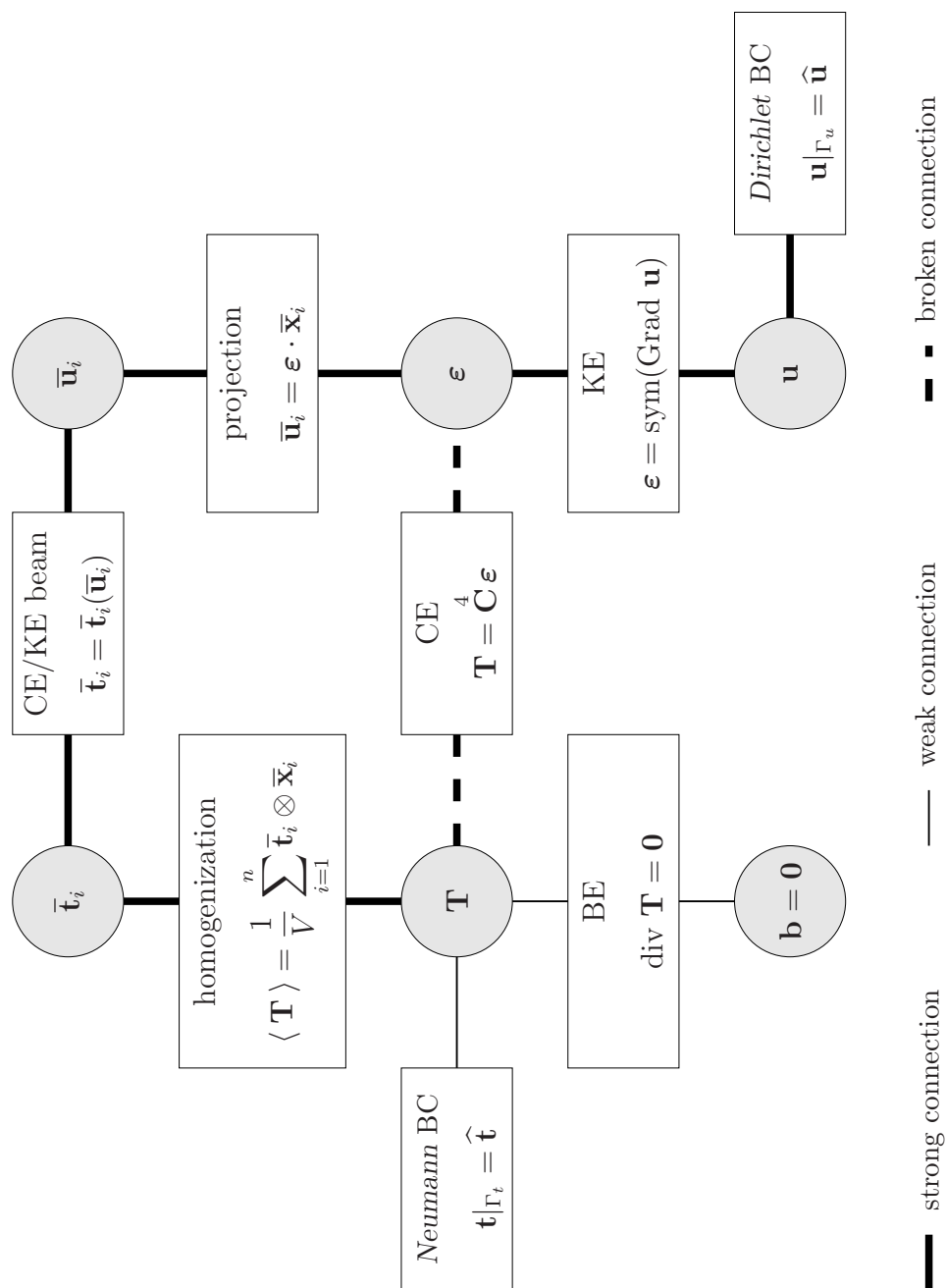


Figure 5.5: Tonti diagram of FE^2 approach using FOH

5.2 FE^2 approach using second order homogenization (SOH)

In second order homogenization in addition to the average of a certain quantity also the average gradient of the quantity is calculated. All higher order effects are still considered as fluctuations and cancel out during the homogenization procedure. That means e. g. that not only the strain tensor is considered in the approach but also the curvature tensor, which reflects the gradient of the strain tensor. On the macroscopic level a macroscopic continuum theory has to be chosen, which can handle the gradient of the fields of interest. In the present approach the fields of interest are the strain and stress tensor. So in addition to that the macroscopic continuum theory has to be able to handle the gradient information of the stress tensor, which is the couple stress tensor, and the gradient of the strain tensor. With respect to the microscale that means that the average and the linear deviation of the stresses and strains are taken into account.

Again an appropriate beam theory has to be chosen for the beams of the attached microstructure. In principle both beam theories seem to be feasible. However, the attached microstructure must be able to reflect all admissible deformation modes. In other words the homogenization of the projected strain-like quantities must not completely vanish. As will be shown later, the homogenization of the projected strain-like quantities completely vanishes for a certain macroscopic deformation in case of the *Euler-Bernoulli* beam theory so that it fails as an appropriate beam theory for the microscopic beam elements.

A similar microstructure is chosen as before in the approach using first order homogenization. The projection of curvature information to the boundary of the attached microstructure yields rotational information on the boundary. Taking this into account the hinges of Fig. 5.2 have to vanish, see Fig. 5.6.

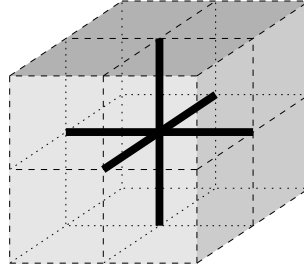


Figure 5.6: Attached microstructure in second order homogenization

5.2.1 Projection

The strain-like quantities of the macromodel are considered to be known at the integration point. In the context of the *Cosserat* continuum theory, this is the *Cosserat* strain tensor and the curvature tensor. After the attachment of the microstructure to the integration point, the information is projected to the boundary of it. The *Cosserat* strain tensor (Eq. 3.21) is constant at the integration point and consists of two parts: a translational part depending on the displacement vector \mathbf{u} and a rotational part depending on the rotation vector $\bar{\varphi}$. If the translational part is constant, the displacement field has to be linear so that the projection is

$$\bar{\mathbf{u}}_i = \bar{\boldsymbol{\varepsilon}}_T \cdot \bar{\mathbf{x}}_i. \quad (5.16)$$

Thereby $\bar{\boldsymbol{\varepsilon}}_T$ has to be symmetric (the skew symmetric part is completely described by the rotational part), because a skew symmetric part in the translational part would yield a stress-free rigid body rotation of the microstructure.

The rotational part is also constant so that it can directly be concluded that the rotation on the boundary resulting from the *Cosserat* strain is equal to the rotation $\bar{\varphi}$

$$\bar{\varphi}_i = \bar{\varphi}. \quad (5.17)$$

The curvature is projected to the boundary by

$$\bar{\varphi}_i = \bar{\kappa} \cdot \bar{\mathbf{x}}_i \quad (5.18)$$

with the same argumentation as for the translational part of the strain tensor: the gradient of the rotation is assumed to be constant, so the distribution of the microrotation has to be linear.

As a consequence of the projection, the rotational information on the boundary of the microstructure consists of a superposition of a strain dependent part, resulting from the skew symmetry of the *Cosserat* strain tensor, and a curvature dependent part.

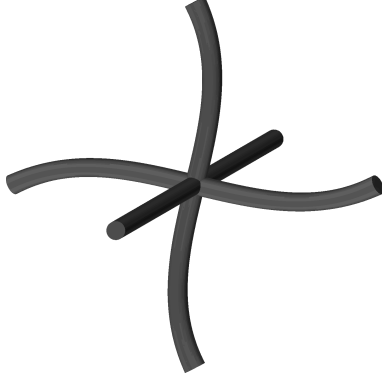
Projecting the skew symmetric part of the strain tensor onto the boundary of the microstructure one now gets the deformed configuration as shown in figure 5.7, which will be called in the following the *Cosserat* deformation mode.

Applying this *Cosserat* deformation mode to the microstructure consisting of *Euler-Bernoulli* beam elements as presented in Fig. 5.6, the components of the homogenized *Cosserat* strain tensor and homogenized curvature tensor are zero due to symmetry as will be shown in the following.

The homogenized *Cosserat* strain tensor for continuously distributed matter using the divergence theorem reads

$$\langle \bar{\boldsymbol{\varepsilon}} \rangle = \frac{1}{V} \int_{\Omega} \bar{\boldsymbol{\varepsilon}} \, dv = \frac{1}{V} \int_{\Gamma} \bar{\mathbf{u}} \otimes \mathbf{n} \, da + \frac{1}{V} \int_{\Omega} \mathbf{E}^3 \bar{\boldsymbol{\varphi}} \, dv \quad (5.19)$$

and the homogenized curvature tensor reads

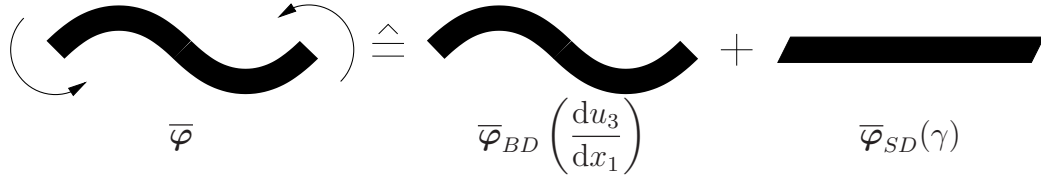


Cosserat mode

Figure 5.7: Cosserat deformation mode

$$\langle \bar{\boldsymbol{\kappa}} \rangle = \frac{1}{V} \int_{\Omega} \bar{\boldsymbol{\kappa}} \, dv = \frac{1}{V} \int_{\Gamma} \bar{\boldsymbol{\varphi}} \otimes \mathbf{n} \, da. \quad (5.20)$$

As shown in figure 5.8 the *Cosserat* deformation mode can be splitted into a bending dependent part $\bar{\boldsymbol{\varphi}}_{BD} \left(\frac{du_3}{dx_1} \right)$ and a shear dependent part $\bar{\boldsymbol{\varphi}}_{SD}(\gamma)$. Using Eqs. 5.19 and 5.20 and calculating for the bending dependent part the homogenized *Cosserat* strain tensor and curvature tensor, all components are zero due to symmetry. Thus, only the shear dependent part affects the homogenized quantities and yields a skew symmetric part of the homogenized *Cosserat* strain tensor. However, this shear dependent part cancels out in the *Euler-Bernoulli* beam theory due to the requirement that the normal remains normal during deformation. That means in other words, using *Euler-Bernoulli* beam elements, the macroscopic homogenized energy is zero and therefore the *Cosserat* deformation mode is not reflected on a macroscopic scale. Circumventing this problem, the attached microstructure must be assembled by *Timoshenko* beam elements.

Figure 5.8: Split of *Cosserat* deformation mode

5.2.2 Homogenization

Solving the microstructural boundary value problem, considering now also in addition rotational boundary conditions, the distribution of the stresses is known in the inner of the beam elements. Thus, by homogenization of the stresses the macroscopic stress answer can be calculated.

The balance of momentum (eq. 3.10) remains the same as for the *Cauchy* continuum. So the calculation of the homogenized stress tensor is identical to that one calculated in first order homogenization (eq. 5.15)

$$\langle \mathbf{T} \rangle = \frac{1}{V} \sum_{i=1}^n \bar{\mathbf{t}}_i \otimes \bar{\mathbf{x}}_i. \quad (5.21)$$

All feasible deformation modes can be divided into modes with axial symmetry (stretch, shear and bending mode) and into modes with skew symmetry (*Cosserat* mode only). After homogenization the balance of moment of momentum (Eq. 3.31) should still be valid

$$\mathbf{I} \times \langle \mathbf{T} \rangle + \text{div} \langle \mathbf{M} \rangle = \mathbf{0}. \quad (5.22)$$

For the deformation modes with axial symmetry the homogenized stress tensor $\langle \mathbf{T} \rangle$ is always symmetric. Thus, the divergence of the couple stress tensor $\langle \mathbf{M} \rangle$ is zero ($\text{div} \langle \mathbf{M} \rangle = \mathbf{0}$). Consequently in analogy to the homogenized stress tensor, the homogenized couple stress tensor can be calculated [18, 24]

$$\langle \mathbf{M} \rangle = \frac{1}{V} \sum_{i=1}^n \bar{\mathbf{m}}_i \otimes \bar{\mathbf{x}}_i, \quad (5.23)$$

which means that it depends on the moments acting on the beam ends but not on the forces.

Equation 5.23 also holds for the skew symmetric deformation modes, which can be shown by substitution of the moment produced by stresses. Starting with the quasistatic form of the balance equation of moment of momentum neglecting body acceleration the global form of the equation is

$$\int_{\Gamma} (\mathbf{x} \times \mathbf{t} + \mathbf{m}) da = \mathbf{0}. \quad (5.24)$$

Using the abbreviation

$$\tilde{\mathbf{m}} = \mathbf{x} \times \mathbf{t} + \mathbf{m} \quad (5.25)$$

with the according *Cauchy* theorem

$$\widetilde{\mathbf{M}} \cdot \mathbf{n} = \tilde{\mathbf{m}}, \quad (5.26)$$

the balance of moment of momentum can be rewritten in the form

$$\operatorname{div} \widetilde{\mathbf{M}} = \mathbf{0}. \quad (5.27)$$

This is analogous to the balance of momentum, see Eq. 3.10. Then the homogenized total couple stress tensor including the moments produced by stresses can be computed formally in the same way as the homogenized stress tensor

$$\langle \widetilde{\mathbf{M}} \rangle = \frac{1}{V} \sum_{i=1}^n \widetilde{\mathbf{m}}_i \otimes \bar{\mathbf{x}}_i = \frac{1}{V} \underbrace{\sum_{i=1}^n (\bar{\mathbf{x}}_i \times \bar{\mathbf{t}}_i) \otimes \bar{\mathbf{x}}_i}_0 + \frac{1}{V} \sum_{i=1}^n \bar{\mathbf{m}}_i \otimes \bar{\mathbf{x}}_i. \quad (5.28)$$

Thereby, the abbreviation introduced in Eq. 5.25 is reversed. $\widetilde{\mathbf{m}}_i$ is the complete discrete moment resulting from the discrete force and moment at beam end i calculated with respect to the center of the TVE. The first summand in Eq. 5.28 is always zero because the vector $\mathbf{x} \times \mathbf{t}$ is perpendicular to the vector \mathbf{x}

$$(\bar{\mathbf{x}}_i \times \bar{\mathbf{t}}_i) \otimes \bar{\mathbf{x}}_i = (\bar{\mathbf{x}}_i \times \bar{\mathbf{x}}_i) \otimes \bar{\mathbf{t}}_i = \mathbf{0}. \quad (5.29)$$

That means that the homogenized couple stress tensor $\langle \widetilde{\mathbf{M}} \rangle$ is independent of the discrete forces $\bar{\mathbf{t}}_i$ and therefore identical to the homogenized couple stress tensor $\langle \mathbf{M} \rangle$ as calculated in Eq. 5.23. In the case of skew symmetric deformation modes Eq. 5.23 and Eq. 5.28, respectively, yield a zero couple stress tensor. This is also in agreement with the consideration that the couple stress tensor is the dual quantity with respect to the curvature tensor. Looking at the skew symmetric *Cosserat* deformation mode in Fig. 5.7, the average curvature is zero due to symmetry and therefore also the couple stress tensor is zero for this specific mode.

It can be shown that the homogenization procedure fulfills the *Hill-Mandel* condition [22, 43, 54] requiring the equivalence of microscopic and homogenized macroscopic energy. However, while the homogenized strain-like quantities are never calculated within the FE² approach, the proof is not given here.

Chapter 6

Application of FE² approach to bone remodeling

6.1 Adaptation of bone:

growth, remodeling and morphogenesis

According to the review article on functional adaptation of biomaterials by *Taber* [77], the adaptation processes of bone can be classified into three categories, which are growth, remodeling and morphogenesis. Thereby, the categories are defined as follows:

- **growth**

mass change through cell divisions (hyperplasia), cell enlargements (hypertrophy), secretion of extracellular matrix (ECM) or accretion on external or internal surfaces. Negative growth is called atrophy.

↪ change in mass

↪ change in topology

- **remodeling**
change of material properties such as strength, density or internal structure.
~> change in local material properties
- **morphogenesis**
shape change of the structure.
~> change in topology
~> no change in mass

The focus of the present work is on the adaptation process taking place in bone material due to the insertion of implants. That means that on the time scale of interest the change in the overall dimension is of secondary importance compared to the adaptation processes taking place in the inner of the bone material.

Within the FE² approach the growth changing the macroscopic dimensions could be considered by increasing the length of the beam elements representing the several trabeculae. To transport the information to the macroscopic level, the microstructure can be pre-stressed so that it fits into the TVE leading to a self-equilibrating stress state in addition to the stress state resulting from the macroscopic loading. The homogenization procedure will consider then also the additional stress state leading to an increasing size of the macroscopic Finite Element if there are no boundary conditions applied which prevent the swelling. This approach matches the idea that growth within a Finite Element is only possible if the adjacent elements are pushed aside.

Furthermore, to keep the model as simple as possible it is not necessary to distinguish between the effects increasing the effective stiffness of the structure. The effective stiffness is affected by the accretion on the internal surfaces (increasing or reducing the size of the cross sectional area of a single trabecula) as well as by modification of the local material properties. Thus, these effects affecting the effective stiffness of the bone material are referred to bone remodeling in the following.

The morphogenesis allows the bone material to adapt to the loading situation by altering the actual topology of the trabecular microstructure.

In the following, remodeling and morphogenesis in the sense of reorientation will be applied to the FE² approach. In the context of remodeling growth means an increase of the trabecular radii and atrophy dwindling of the radii.

6.2 Remodeling

The adaptive remodeling behavior of bone has been studied systematically since the end of the 19th century [16, 60, 73, 80]. Thereby it has been observed that the topology of the spongiosa – the several trabeculae – always adapts with respect to mechanical stimulus. The most obvious observations are that in regions of larger mechanical stimulus also the thickness of a single trabecula is larger and that the trabeculae tend to orient into the principal directions of loading. Thus, the bone material achieves a maximum of stiffness with minimal weight with respect to the average loading situation.

Following the idea of Beaupre, Orr and Carter [7, 8] the range of the mechanical stimulus is divided into three parts. The range of the dead zone has the upper bound T_u and the lower bound T_l , where apposition and resorption are in equilibrium. Crossing the upper bound T_u one reaches the apposition range, where the amount of apposition is larger than the amount of resorption. Falling below the lower bound T_l one reaches the resorption range, where the amount of resorption is larger than the amount of apposition.

This motivates the definition of the stimulus T_Δ , which is greater than zero in case of growth, lower than zero in case of atrophy and otherwise zero

$$T_\Delta = \begin{cases} T_{eq} - T_l & \text{if } T_{eq} < T_l, \\ 0 & \text{if } T_l \leq T_{eq} \leq T_u, \\ T_{eq} - T_u & \text{if } T_{eq} > T_u, \end{cases} \quad (6.1)$$

whereby T_{eq} is the quantity being responsible for growth and atrophy in a phenomenological sense as long as there exists a strong correlation between

this quantity and growth as well as atrophy. In the following T_{eq} is defined as the maximum equivalent stress at the center points of the free beam ends of the TVE.

$$T_{eq} = \sqrt{\sigma_{11}^2 + 3\tau_{12}^2 + 3\tau_{13}^2}. \quad (6.2)$$

Therein σ_{11} are the normal stresses into the direction of the beam axis calculated from the normal force. τ_{12} and τ_{13} are the shear stresses at the beam end resulting from the shear forces. Due to the evaluation at the center points of the beam ends the moments do not enter the equation. The moments at the beam ends are not considered in this formula because in the equilibrium state of interest the effect of the stresses resulting from the moments at the beam ends is negligible while for an arbitrary state they can dominate the equivalent stress T_{eq} , which will stimulate the growth dramatically until the principal directions of the TVE are tolerably aligned with the principal directions of the macroscopic loading. The reason for it is the fact that in the equilibrium state the load is mainly carried by stretching of the microstructural beam elements while for an arbitrary stress state the load is mainly carried by bending leading to much higher bending moments at the beam ends.

Using the definition of the stress stimulus T_{Δ} (Eq. 6.1) growth and atrophy can then be described by logistic functions for the radius d_i of each beam element depending on the sign of the stimulus

$$\dot{d}_i = \begin{cases} \frac{(d_{min} - d_i) d_i}{\eta_2} & \text{if } T_{\Delta} < 0, \\ 0 & \text{if } T_{\Delta} = 0, \\ \frac{(d_{max} - d_i) d_i T_{\Delta}}{\eta_1} & \text{if } T_{\Delta} > 0 \end{cases} \quad (6.3)$$

with the viscous material parameters η_1 and η_2 governing the velocity of thickness change either for growth or for dwindling while from tests it is known that the thickness reduction is faster than the increase of thickness

[63]. d_{min} and d_{max} are the lower and upper bounds for the radius d . Furthermore in case of growth $T_{\Delta} > 0$ the logistic function is weighted by the stimulus itself while in case of atrophy the function is considered to be independent of the stimulus.

The circumferential growth and atrophy of a single beam element of the TVE are visualized in Fig. 6.1.

6.3 Reorientation

The studies of adaptive bone remodeling at the end of the 19th century were already concerned with the correlation between trabecular orientation and principal directions of the stress or strain state [16, 60, 73, 80]. It has been observed that the microstructure tends to orient into the principal direction of the strain tensor and stress tensor respectively. According to this the trabeculae cross each other by an angle of approximately 90° while the principal axes are exactly perpendicular to each other.

To guarantee the right angle between the trabeculae of the TVE, the complete microstructure is able to orient into the principal directions of the load case.

In the following the principal directions are calculated from the strain tensor. The actual orientation of the microstructure is known. Then it is possible to determine the rotation tensor \mathbf{R}_{dif} , which describes the rotation from the actual configuration of the microstructure into the principal direction of the strain tensor, see Fig. 6.2.

Using the Euler-Rodrigues form of the spatial rotation, see also eq. 3.18,

$$\mathbf{R} = \mathbf{a} \otimes \mathbf{a} + \cos \varphi (\mathbf{I} - \mathbf{a} \otimes \mathbf{a}) + \sin \varphi (\mathbf{a} \times \mathbf{I}) \quad (6.4)$$

it is possible to extract the rotation axis \mathbf{a} and the angle of rotation φ . Assuming that the rotation axis remains fixed during the rotational update,

the update is formulated in the following form

$$\mathbf{R}_{TVE}^A = \mathbf{R}_\Delta \cdot \mathbf{R}_{TVE}^R, \quad (6.5)$$

whereby \mathbf{R}_{TVE}^A describes the actual orientation of the TVE after reorientation update and \mathbf{R}_{TVE}^R the reference orientation before reorientation update – in each case with respect to the global coordinate system. \mathbf{R}_Δ is the rotation tensor calculated by use of the Euler-Rodrigues form of spatial rotation (eq. 6.4)

$$\mathbf{R}_\Delta = \mathbf{a} \otimes \mathbf{a} + \cos \varphi_\Delta (\mathbf{I} - \mathbf{a} \otimes \mathbf{a}) + \sin \varphi_\Delta (\mathbf{a} \times \mathbf{I}) \quad (6.6)$$

with the fixed rotation axis \mathbf{a} but a reduced rotation angle φ_Δ . One of the simplest possibilities for the calculation of the orientational update consists in postulating the change of orientation per time to be proportional to the difference of orientation φ

$$\dot{\varphi}_\Delta = c \varphi_\Delta \lambda. \quad (6.7)$$

The evolution equation is weighted by the sum λ of the eigenvalues (absolute values) of the strain tensor to guarantee that the structure reorients only if the microstructure is loaded. Furthermore the parameter c drives the rate of reorientation update.

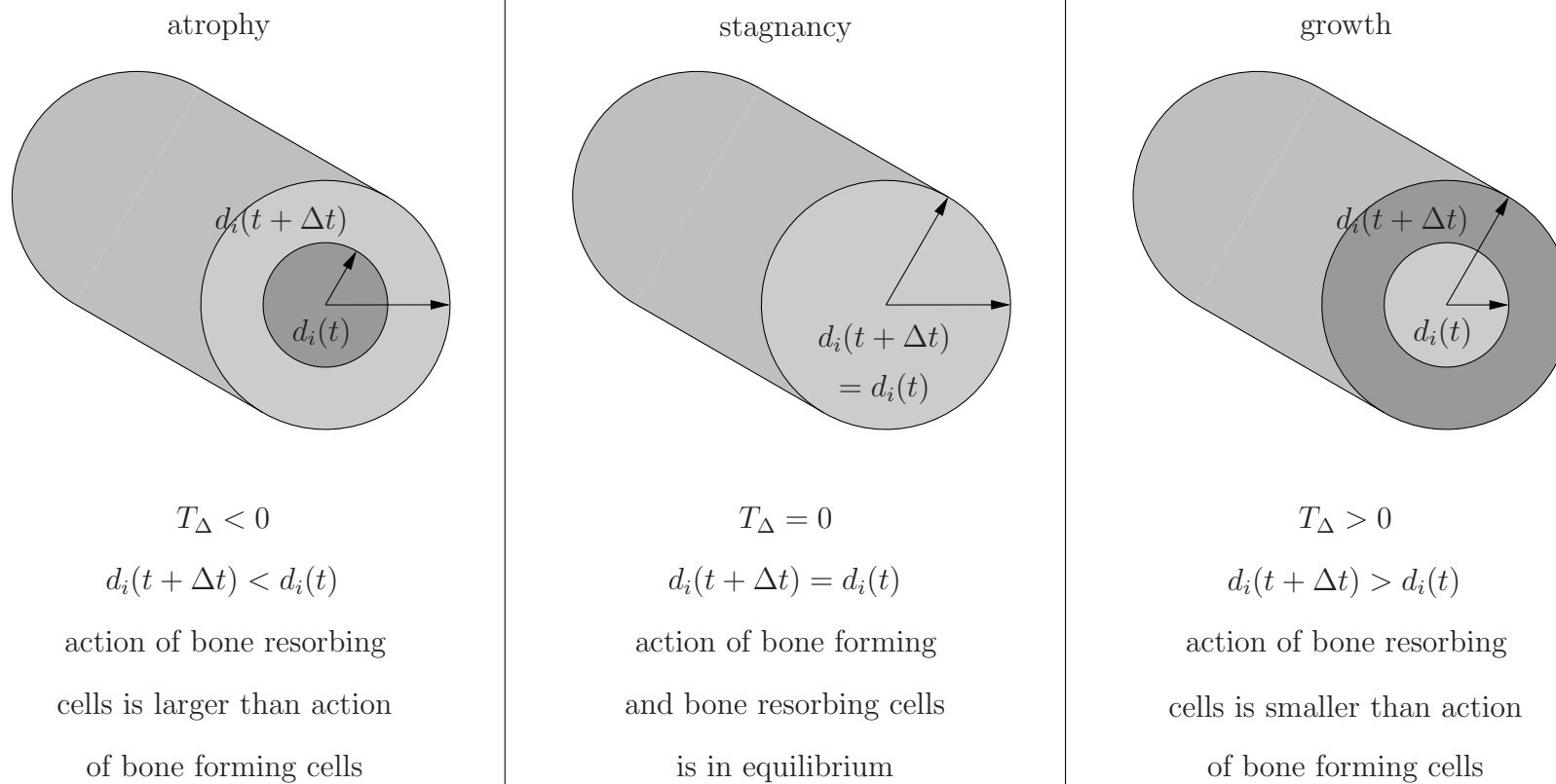


Figure 6.1: Circumferential growth and atrophy

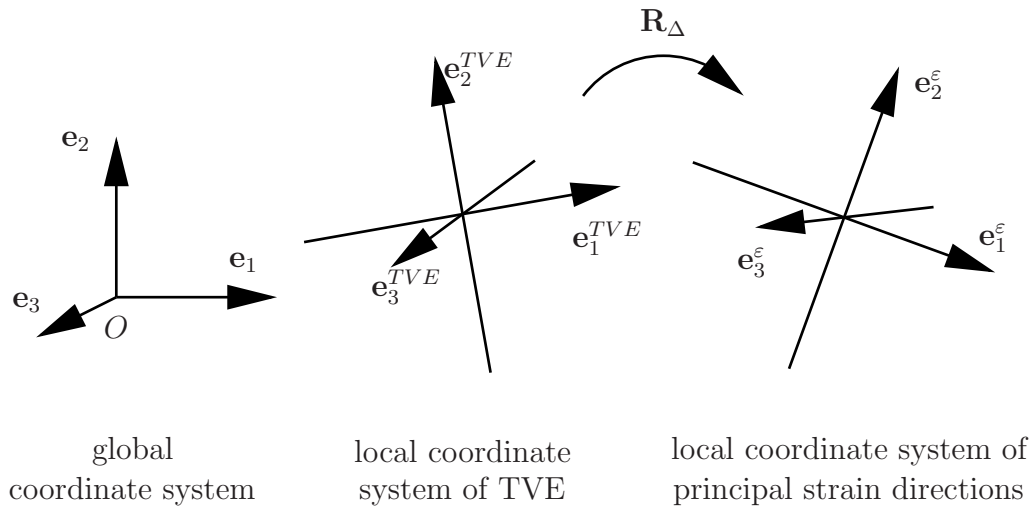


Figure 6.2: Rotational update

Chapter 7

Numerical implementation

The FE^2 concept has been implemented into different Finite Element codes. The first implementation was carried out for the code PANDAS, developed by the Institute of Applied Mechanics (Civil Engineering) at the University of Stuttgart [23]. Thereby, the second order homogenization (SOH) is used with the underlying macroscopic *Cosserat* continuum theory. Discussing the recent effects of the model on two-dimensional examples, one can motivate a much simpler model using the first order homogenization (FOH). This simpler model is numerically more efficient and therefore better suited for a three-dimensional implementation. Having in mind the application to real bone geometries represented by a large number of Finite Elements, the simpler model is implemented into an explicit code. This has the advantage that the global stiffness matrix does not have to be reversed but has the drawback that the time step size is limited due to the Courant-Friedrichs-Lewy condition [12]. The simpler model has been embedded into the commercial code LS-DYNA [40] so that the infrastructure for parallel computing of this code could be used directly.

7.1 Two-dimensional implementation into implicit code PANDAS using SOH

The evolution equations for remodeling (eq. 6.3) and reorientation (eq. 6.3) are solved in an implicit way. However, reducing the numerical effort some simplifications are introduced to avoid iterative solutions involving the complete FE² procedure.

7.1.1 Remodeling

First the thickness change \dot{d}_i is approximated by the thickness difference divided by the time interval Δt

$$\dot{d}_i = \frac{d_i^{n+1} - d_i^n}{\Delta t}, \quad (7.1)$$

whereby superscript n indicates a quantity at the beginning of the time interval and superscript $n + 1$ at the end of the time interval. Then it is possible to solve eq. 6.3 for the actual radius d_i^{n+1} of each beam element i

$$d_i^{n+1} = \begin{cases} \frac{\sqrt{(\eta_2 - d_{min} \Delta t)^2 + 4 \eta_2 \Delta t d_i^n} - \eta_2 + d_{min} \Delta t}{2 \Delta t} & \text{if } T_\Delta < 0, \\ d_i^n & \text{if } T_\Delta = 0, \\ \frac{\sqrt{(F_\Delta \Delta t - d_i^n \eta_1)^2 + 4 \eta_1 d_{max} F_\Delta \Delta t} - F_\Delta \Delta t + \eta_1 d_i^n}{2 \eta_1} & \text{if } T_\Delta > 0, \end{cases} \quad (7.2)$$

using the assumption that the stimulus T_Δ depends quadratically on the

radius, which means that the contribution of bending moments to the stimulus is negligible compared to the contribution of the normal force and shear forces. Thus the stress-like stimulus T_Δ can be replaced by the force-like stimulus F_Δ using the relation

$$F_\Delta = T_\Delta (d_i^{n+1})^2. \quad (7.3)$$

One further simplification regarding remodeling is included in the model. If the influence of bending moments on the stimulus T_Δ is small compared to the influence of the forces, the stimulus at opposite beam ends is approximately the same. Reducing the number of internal variables, only two beam radii for the in-plane beam elements of the TVE are considered. Therefore, at last the average stimulus of opposite beam ends is used for the update of the beam radii.

The orientation update is independent of the thickness update. Thus, if the orientation update is carried out before the calculation of the stimulus, the thickness update does not further interact with the orientation update.

7.1.2 Reorientation

For the numerical implementation of the orientation update a case differentiation has to be done due to the symmetry of the quadrilateral microstructure as shown in Fig. 5.6. Because of the restriction on the two-dimensional case one beam axis has to be aligned with the global out-of-plane direction. The microstructure should always take the shortest way to rotate the direction of the microstructure into the direction of the strain tensor. Thus, for the two-dimensional problem, the maximum difference between both directions cannot exceed an angle of 45° , see Fig. 7.1. The evolution equation 6.7 is implemented in an implicit manner. The principal directions of a tensor can only be computed for symmetric tensors. Thus, only the symmetric part of the *Cosserat* strain tensor $\bar{\epsilon}$ is used. That leads to the update

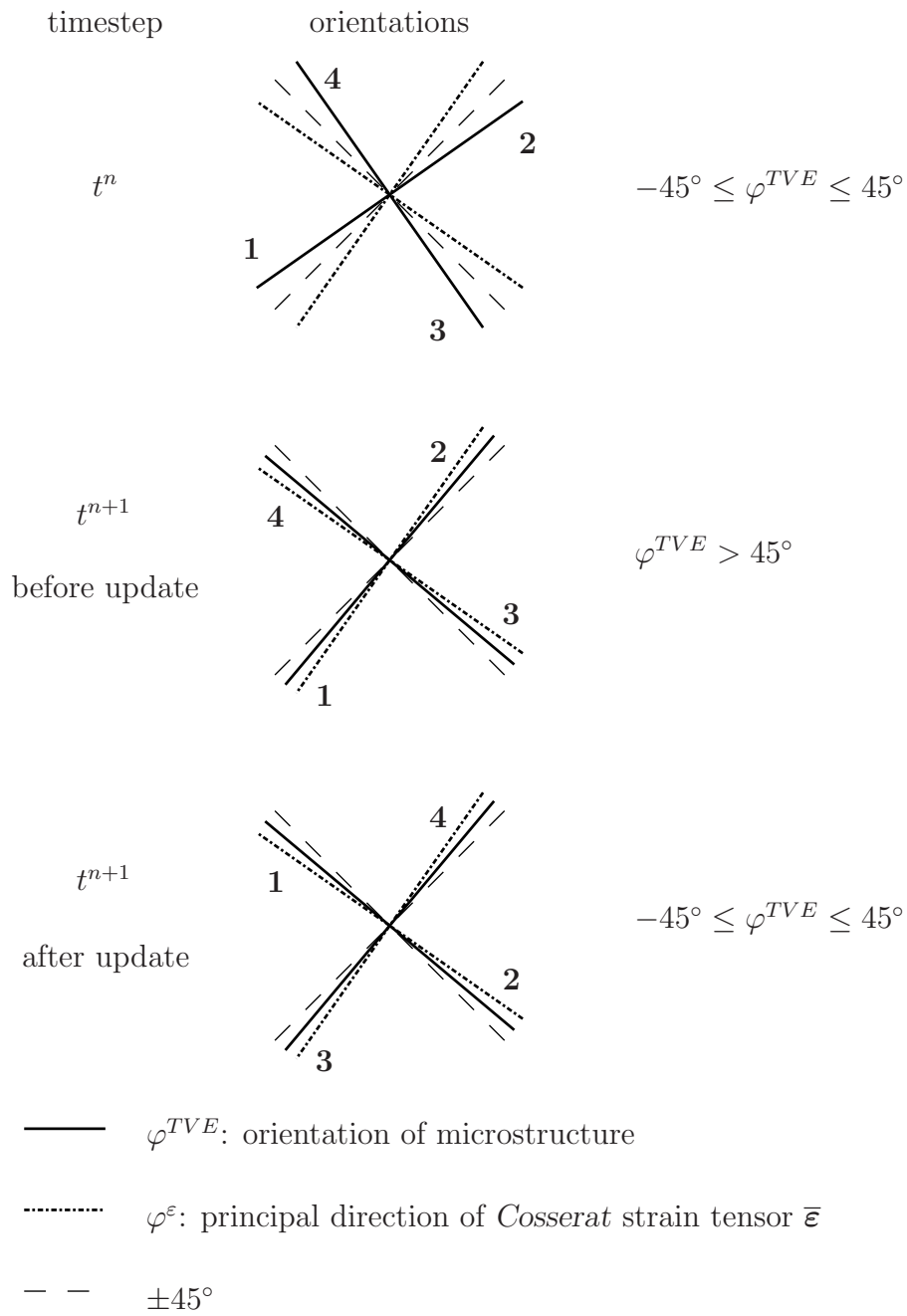


Figure 7.1: Case differentiation for orientation update

$$\varphi^{n+1} = \begin{cases} \frac{\varphi^n + C (\varphi_{\bar{\epsilon}^{sym}} + 90^\circ)}{1 + C} & \text{if } \varphi_\Delta < -45^\circ, \\ \frac{\varphi^n + C \varphi_{\bar{\epsilon}^{sym}}}{1 + C} & \text{if } \|\varphi_\Delta\| \leq 45^\circ, \\ \frac{\varphi^n + C (\varphi_{\bar{\epsilon}^{sym}} - 90^\circ)}{1 + C} & \text{if } \varphi_\Delta > 45^\circ \end{cases} \quad (7.4)$$

with the abbreviation

$$C = c \Delta t \lambda_{\bar{\epsilon}^{sym}} \quad (7.5)$$

and with the sum of the eigenvalues of in-plane directions $\lambda_{\bar{\epsilon}^{sym}}$ calculated again using the symmetric part of the *Cosserat* strain tensor $\bar{\epsilon}$ only. Thereby all directions are in the range between -45° and $+45^\circ$. That means, if the orientation quits this range, the orientation is updated by an angle of $\pm 90^\circ$ in attendance with a cyclic permutation of the thickness distribution. The procedure is demonstrated in figure 7.1 for α exceeding an angle of 45° .

The update of the orientation depends only on the strain-like quantities of the macroscale and is not influenced by the thickness update. Thus, equation 7.4 is solved first so that the stress-like quantities and thickness update are calculated with respect to the actual orientation of the TVE. Again the bisection method for the time interval Δt is used to guarantee a time-independent solution.

The complete procedure connecting strain- and stress-like quantities is presented in table 7.1.

Numerical solution scheme – FE²	
(integration point level)	
1.	Calculation of $\bar{\boldsymbol{\varepsilon}}_{IP}$ and $\bar{\boldsymbol{\kappa}}_{IP}$ from the macroscopic problem
2.	Attachment of microstructure TVE to integration point (IP) $\Omega_{IP} = \Omega_{TVE}, \Gamma_{IP} = \Gamma_{TVE}$
3.	Projection of $\bar{\boldsymbol{\varepsilon}}_{IP}$ and $\bar{\boldsymbol{\kappa}}_{IP}$ to Γ_{TVE} $\mathbf{u}^{micro} = \text{sym}(\bar{\boldsymbol{\varepsilon}}_{IP}) \cdot \mathbf{x}, \quad \bar{\boldsymbol{\varphi}}^{micro} = -\frac{1}{2} \mathbf{E} \text{skw}(\bar{\boldsymbol{\varepsilon}}_{IP}) + \bar{\boldsymbol{\kappa}} \cdot \mathbf{x}$
4.	Update of orientation of microstructure
4.1.	Analytical calculation of eigenvalues and according directions
4.2.	Update of orientation $\dot{\varphi}_{\Delta} = c \varphi_{\Delta} \lambda$
5.	Calculation of microscopic forces and moments $\mathbf{f}^{int} = \mathbf{f}^{ext}$
6.	Update of microscopic beam radii
6.1.	Calculation of stimulus T_{Δ} from microscopic forces
6.2.	Update of radii $\dot{d}_i = \begin{cases} \frac{(d_{min} - d_i) d_i}{\eta_2} & \text{if } T_{\Delta} < 0, \\ 0 & \text{if } T_{\Delta} = 0, \\ \frac{(d_{max} - d_i) d_i (T_{\Delta})}{\eta_1} & \text{if } T_{\Delta} > 0 \end{cases}$
7.	Homogenization of microscopic forces and moments $\langle \mathbf{T} \rangle = \frac{1}{V} \sum_{i=1}^N \mathbf{f}^{(i)} \otimes \mathbf{x}^{(i)}, \quad \langle \bar{\mathbf{M}} \rangle = \frac{1}{V} \sum_{i=1}^N \mathbf{m}^{(i)} \otimes \mathbf{x}^{(i)}$
8.	Mapping of homogenized forces and moments to IP $\mathbf{T}_{IP} = \langle \mathbf{T} \rangle, \quad \bar{\mathbf{M}}_{IP} = \langle \bar{\mathbf{M}} \rangle$

Table 7.1: Principal strain-driven FE² approach (SOH)

7.2 Three-dimensional implementation into explicit code LS-DYNA using FOH

Analogously to the two-dimensional implementation into the implicit code PANDAS, the evolution equations for remodeling (eq. 6.3) and reorientation (eq. 6.3) are solved, but now in an explicit way.

7.2.1 Remodeling

Again the thickness change \dot{d}_i is approximated by the thickness difference divided by the time interval Δt as done for the previous case (eq. 7.1)

$$\dot{d}_i = \frac{d_i^{n+1} - d_i^n}{\Delta t}. \quad (7.6)$$

Equation 6.3 is solved in an explicit way for the actual beam radii d_i^{n+1} for each beam element i

$$d_i^{n+1} = \begin{cases} \frac{(d_{min} - d_i^n) d_i^n}{\eta_2} \Delta t + d_i^n & \text{if } T_\Delta < 0, \\ d_i^n & \text{if } T_\Delta = 0, \\ \frac{(d_{max} - d_i^n) d_i^n (T_\Delta)}{\eta_1} \Delta t + d_i^n & \text{if } T_\Delta > 0. \end{cases} \quad (7.7)$$

Using the FOH procedure, the stimulus at opposite beam ends is identical due to the symmetry of the TVE and the applied projection scheme. Again reducing the number of internal variables, only three radii have to be stored for three independent beam directions of the TVE.

7.2.2 Reorientation

Due to the three-dimensional implementation the complexity of reorientation increases compared to the two-dimensional case. According to the underlying macroscopic *Cauchy* continuum theory, the strain tensor is symmetric. Thus, the eigenvalues and the associated directions are calculated numerically for the complete strain tensor. The following problem is to order these directions so that the rotation angle needed to rotate the TVE into the principal directions of the strain tensor gets minimal, see Fig. 6.2. This is implemented in two steps. The first one is a diagonal test, which guarantees that the angle between the diagonal of the local coordinate system of the TVE and the coordinate system constructed by the principal directions of the strain tensor gets minimal. Considering right-hand systems only, each of the three still possible remaining coordinate systems is checked separately by cyclic switch of the directions. The resulting coordinate system is that one, which allows to rotate the TVE into the principal directions of the strain tensor by a minimal angle. As a consequence the maximum angle between both coordinate system cannot exceed an angle of $\varphi_{max} = \arccos(1/\sqrt{3}) \approx 54.7^\circ$.

Then equation 6.7 is solved in an explicit way for the actual orientation of the TVE in the following form

$$\varphi_{\Delta}^{n+1} = c \varphi_{\Delta}^n \lambda \Delta t + \varphi_{\Delta}^n, \quad (7.8)$$

whereby λ ist the sum of all eigenvalues (absolute values) of the strain tensor.

Hence, as done before for the implementation into the code PANDAS, the complete procedure is presented in table 7.1.

Numerical solution scheme – FE²	
(integration point level)	
1.	Calculation of $\boldsymbol{\varepsilon}_{IP}$
2.	Attachment of microstructure TVE to integration point (IP)
	$\Omega_{IP} = \Omega_{TVE}, \Gamma_{IP} = \Gamma_{TVE}$
3.	Projection of $\boldsymbol{\varepsilon}_{IP}$ to Γ_{TVE}
	$\mathbf{u}^{micro} = \boldsymbol{\varepsilon}_{IP} \cdot \mathbf{x}$
4.	Update of orientation of microstructure
4.1.	Numerical calculation of eigenvalues and according directions
4.2.	Assembly of optimal coordinate system
4.3.	Update of orientation
	$\dot{\varphi}_{\Delta} = c \varphi_{\Delta} \lambda$
5.	Calculation of microscopic forces
	$\mathbf{f}^{int} = \mathbf{f}^{ext}$
6.	Update of microscopic beam radii
6.1.	Calculation of stimulus T_{Δ} from microscopic forces
6.2.	Update of radii
	$\dot{d}_i = \begin{cases} \frac{(d_{min} - d_i) d_i}{\eta_2} & \text{if } T_{\Delta} < 0, \\ 0 & \text{if } T_{\Delta} = 0, \\ \frac{(d_{max} - d_i) d_i (T_{\Delta})}{\eta_1} & \text{if } T_{\Delta} > 0 \end{cases}$
7.	Homogenization of microscopic forces
	$\langle \mathbf{T} \rangle = \frac{1}{V} \sum_{i=1}^N \mathbf{f}^{(i)} \otimes \mathbf{x}^{(i)}$
8.	Mapping of homogenized forces to IP
	$\mathbf{T}_{IP} = \langle \mathbf{T} \rangle$

Table 7.2: Principal strain-driven FE² approach (FOH)

Chapter 8

Numerical examples

8.1 Numerical examples calculated by PANDAS

Four numerical examples are discussed, which demonstrate the capability of the model. All examples fall back on the same set of material parameters as presented in table 8.1. However, separating the effects included by the orientation and thickness update, respectively, the update can be switched off independently. Furthermore the variation of certain material parameters will be discussed.

With the help of peripheral Quantitative Computer Tomography (pQCT) it is possible to get a reasonable distribution of the Bone Mineral Density (BMD), which can be used as a starting point for the initial distribution of the beam radii. However, the information about anisotropy is normally not provided by the pQCT, which means that neither the initial orientation of the microstructure nor the initial distribution of the trabecular beam radii in the different directions are known. Thus, considering the BMD to be an

Young's modulus	E	100000	$\frac{\text{N}}{\text{mm}^2}$
shear modulus	G	38461.54	$\frac{\text{N}}{\text{mm}^2}$
length	l	1	mm
minimum thickness	d_{min}	0.01	mm
maximum thickness	d_{max}	0.5	mm
viscous parameter growth	η_1	10000.0	$\frac{\text{N}}{\text{mm}} h$
viscous parameter atrophy	η_2	1.0	mm h
lower bound of dead zone	T_l	240	$\frac{\text{N}}{\text{mm}^2}$
upper bound of dead zone	T_u	260	$\frac{\text{N}}{\text{mm}^2}$
velocity parameter reorientation	c	0.1	$\frac{1}{h}$

Table 8.1: Material parameters (PANDAS)

average value for the region under treatment, all initial beam radii of a TVE have the same amount. For the initial orientation of the TVEs two different types of initial configurations are discussed. The first one is a homogeneous orientation with prescribed angle of rotation, the second one is a stochastic orientation of the several TVEs.

Compared to a pure macroscopic calculation the present model is numerically very expensive. Thus, it may seem reasonable to keep the number of degrees of freedom (DOF) as small as possible using linear ansatz functions for the primary variables (displacement field \mathbf{u} and rotational field $\bar{\varphi}$). However, taking a look at the formulation of the *Cosserat* strain tensor $\bar{\varepsilon}$ (eq. 3.21), where the gradient of the displacement field $\text{Grad } \mathbf{u}$ is coupled with the rotational field $\bar{\varphi}$ directly, it may be a better choice to choose quadratic ansatz functions for the displacement field \mathbf{u} and linear ansatz functions for the rotational field $\bar{\varphi}$. Consequently the contribution of both fields to the

strain tensor is linear and thereby compatible. This type of formulation with higher ansatz functions for the displacement field \mathbf{u} than for the rotational field $\bar{\varphi}$ is known in literature as *Taylor-Hood* formulation [9].

Thus, the first example investigates the difference between the simplest formulation using linear ansatz functions only and the *Taylor-Hood* formulation using quadratic ansatz function for the displacement field and linear ansatz functions for the rotational field. Due to the underlying macroscopic *Cosserat* continuum theory the model is able to represent boundary layer effects. Within the classical *Cosserat* theory the so-called internal length scale λ_C drives the distribution of the quantity within the boundary layer. By comparison the second example investigates the influence of the microstructural topology on the boundary layer effect. The third example discusses the influence of different initial conditions and the last example studies the interaction between an inserted screw and the surrounding bone material.

8.1.1 Comparison of ansatz functions

In the following eight different discretizations are compared to each other: four discretizations using quadrilateral elements (QUAD) and four discretizations using triangular elements (TRIA), see table 8.2, each with an application of a *Taylor-Hood* (TH) formulation, which means higher ansatz functions for the displacement field \mathbf{u} than for the rotational field $\bar{\varphi}$, and with application of linear ansatz functions (LL) for both fields, which is the simplest choice. Furthermore, each formulation is checked on a fine as well as on a coarse discretization. One expects that for a fine discretization the results coincide – analogously to the h -adaptivity – while for a coarse discretization the results may differ due to the lack of certain ansatz functions to represent the actual distribution of the quantity. To keep the numerical effort of the quadrilateral and the triangular discretization in the same order, the fineness of the meshes is chosen in such a way, that the number of DOF is approximately the same using the *Taylor-Hood* formulation, while for the linear ansatz functions the same mesh as for the *Taylor-Hood* formulation is used. Table 8.2 contains the number of elements as well as the number of DOF. The figures have to be comprehended symbolically and do not reflect

the actual discretization.

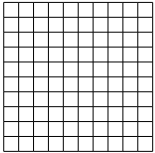
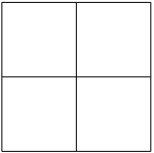
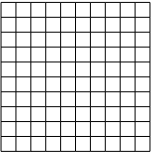
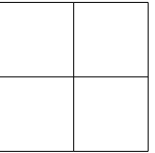
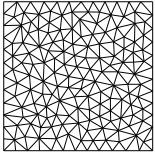
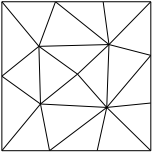
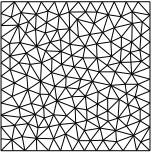
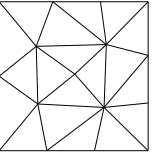
No.	1	2	3	4
mesh				
type	QUAD	QUAD	QUAD	QUAD
ansatz \mathbf{u}	quadratic	quadratic	linear	linear
ansatz $\bar{\varphi}$	linear	linear	linear	linear
elements	10 000	400	10 000	400
DOF	71 003	3 003	30 603	1 323
No.	5	6	7	8
mesh				
type	TRIA	TRIA	TRIA	TRIA
ansatz \mathbf{u}	quadratic	quadratic	linear	linear
ansatz $\bar{\varphi}$	linear	linear	linear	linear
elements	15 572	627	15 572	627
DOF	71 007	3 007	23 919	1 053

Table 8.2: Comparison of ansatz functions

Figure 8.1 shows the shear test boundary value problem with the according dimensions, which is used to compare the different discretizations. A shear experiment is chosen, because it is known from the macroscopic *Cosserat* continuum theory that a boundary layer arises and the investigated ansatz functions may especially fail in the approximation of the distribution of the quantity within the boundary layer. At the bottom the sample is fully constrained, at the top the vertical displacement u_2 and the rotation $\bar{\varphi}$ are constrained and a constant horizontal displacement $u_1 = 1$ mm is prescribed. No boundary conditions are applied on the left and right boundary of the sample.

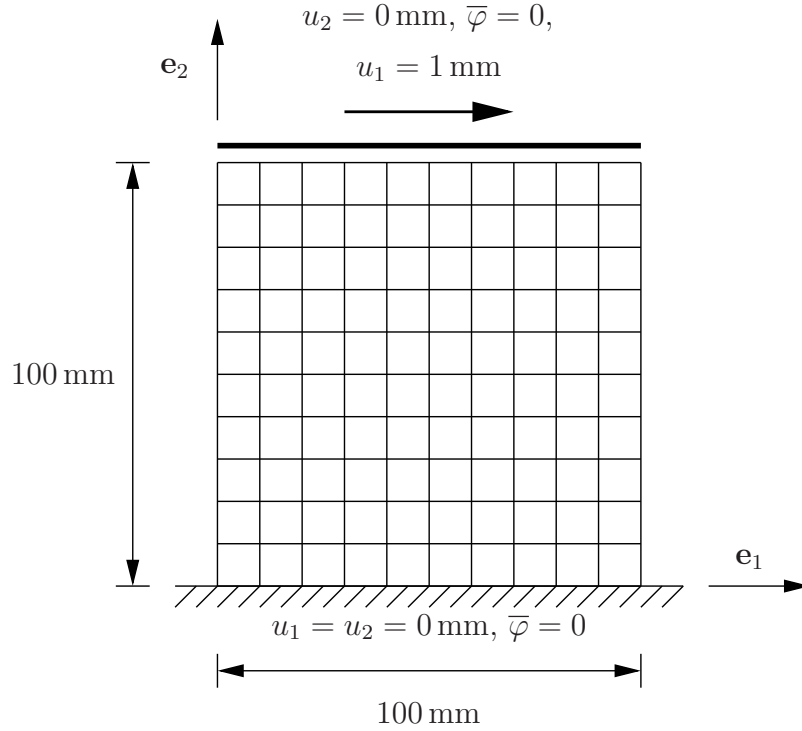


Figure 8.1: Boundary value problem of shear test

In Figure 8.2 the numerical results at time $t = 1 \text{ h}$ are shown for the reference solution using 40 000 quadrilateral elements with *Taylor-Hood* formulation. The quantities under consideration are the symmetric part of the shear stress $\tau = \frac{1}{2}(T_{12} + T_{21})$ reflecting the main load transfer, the component \bar{M}_{32} of the couple stress tensor, which is sensitive with respect to the boundary layer effect, the average growth variable $\delta = \frac{1}{2}(d_1 + d_2)$ and the actual orientation of the TVE φ^{TVE} . Figure 8.3 demonstrates that the results for d_1 and d_2 can not be interpreted separately, because it depends on the orientation of the microstructure, if the thickness change of a microstructural beam element contributes to the variable d_1 or to the variable d_2 . The calculation of the equivalent stress T_{eq} does not differ between tensile stresses and compressive stresses, which means that the distribution of the quantity is symmetric with respect to the horizontal and vertical symmetry axis. But due to the influence of the microstructural orientation, the results for the variables d_1 and d_2 , respectively, are not symmetric themselves. Thus, except for Figure 8.3, the

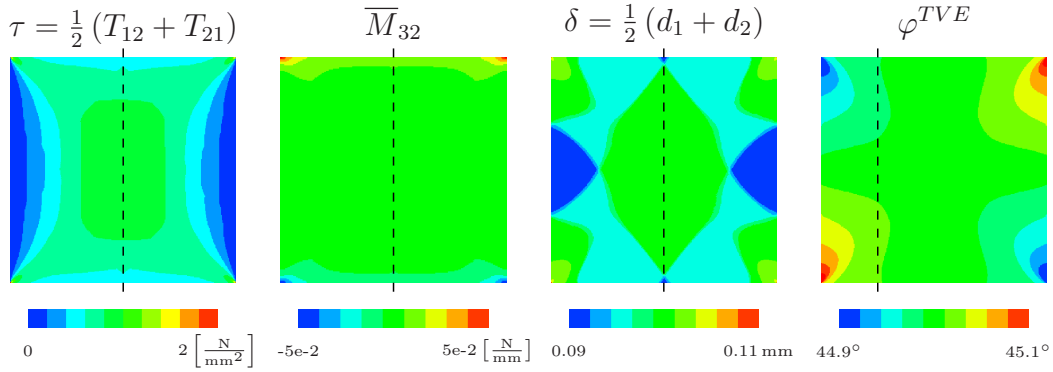
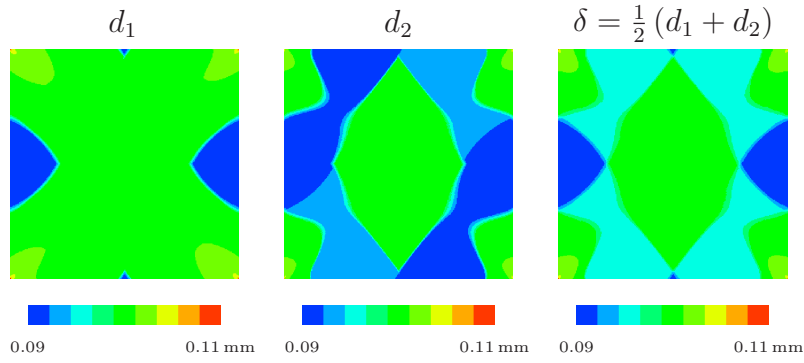


Figure 8.2: Numerical results of reference solution

Figure 8.3: Absent axial symmetry of thickness change d_1 and d_2

results for the thickness increase and thickness decrease of the beam elements (d_1 and d_2) are always presented in the form of the average quantity δ .

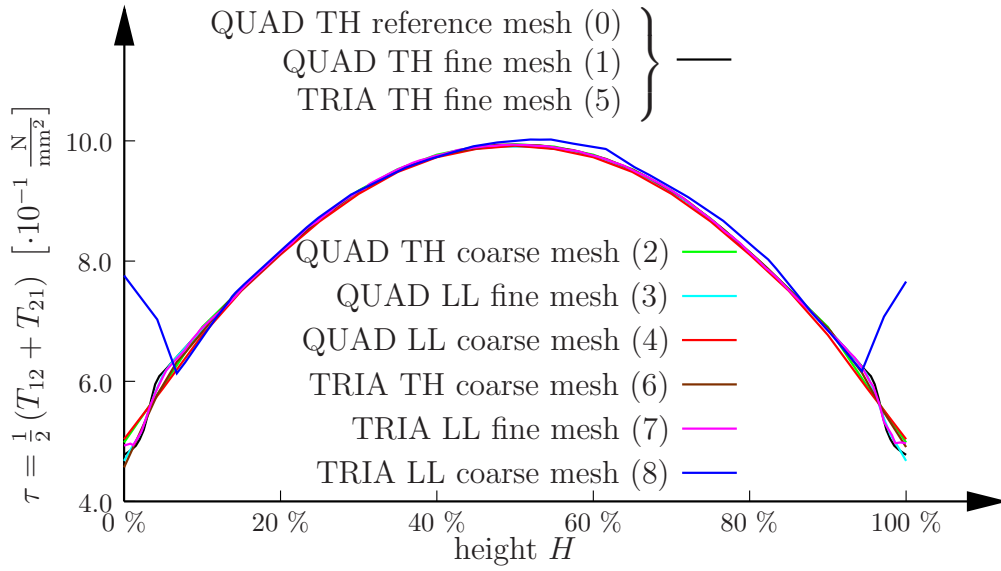
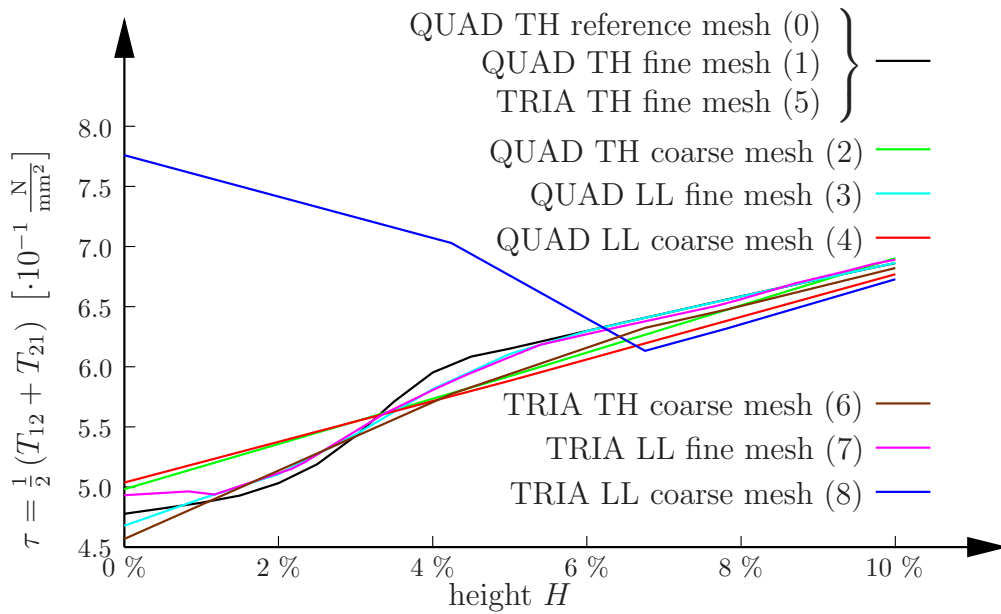
The numerical results will be compared at the according cutting line as illustrated in Fig. 8.2. The results for the symmetric shear stress τ , the couple stress tensor component \overline{M}_{32} and the average thickness change δ are evaluated at the vertical symmetry line of the model. By contrast the actual orientation of the TVE φ^{TVE} is evaluated at a quarter of the width, because the initial orientation is 45° and due to symmetry and shear loading, the principal direction of the strain tensor at the vertical symmetry line is also 45° , so that the orientation remains constant there if there are no other effects involved by thickness change, as will be seen later. The numbers of the

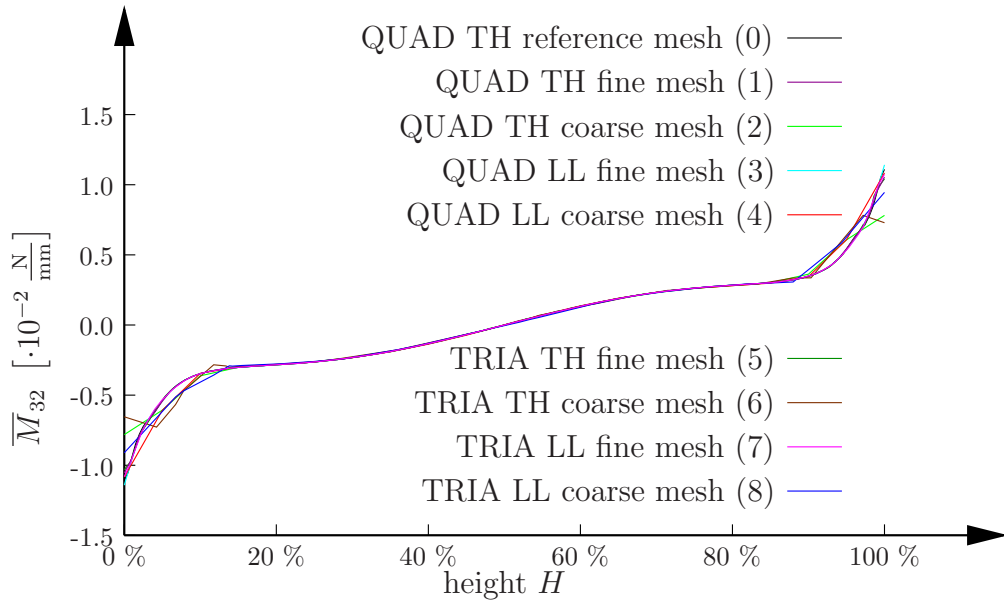
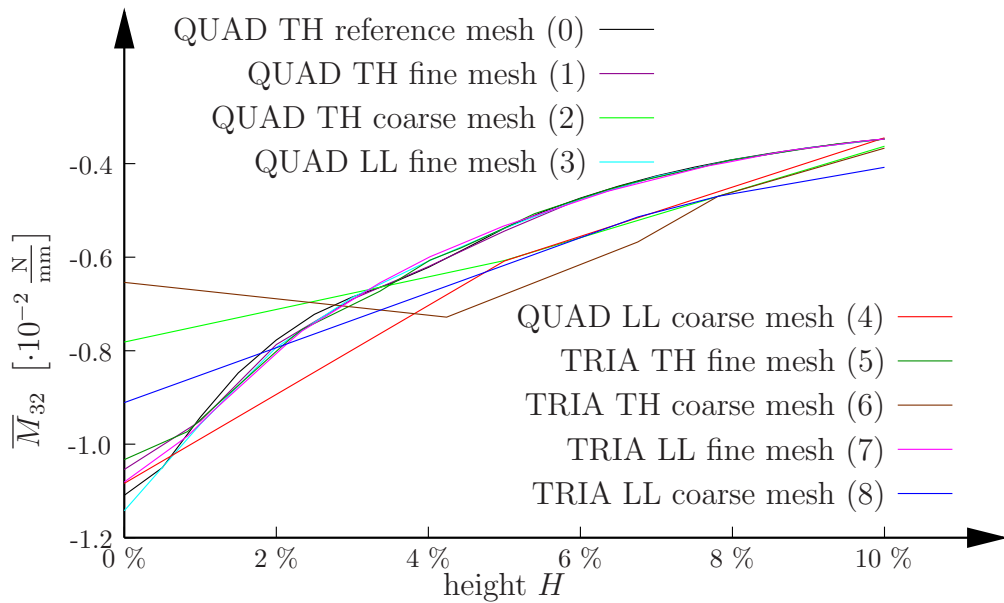
curves correspond to the numbers given in table 8.2, whereby the reference solution has the number 0.

Figure 8.4 shows the results of the symmetric part of the shear stress τ . In the inner of the sample (height H in the range of $10\% < H < 90\%$) the results are nearly identical apart from the last solution (No. (8)) using a coarse discretization by triangular elements and linear ansatz functions. The reason for it is the bad approximation of the principal direction of the strain tensor by the triangular element as will be seen later in Fig. 8.10. For the discussion of the effects in the boundary layer, the range $0\% < H < 10\%$ is plotted in a separate diagram (Fig. 8.5). It is clear that a certain mesh fineness is needed so that the S-shaped boundary layer effect can be represented. Otherwise the effect will be smoothed out (No. (2), (4), (6), (8)). Using linear ansatz functions but a fine discretization (No. (3), (7)) still yields different results. Only if the *Taylor-Hood* formulation is used (No. (1), (5)) the solutions coincide with the reference solution.

Figure 8.6 shows the results for the couple stress tensor component \overline{M}_{32} . In the inner of the sample the curves are in good agreement, but in the range of the boundary layer the differences are obvious, see Fig. 8.6. The component \overline{M}_{32} does not decay to the value zero outside the boundary layer, but this effect will be discussed on the basis of the following example investigating the influence of the microstructural parameter on the boundary layer effect. Taking a look at Fig. 8.6, one can see the smoothening of the boundary layer effect using coarse discretizations. For the range $1\% < H < 99\%$ the differences between the curves for fine discretizations are tolerable. Inversely that means that the main error results from the top and bottom layers of elements, where the steep gradient of the boundary layer effect is represented very poorly.

The boundary layer effect of the average thickness change variable δ (Fig. 8.8) does not result from the boundary layer effect of the couple stress tensor component \overline{M}_{32} (in this case one would expect an increase of the variable at the boundary layer) but it results from the lower equivalent stress T_{eq} at the boundary, which is qualitatively closely related to the distribution of the symmetric part of the shear stress τ , see Fig. 8.2. The small overshoots present at the transition from the boundary layer to the inner of the sample do not result from the numerical model (they are not present plotting the in-

Figure 8.4: Numerical results of τ at cutting lineFigure 8.5: Numerical results of τ at cutting line (detail)

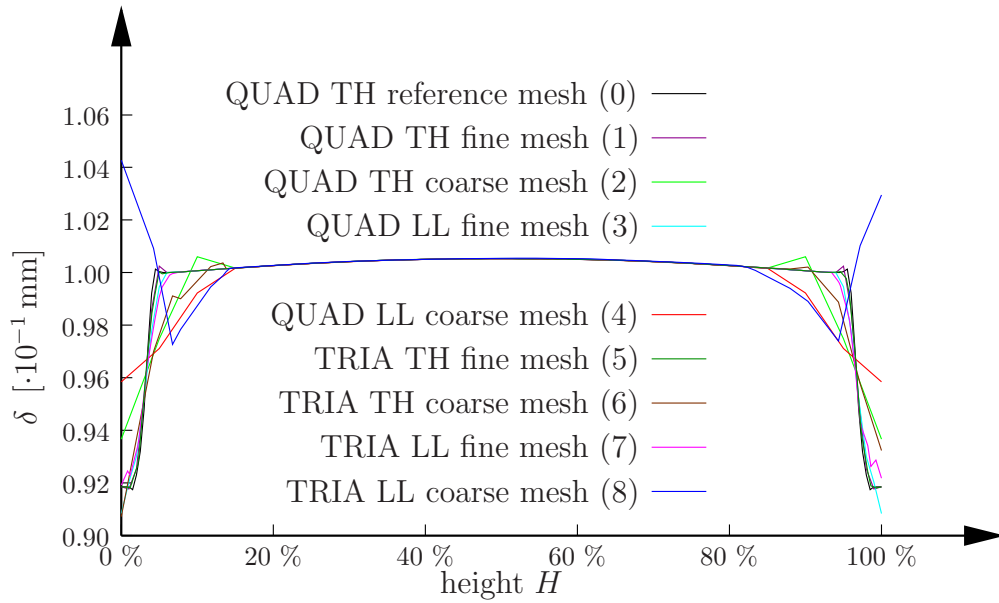
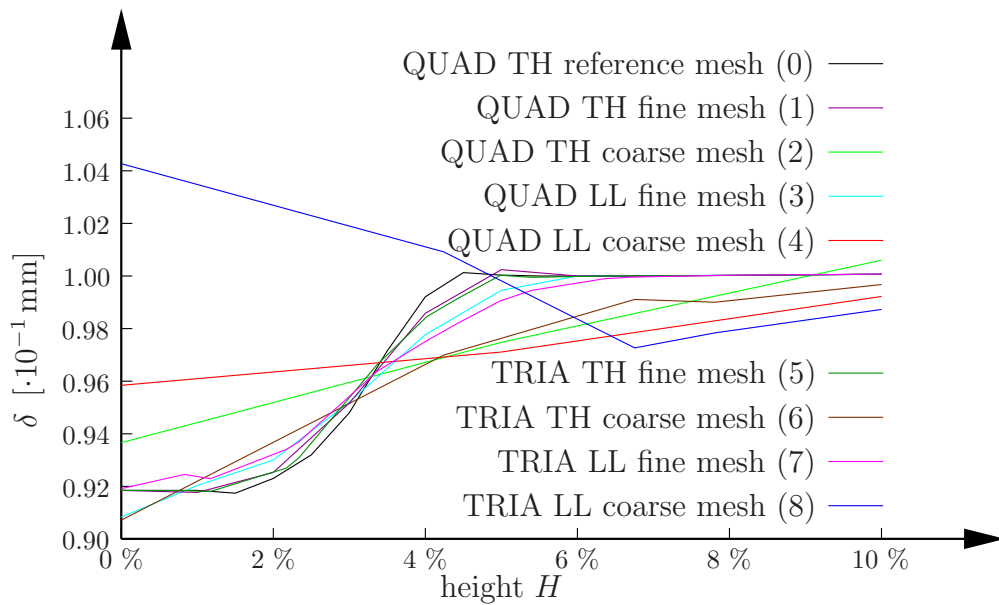
Figure 8.6: Numerical results of \bar{M}_{32} at cutting lineFigure 8.7: Numerical results of \bar{M}_{32} at cutting line (detail)

ternal variables at the integration points) but they result from the projection of the non-steady variable provided at the integration point to the boundary of the element followed by an averaging of the quantity for adjacent elements contributing to the quantity.

Again the boundary layer effect is smoothed using a coarse discretization. Taking a look at the range near the boundary ($0\% < H < 10\%$, see Fig. 8.9) one observes that even the reference solution is not able to represent the direct decline from the initial thickness to the reduced thickness, which should be constant within the boundary layer. The reason for it is that if the stimulus is smaller than zero, the decrease is independent of the amount of the stimulus. The results show that approximately four layers of elements are needed to represent the steep gradient. The four layers correspond for the reference solution with 200 elements in direction of height to a thickness of 2% and for the fine solution with 100 elements in direction of height to a thickness of 4%.

At last the results for the actual orientation φ^{TVE} of the TVE are presented (Fig. 8.10). Only the solutions using coarse discretizations and linear ansatz functions deviate from the reference solution. The actual orientation is mainly influenced by the principal direction of the strain tensor. That suggests the assumption that the differences result from the lacking ability of the elements using linear ansatz functions to represent the principal direction of the strain tensor correctly. That also explains why the results for the quadrilateral element are much better than the results for the triangular element. For the triangular element the principal directions are calculated from the information of three nodes. In contrast for the quadrilateral element the information at four nodes is available to calculate the principal strain directions.

This first example shows that the *Taylor-Hood* formulation is always preferable compared to a formulation using linear ansatz functions only. That holds for the quadrilateral elements as well as for the triangular elements. Furthermore a certain mesh fineness is required to capture the steep gradients involved in the model by the boundary layer effect resulting from the underlying macroscopic *Cosserat* continuum theory and by the steep gradient resulting from the evolution equation for decreasing thickness being independent of the stimulus' amount.

Figure 8.8: Numerical results of δ at cutting lineFigure 8.9: Numerical results of δ at cutting line (detail)

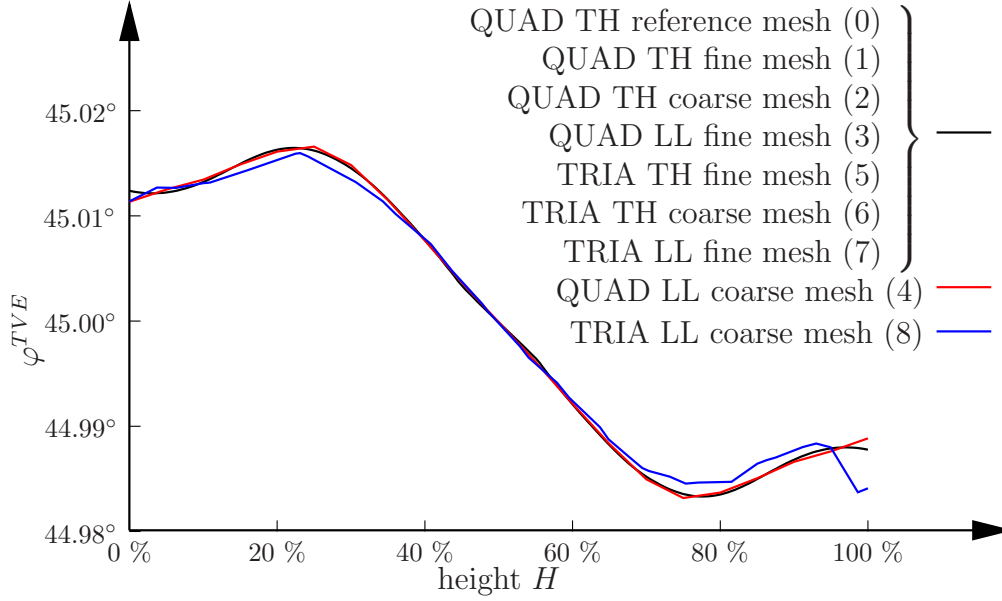


Figure 8.10: Numerical results of φ^{TVE} at cutting line

8.1.2 Influence of parameters on boundary layer effect

The second example investigates the influence of the microstructural parameters on the boundary layer effect, namely the beam thicknesses d_1 and d_2 and the beam length l even the beam length l is kept constant within the FE^2 model. The boundary layer effect results from the underlying macroscopic *Cosserat* continuum theory but not from the modeling of the adaptation process. Thus, for this example adaptation processes are neglected ($c \rightarrow 0$; $\eta_1 \rightarrow \infty$; $\eta_2 \rightarrow \infty$). The same boundary conditions are used as for the previous example, see Fig. 8.1.

The results will be discussed for the orientations $\varphi^{TVE} = 0^\circ$ and $\varphi^{TVE} = 45^\circ$. The variation of the microstructural parameters affects the boundary layer, as e. g. present for the couple stress tensor component \overline{M}_{32} , but hardly influences the distribution of other quantities like the symmetric part of the shear stresses τ . This is demonstrated exactly for those quantities, the couple stress tensor component \overline{M}_{32} and the symmetric part of the shear stresses τ .

The first figure (Fig. 8.12) shows the effect of scaling the TVE by a factor of 0.25 up to a factor of 4. The upper part shows the results for the orientation of $\varphi^{TVE} = 0^\circ$, the lower part gives the results for the orientation of $\varphi^{TVE} = 45^\circ$. For both orientations the thickness of the boundary layer as well as the absolute value of the quantity itself at the boundary increases for the couple stress tensor component while the influence on the symmetric shear stress is very small. The main difference between both orientations is the fact that for the orientation of $\varphi^{TVE} = 0^\circ$ the quantity decays to the value zero while for the orientation of $\varphi^{TVE} = 45^\circ$ the quantity takes the value zero only in the middle due to skew symmetry. The reason for it is shown in figure 8.11. Thereby black color indicates the initial configuration and red color the actual configuration. The figures have to be understood schematically and do not result from a FE calculation because even for small deformations in case of the X-like microstructure ($\varphi^{TVE} = 45^\circ$) buckling occurs. The figures show only the main topic of interest, which is the difference in the load carrying behavior between boundary layer and the inner of the sample (the boundary layer effects on the left and right boundary for the X-like microstructure are not represented correctly). For the cross-like microstructure ($\varphi^{TVE} = 0^\circ$) the load is carried by bending of the beam rows on top and bottom and only in the inner the load is carried in addition by stretching of the beam elements. Thus, the curvature at the boundary is much higher than the curvature in the inner of the sample. The couple stress tensor component \overline{M}_{32} is the dual quantity with respect to the curvature $\overline{\kappa}_{32}$. Thus, this effect is also represented by the couple stress tensor component. By contrast for the X-like microstructure also the beam elements on top and bottom are mainly loaded by stretch due to the nearly optimal orientation of the microstructure so that the curvature at the boundary is of the same order as in the inner of the sample.

The second figure (Fig. 8.13) shows the effect of scaling the beam length l but keeping the beam thicknesses d_1 and d_2 constant. Scaling of the beam length but not of the beam thicknesses is accompanied by a variation of the density. This effect is eliminated by multiplication of all results with the factor $(\frac{l}{\delta})^2$. One can see that increasing the beam length l also increases the thickness of the boundary layer of the couple stress tensor component \overline{M}_{32} . That holds for both orientations. Thereby the absolute value at the boundary is more or less independent of the beam length l . Again the distribution of the symmetric stresses τ is hardly influenced by increasing the size of the

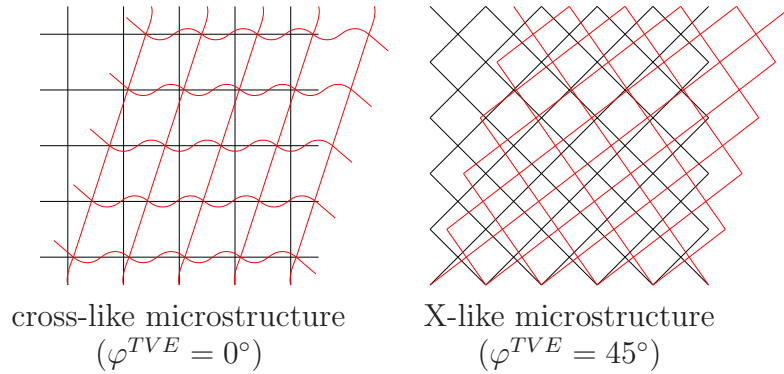
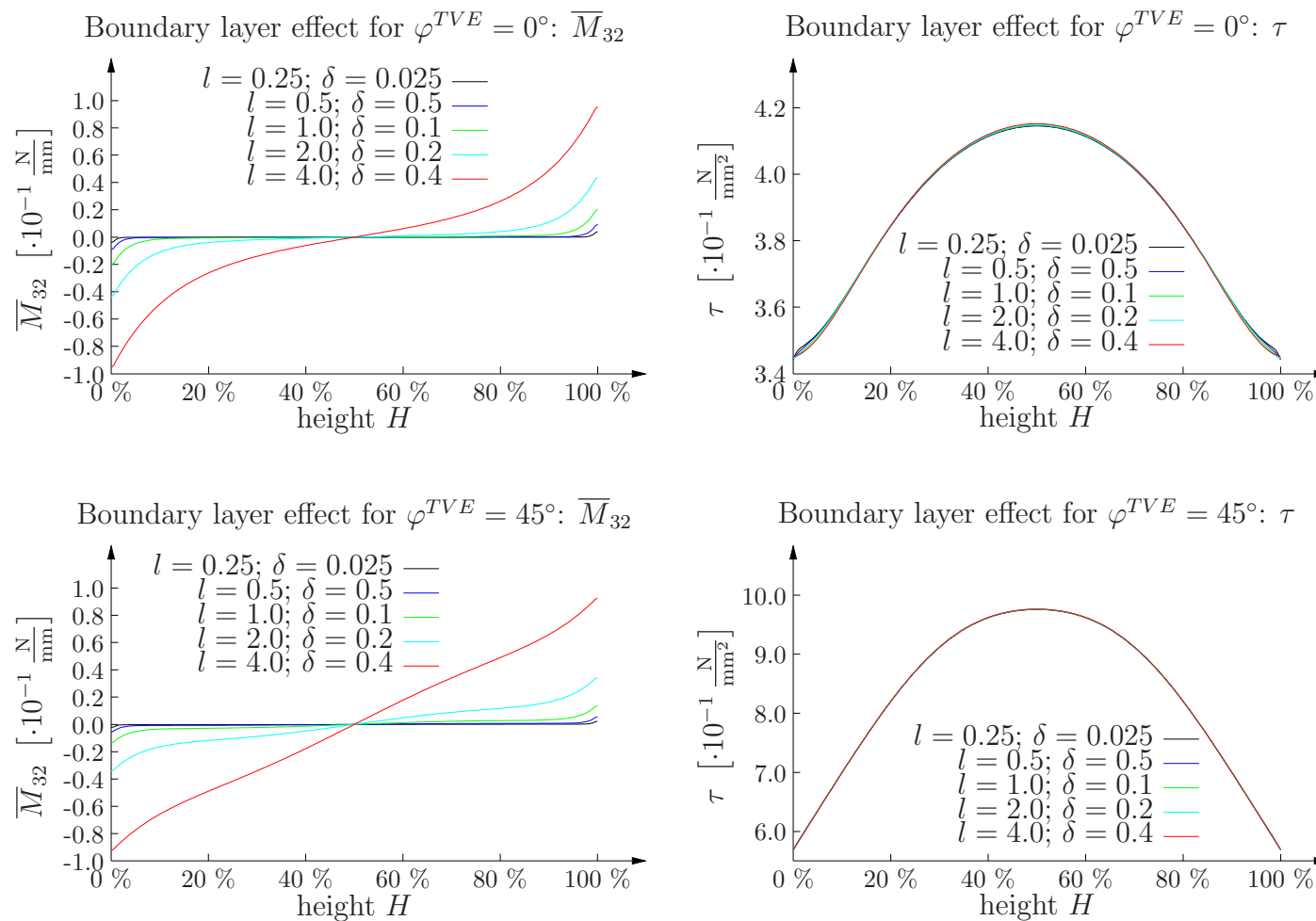


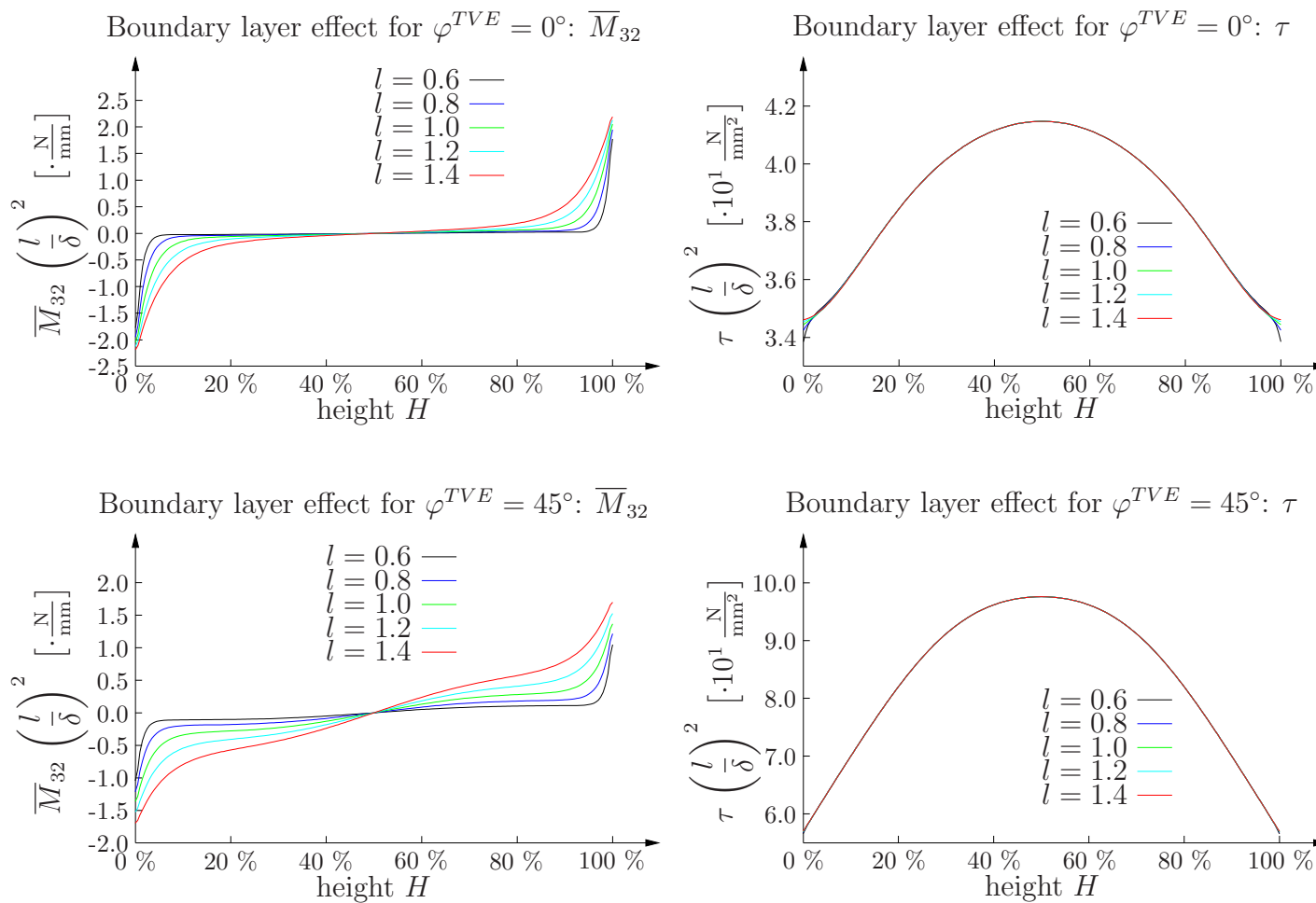
Figure 8.11: Different load carrying behavior of microstructures

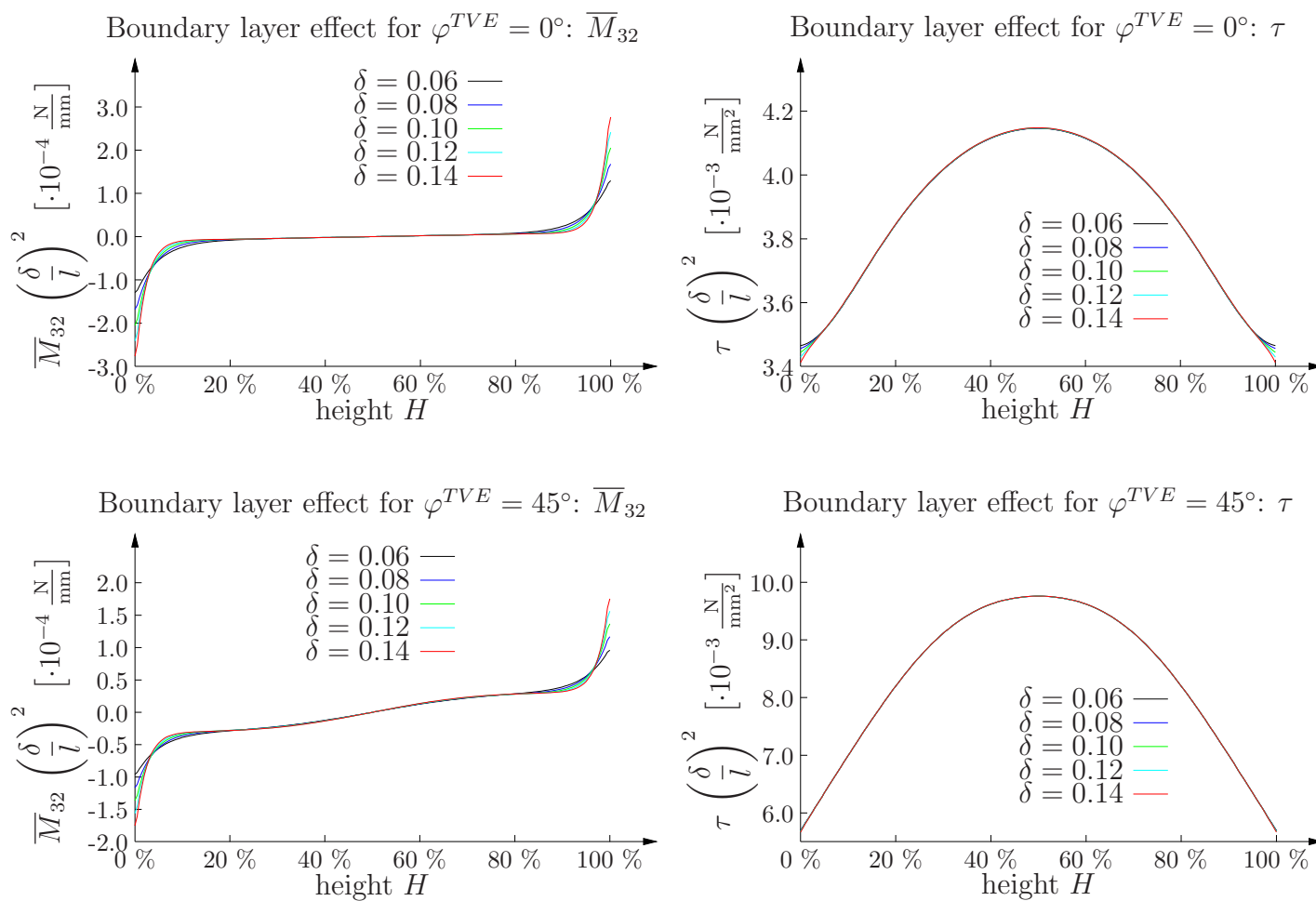
beam length l .

The third figure (Fig. 8.14) shows the influence of scaling the beam thicknesses d_1 and d_2 but keeping the beam length l constant. Again the effect of changing the density is eliminated by multiplication of the results with the factor $(\frac{\hat{\rho}}{\hat{l}})^2$. Scaling the beam thicknesses mainly influences the gradient of the quantity, here the couple stress tensor component \overline{M}_{32} . It seems that the integral of the quantity within the boundary layer is nearly the same and that a fixpoint exists in the inner of the boundary layer, which is crossed by each curve. Accordingly the absolute value at the boundary increases for increasing beam thicknesses. And again the influence on the symmetric shear stress τ is marginal.

This example shows how to control the boundary layer effect of the model by the microstructural beam parameters l , d_1 and d_2 . The classical *Cosserat* continuum theory only knows one parameter, which drives the distribution of the quantity within the boundary layer. This parameter is the so-called internal length scale, often abbreviated as λ_C . By contrast, the present FE² model includes two parameters (assuming $d_1 = d_2$ because anisotropy is not included in the classical *Cosserat* model).

Figure 8.12: Boundary layer effect scaling size of TVE (l/δ constant)

Figure 8.13: Boundary layer effect scaling length l (δ constant)

Figure 8.14: Boundary layer effect scaling thickness δ (l constant)

8.1.3 The influence of the initial conditions

The third example investigates the influence of the initial conditions on the converged solution, namely the initial conditions of the thickness distribution and the orientation of the TVE. Considering the application of the model to real patient specific data derived by computer tomography, the *Hounsfield* unit distribution provides an informative basis for the initial conditions of the thickness distribution. However, it is difficult to extract information concerning the initial orientation from the CT data. Therefore the following example studies the influence of varying the initial conditions. The same boundary conditions are used as presented in Fig. 8.1.

Figure 8.15 shows the numerical results for different initial orientations: an orientation of 45° , which is the optimal orientation with respect to the applied shear test, an orientation of 0° , which is the worst orientation with respect to the applied shear test, and a stochastic orientation. While in the outer regions of the sample the results are more or less the same, especially in the inner of the sample considerable differences appear, which affect all of the presented quantities. The reason for it is the formation of bands with larger beam thicknesses and lower beam thicknesses, respectively. These bands propagate in the direction of the principal loading ($\pm 45^\circ$). The initial conditions now have a strong influence, where the bands start to develop determining the number of bands and in which direction the bands expand. For the orientation of 45° this results in a formation of 6 bands in direction of -45° , for the orientation of 0° in a formation of 12 bands in direction of 45° and for the stochastic orientation in a formation of 8 bands again in direction of -45° . The number of bands depends on the initial conditions but not on the discretization. The reason for it is that local stress peaks appear at different locations serving as starting points for the formation of bands. However, the locations of the stress peaks are independent of the discretization due to the underlying regularizing *Cosserat* continuum theory. This is confirmed by the observation that the bands have a certain thickness, which is also independent of the discretization. The couple stress tensor component \overline{M}_{32} interacts with these bands. Similarly to the boundary layer effects, where the sample behaves stronger or softer due to the applied boundary conditions, couple stresses arise where the beam thicknesses change significantly. This then also effects the orientation of the microstructure φ^{TVE} , which is in the

equilibrium state identical with the principal strain direction φ_ε .

The same effect can be observed varying the initial beam thicknesses instead of the initial orientation (Fig. 8.16). Again the initial conditions have a strong influence on the number and orientation of bands in the inner.

Figure 8.17 shows exemplarily the principal stress and strain directions using an initial orientation of 45° and an initial beam thickness δ of 0.1 mm. One can see that in contrast to the principal strain direction φ_ε the principal stress direction in the inner follows the continuum solution and is not affected by the formation of bands.

In summary one can say that the initial conditions have a strong influence on the local behavior but not on the overall global behavior as the effect on the symmetric part of the shear stress τ is not enormous.

One may argue that the applied boundary value problem is not well-suited to investigate the effect of different initial thicknesses. Considering a single beam element loaded by constant *Dirichlet* boundary conditions leading to growth due to a positive stimulus, the beam element will try to achieve the maximum thickness. The reason for it is that the cross sectional area increases in the same way as the resultant forces at the boundary so that the stimulus is in this case independent of growth. Thus, a second more realistic boundary value problem is shown in addition to the previous example applying *Neumann* boundary conditions as shown in Fig. 8.18, whereby the model is fixated against free horizontal displacement. The numerical results are presented in Figure 8.19. However, the results show that even in this case the selection of the initial thickness does not play an important role.

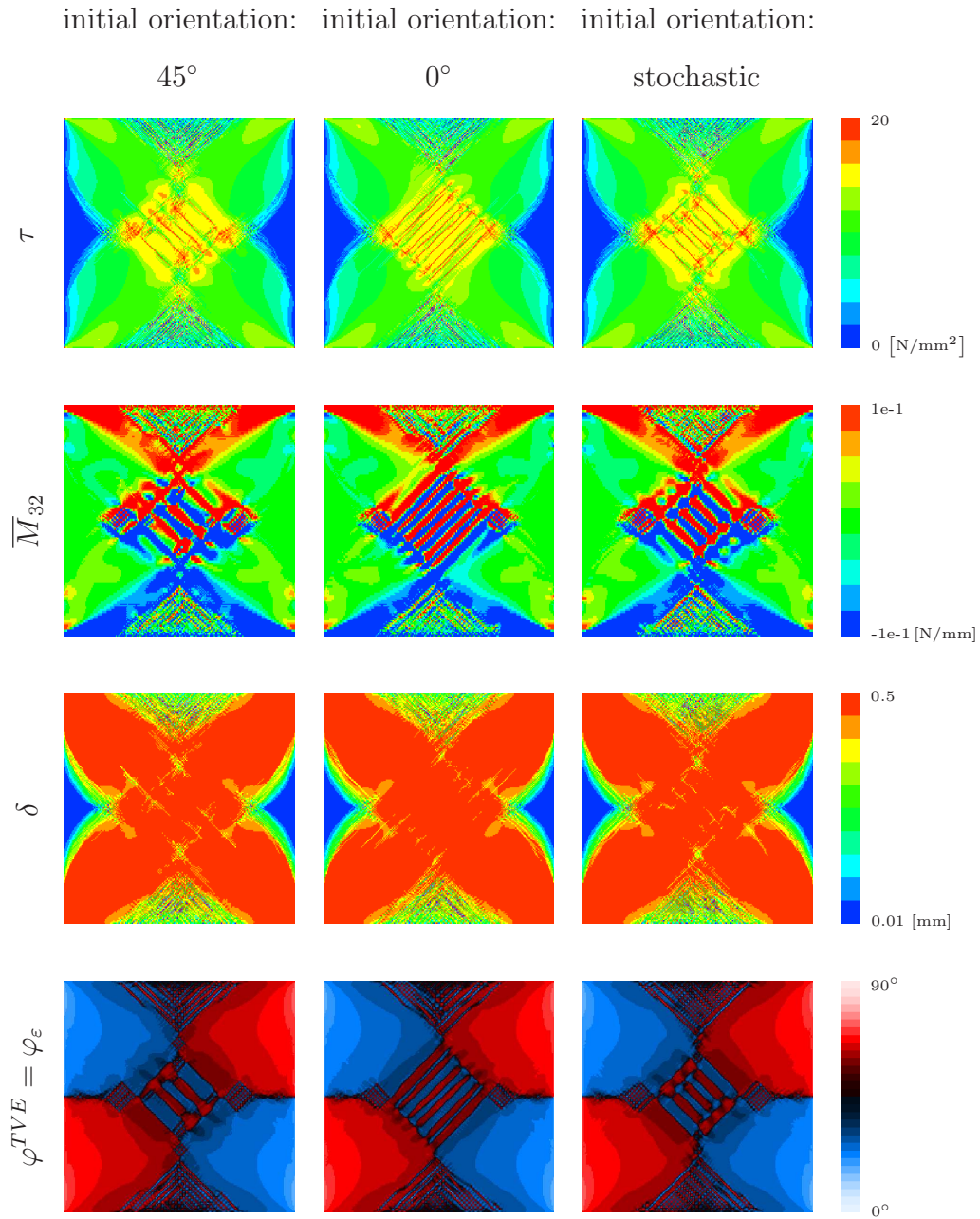


Figure 8.15: Converged solutions for different initial orientations

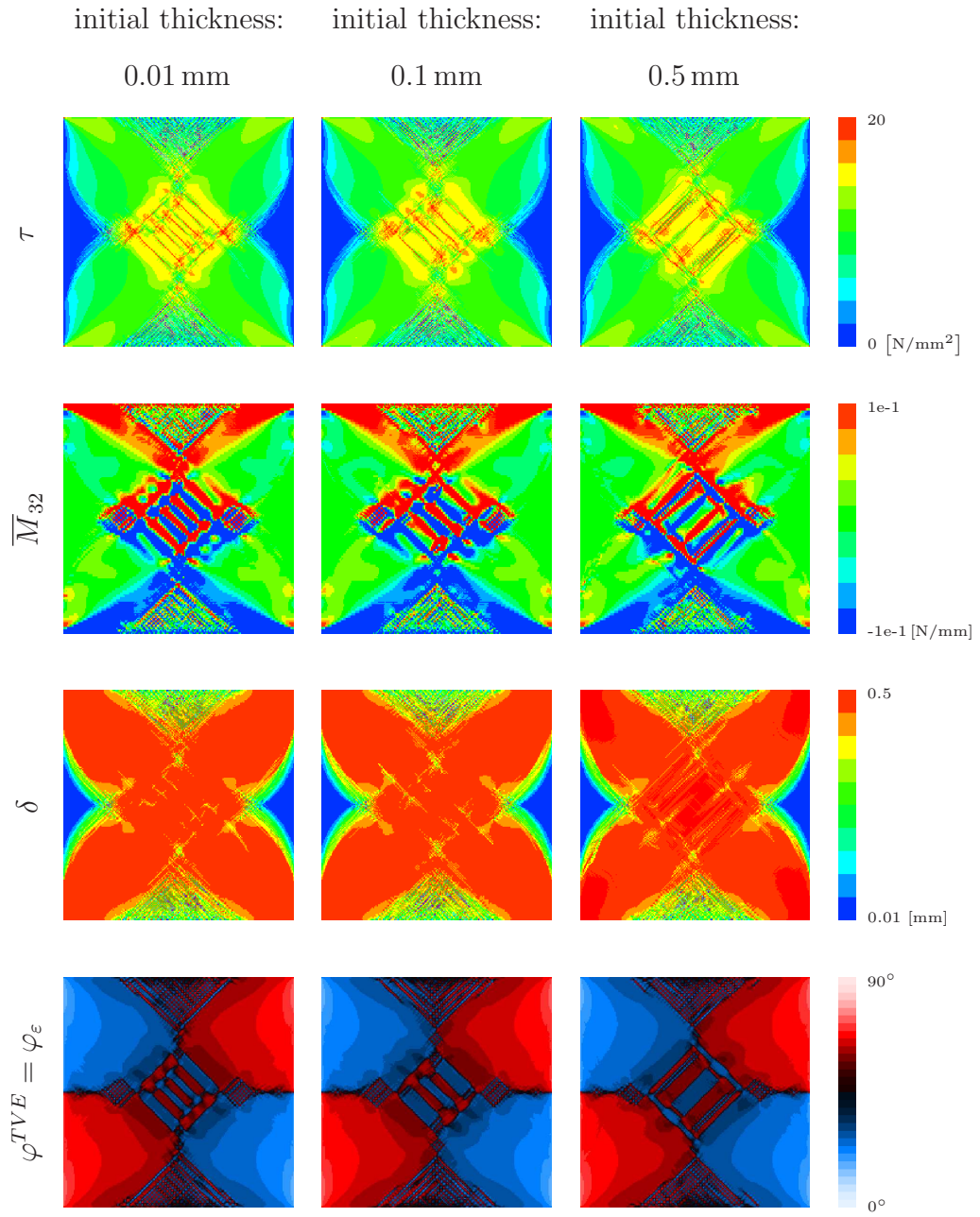


Figure 8.16: Converged solutions for different initial thicknesses

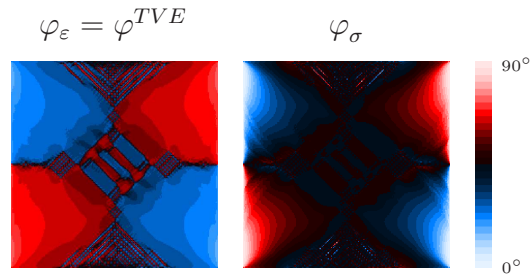


Figure 8.17: Comparison of principal directions

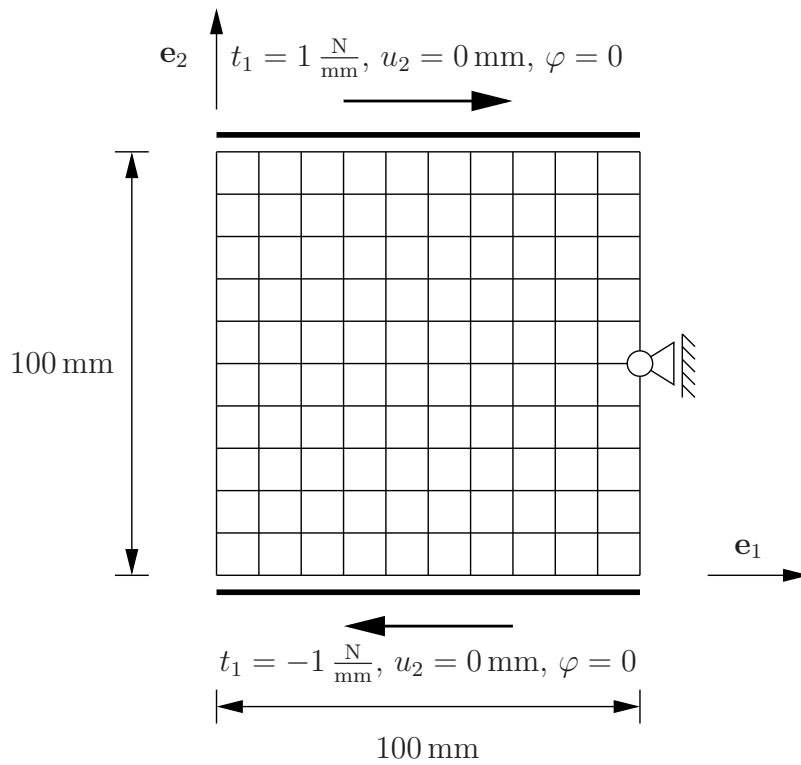


Figure 8.18: Boundary value problem of shear test (Neumann BC)

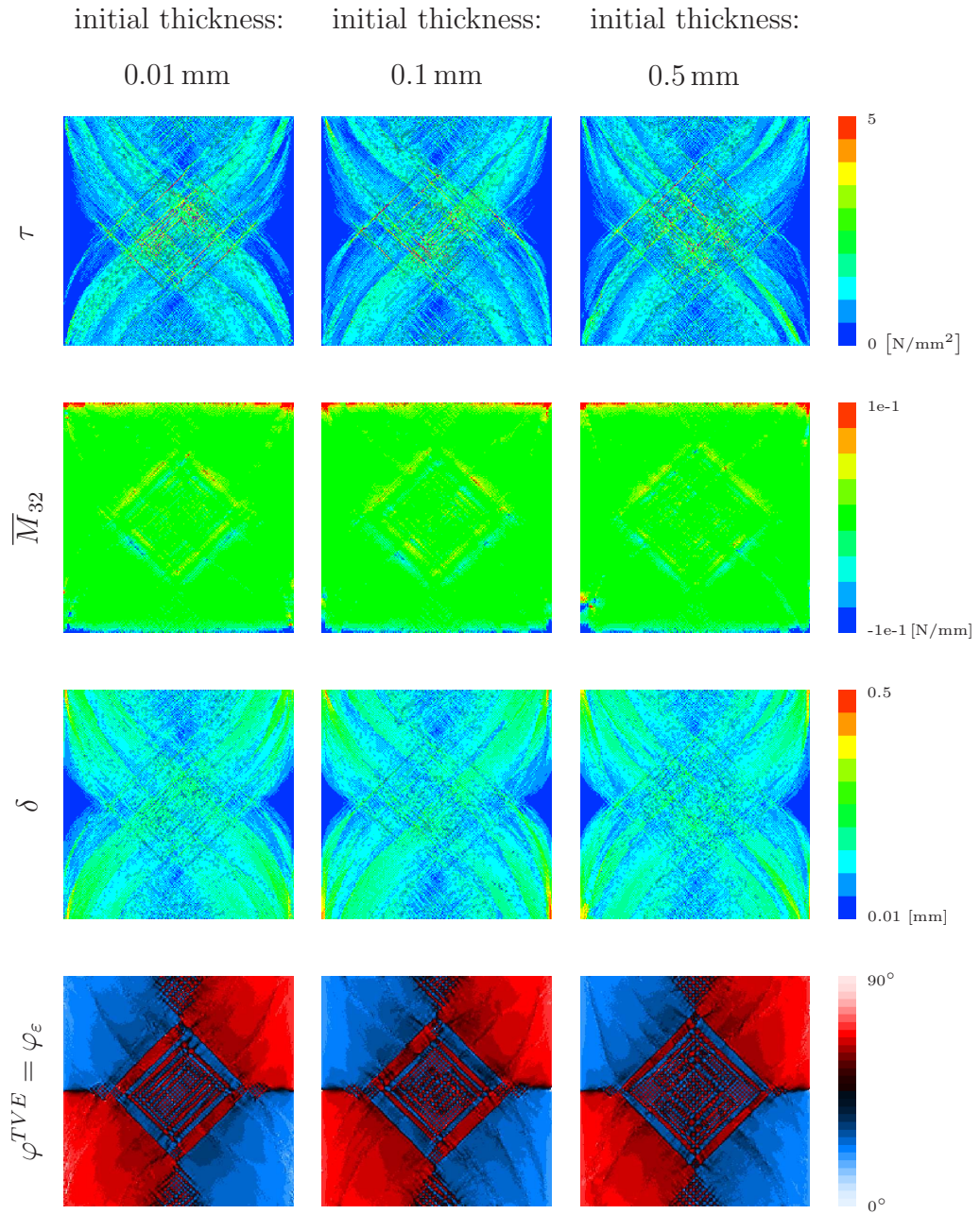


Figure 8.19: Converged solutions for different initial thicknesses (stress BC)

8.1.4 Interaction of model with inserted screw

The last example calculated by PANDAS studies the effect of inserting a screw into the material. The main difference with respect to the previous examples is the fact that now due to the geometry stress peaks appear at the tip of the thread, which will serve as nuclei for the formation of growth bands. Figure 8.20 shows the dimension of the boundary value problem as well as the applied boundary conditions. A screw is pulled out from the sample which is completely fixated at top and bottom. Three different screw geometries are investigated: while the inner diameter and the pitch are constant, the thread depth is varied from 0 mm (no thread present) to 4 mm. Ideal contact is assumed. The screw has the same stiffness as the bulk material of the trabecular beam elements so that the screw is comparatively stiff with respect to the bone-like material. The main interest is on the neighborhood of the screw. Thus, a finer discretization than the discretization at top and bottom is used there.

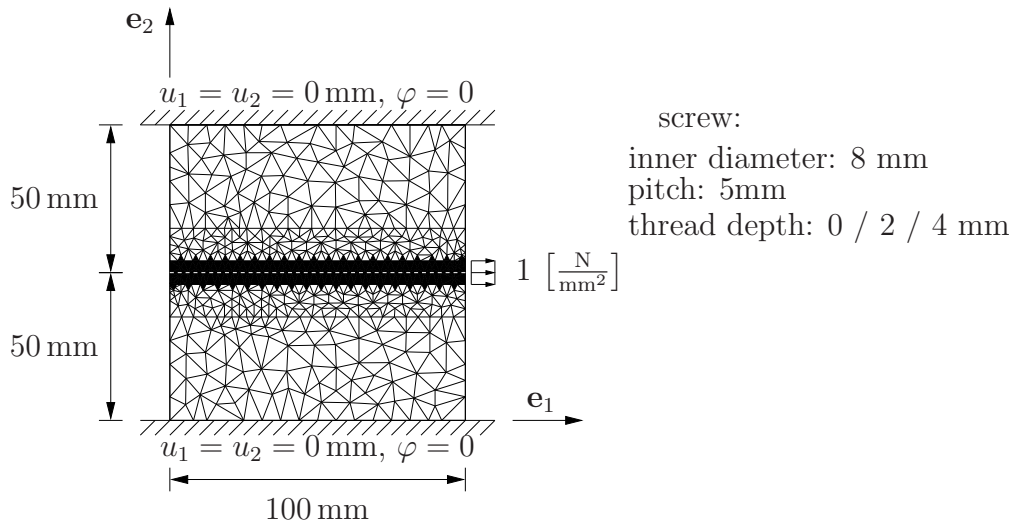


Figure 8.20: Boundary value problem of pull out test

Figure 8.21 shows the respective numerical results. While for the screw without thread (left column) two bands of higher density appear, for the screws with thread (column in the middle and right column) the tips serve as expected as starting points for the formation of bands distributing the

load over a larger width and caring thereby for a more homogeneous load carrying as in the case without thread.

This last example shows the importance of an accurate modeling of the geometry. It is important to include the effects which are responsible for stress peaks but in the same way it is necessary to avoid stress peaks in the model, which are not present in reality, e. g. which result from an insufficient discretization.

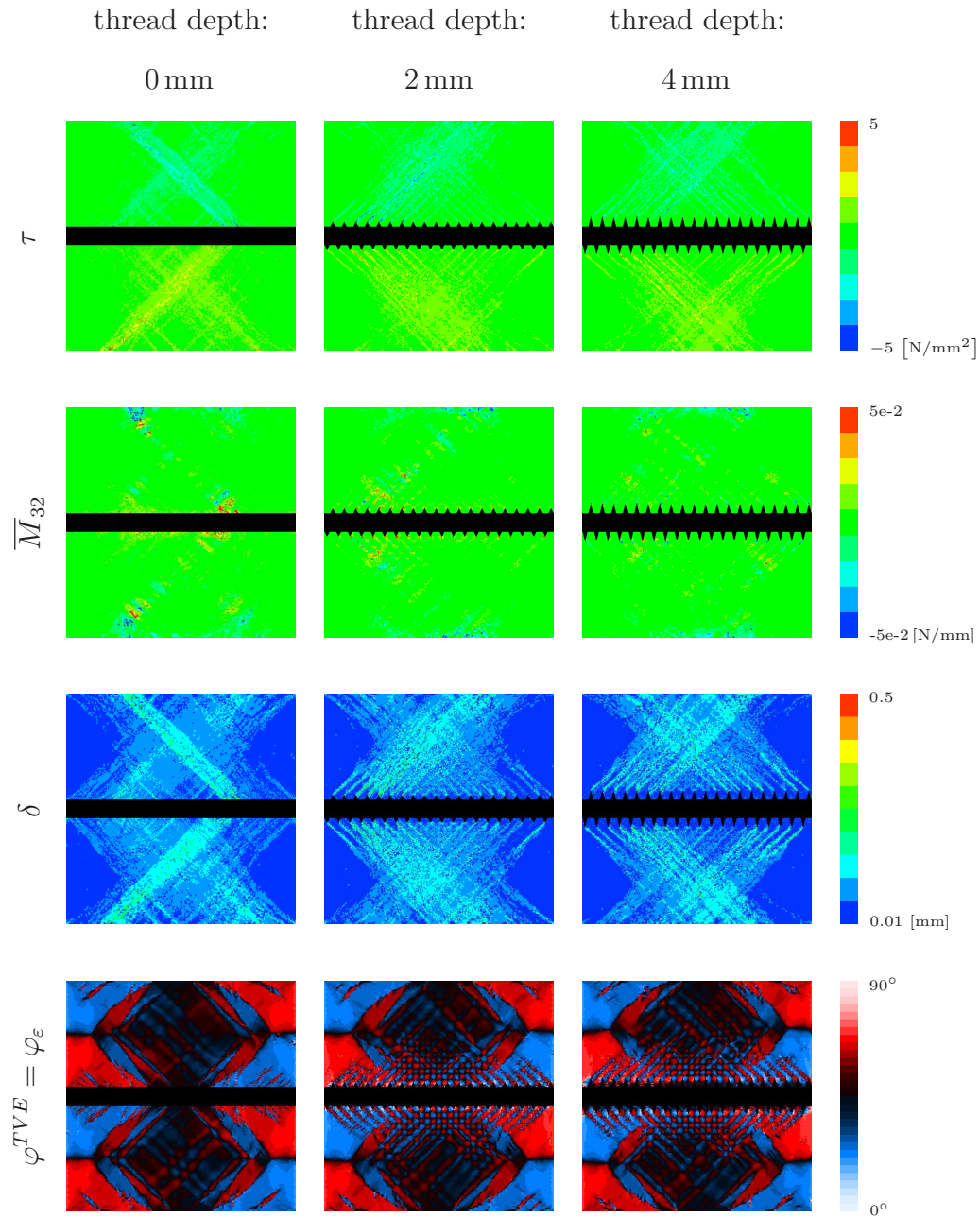


Figure 8.21: Converged solutions for different thread depths

8.2 Numerical examples calculated by LS-DYNA

Four numerical examples are presented demonstrating the reduced capability of the model based on first order homogenization considering the *Cauchy* continuum theory on the macroscopic level. The first example focuses on the reasonability of the adaptation process. The second example checks the presence of a boundary layer and the presence of size effects, respectively. The third example discusses the mesh independency. In the fourth example the model is applied to a simplified model geometry of the femoral head with inserted screw. The numerical examples are followed by a sketch of how to include the CT data into the model.

In principle all examples base on the same set of material parameters. However, the adaptation processes can be switched off independently to discuss effects involved by the FE² approach and effects involved by the formulation of the adaptation process separately. The set of material parameters is presented in table 8.3.

The *Courant-Friedrichs-Lewy* condition [12] postulates that the time step size of the explicit calculation is smaller than a critical time step Δt_{crit}

$$\Delta t_{crit} = \frac{l_{min}}{s}, \quad (8.1)$$

whereby l_{min} is the smallest distance between neighbored points of the discretization and s is the wave propagation velocity, which is given for the three-dimensional continuum by

$$s = \sqrt{\frac{E(1-\nu)}{(1+\nu)(1-2\nu)\rho}} \quad (8.2)$$

Young's modulus	E	100000	$\frac{\text{N}}{\text{mm}^2}$
length	l	1	mm
minimum radius	d_{min}	0.001	mm
maximum radius	d_{max}	0.5	mm
viscous parameter growth	η_1	10000.0	$\frac{\text{N}}{\text{mm}} h$
viscous parameter atrophy	η_2	1.0	mm h
lower bound of dead zone	T_l	400	$\frac{\text{N}}{\text{mm}^2}$
upper bound of dead zone	T_u	500	$\frac{\text{N}}{\text{mm}^2}$
velocity parameter reorientation	c	0.001	$\frac{1}{h}$

Table 8.3: Material parameters (LS-DYNA)

with Young's modulus E , Poisson's ratio ν and specific mass density ρ . However, these effective quantities are never calculated for the TVE. Therefore, the critical time step size is computed using some simplifications. A wave cannot propagate through the TVE faster than through a homogeneous TVE consisting completely of the bulk material. That means that the microscopic Young's modulus E as given in table 8.3 is used for the calculation of the time step size. The effect of the Poisson's ratio is considered by a safety factor f . The effective density can be approximated based on the microscopic density and topology. However, the microscopic density is not used within the FE² approach, and due to the interest in quasi-static solutions the effective density ρ can be chosen in a range, which guarantees that kinematical effects are negligible compared to the quasi-static solution. In other words: increasing the effective density ρ also increases the critical time step size Δt_{crit} , but that also increases the mass inertia so that the converged solution without kinematical effects is reached after the same CPU time.

8.2.1 Check of adaptation process

The first example calculated by LS-DYNA checks the reasonability of the adaptation process, whereby the geometry of the bone-like material is discretized by one single hexahedral element and six tetrahedral elements, respectively. The geometry and the applied boundary conditions are shown in Fig. 8.22. Minimizing dynamical effects, viscoelastic layers are placed on top and bottom of the sample damping out the kinetic energy. These layers are extremely stiff compared to the bone-like material so that the deformation of the layers has no influence on the numerical results of the material under investigation. Furthermore, applying the load a S-shaped scaling function $f(t)$ is used also reducing the amount of kinetic energy. To get a unique solution a triaxial load case is applied to the structure. Applying a uniaxial load case would cause an ambiguous solution, because only one principal direction of the strain tensor can be determined and the other two directions would depend on the numerical errors of the strain tensor components. The circle with included microstructure within Fig. 8.22 shows the used TVE, which is initially rotated around the \mathbf{e}_2 -axis by an angle of 30° .

Fig. 8.24 presents the numerical results of the reorientation. As expected the TVE turns back into the reference position, which is the position where the axes of the TVE are aligned with the coordinate system of the macroscale. All the hexahedral elements under investigation (element formulation 1: constant stress solid element; element formulation 2: fully integrated solid with selective reduced integration; element formulation 18: enhanced strain solid) yield the same result. By contrast the tetrahedral elements (element formulation 10: constant stress tetrahedron) although initially turn back into the required vertically aligned position, but at time $t > 6000$ h the angle increases. At this moment also the rotation axis starts to deviate from the expected rotation axis, which is the \mathbf{e}_2 -direction, the TVE was initially rotated around. Taking a look at Fig. 8.24, which presents the beam radii d_i of the beam elements as well as the according stimuli $T_{eq,i}$, one can see, that the problem occurs when the beam radius d_3 starts to deviate from the other beam radii. Thereby, the initially orthotropic TVE with same stiffness in each principal direction becomes now orthotropic but with different stiffness in the several principal directions. This additional anisotropy in combination with the anisotropy involved by the discretization with six tetrahedral

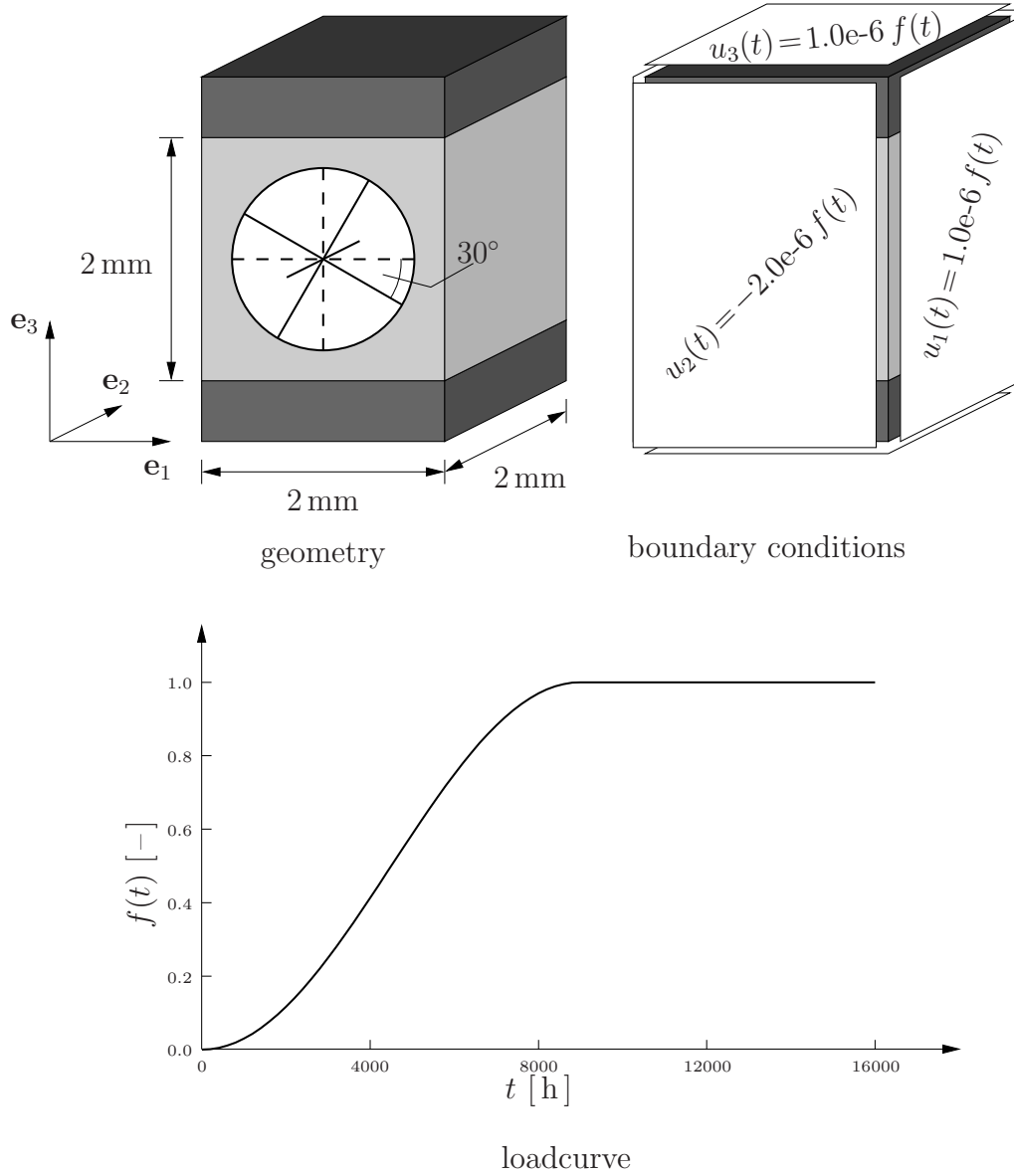


Figure 8.22: Boundary value problem for testing of the adaptation process

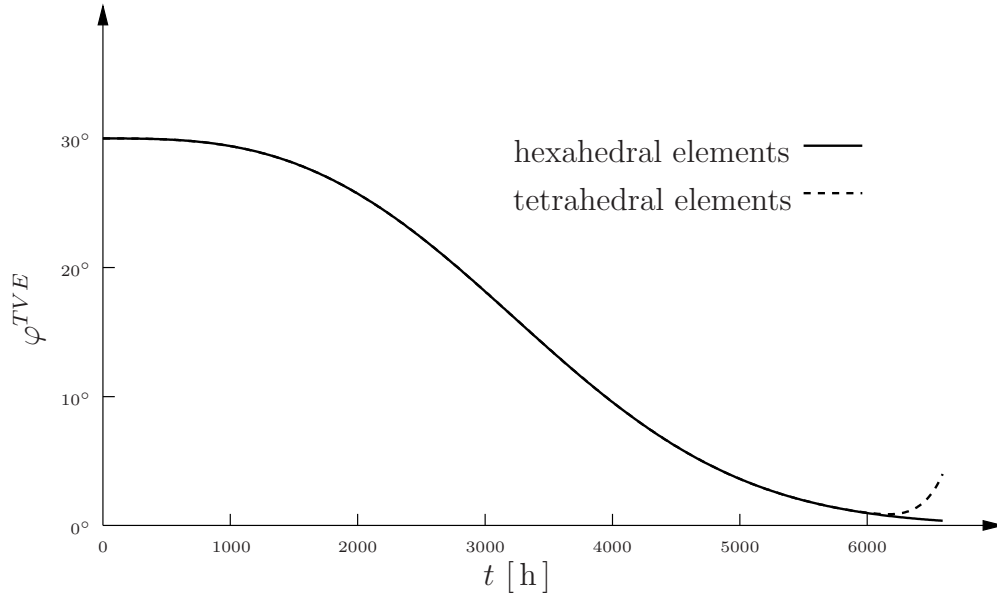


Figure 8.23: Adaptation: reorientation

elements only leads to the undesirable effect for the reorientation. LS-DYNA also provides other tetrahedral elements than the constant stress tetrahedron. However, these elements fail completely due to the bad approximation of the principal strain directions, which depends considerably more on the discretization of the geometry.

The diagrams of Fig. 8.24, showing the beam radii d_i and the according stimuli $T_{eq,i}$, are plotted consciously on top of each other. Thus, it is possible to directly see the influence of the stimulus on the change of the radius. All beam directions have the same initial beam radius of 0.01 mm. At the beginning all stimuli are lower than the lower bound of the dead zone leading to decreasing beam radii, which converge towards the minimum beam radius. Then the stimulus of the third beam axis crosses the dead zone and exceeds the upper bound of the dead zone leading to an increasing beam radius of the third beam direction. Inversely the increasing beam radius leads to a reduction of the according stimulus. The stimulus consists of two parts: a normal stress dependent part and a shear stress dependent part. Applying *Dirichlet*

boundary conditions, the normal stresses due to stretch and compression do not change varying the beam radius. That means that the reduction of the stimulus results from the reduction of the shear stresses at the beam ends, which are reduced by the increased bending stiffness of the according beam elements.

Having in mind the application to real patient specific data, the geometry will normally be approximated by tetrahedral elements provided by a mesh generator. Only one tetrahedral element formulation, the constant stress element formulation, is available. Thus, also for the hexahedral elements only the constant stress formulation is investigated in the following, even it is clear that this will influence the numerical results significantly, especially under shear deformation.

8.2.2 Check of boundary layer effect and size effect

The second example calculated by LS-DYNA investigates the boundary layer effect and the size effect. From a theoretical point of view, the FE² model using FOH should not be able to reflect boundary layer effects due to the underlying *Cauchy* continuum theory, which does not regard an internal length scale. However, that does not mean that size effects are completely excluded. Scaling of the beam length l or of the beam thicknesses d_i can change the relation between tensile stiffness and bending stiffness. When eliminating the change of density involved by scaling of the microscopic geometry parameters an influence on the macroscopic scale can still be observed.

While a boundary layer effect has been observed in the shear experiment using the FE² approach with SOH (Fig. 8.2) a shear experiment is also carried out for the model based on FOH. Taking a look at the cross-like microstructure presented in Fig. 8.11 one can imagine that even for a very small shear deformation the normal stresses in the vertical direction are comparably high due to the strong difference in bending and tensile stiffness of the beam elements. Thus, extremely small deformations are applied in this case. As before in the case of the model using SOH, the adaptation processes are switched off investigating the size effect. Two different orienta-

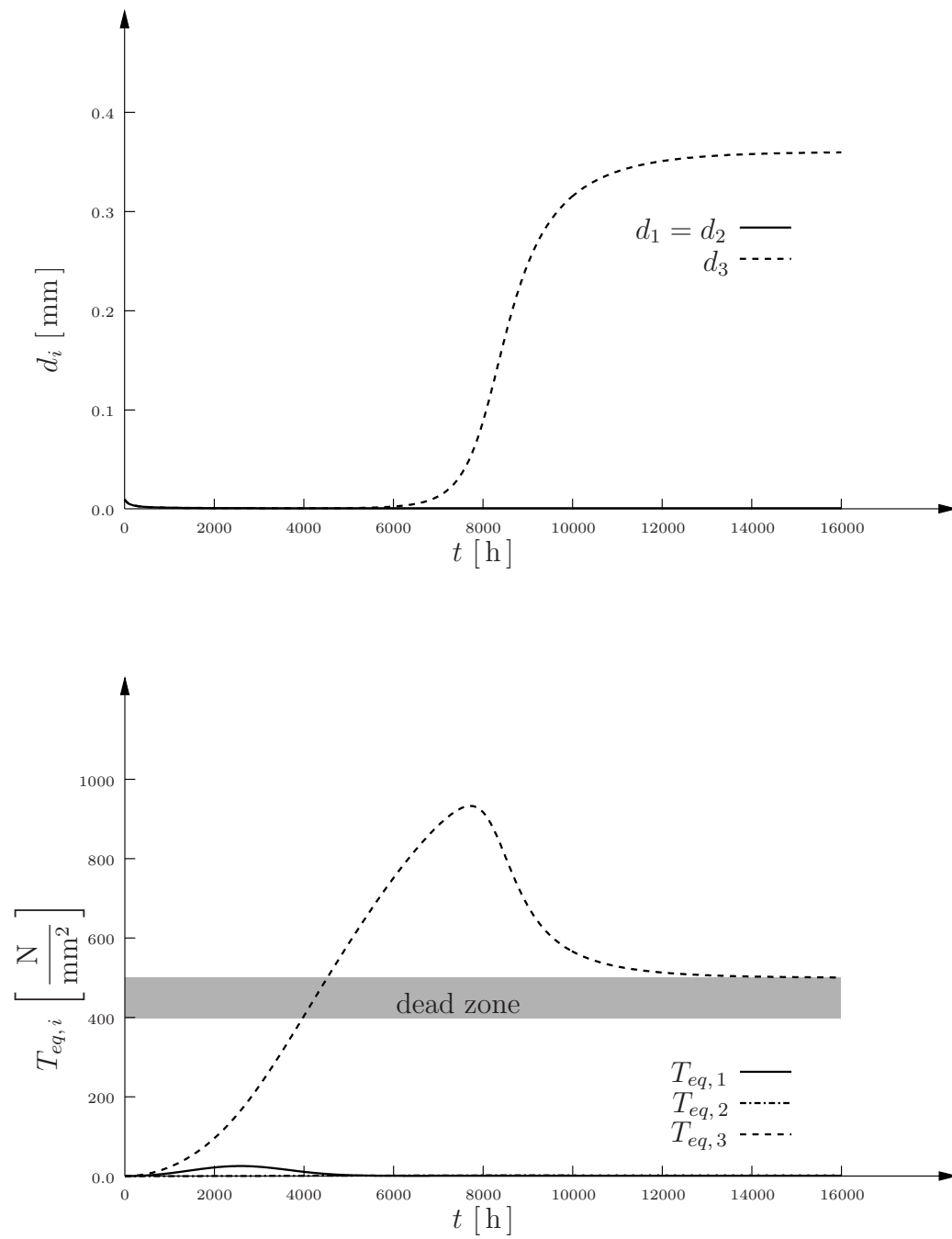


Figure 8.24: Adaptation: thickness change and stimuli

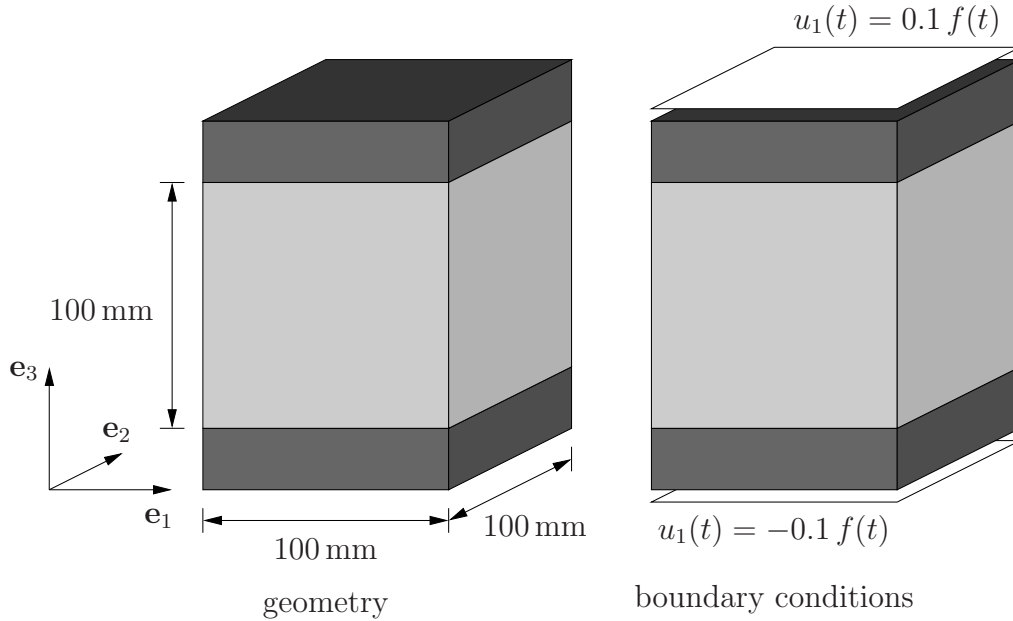


Figure 8.25: Boundary value problem for investigation of size effects

tions of the TVE are investigated, namely an orientation of $\varphi^{TVE} = 0^\circ$ and of $\varphi^{TVE} = 45^\circ$. The rotation axis is aligned with the global \mathbf{e}_2 -direction. The boundary value problem is shown in Fig. 8.25. As before for the previous example comparably stiff viscoelastic layers are placed on top and bottom of the sample damping out the kinetic energy. Furthermore, the same load scale function $f(t)$ is used as for the previous example, see Fig. 8.22.

In a first step the convergence behavior of the shear stresses $T_{13} = T_{31}$ with respect to mesh refinement is investigated for both orientations (table 8.4). For each orientation the actual value of the quasi-static solution is given for the maximum applied load. Furthermore the absolute deviation with respect to the finest discretization under investigation ($25 \times 25 \times 25$) is shown. It is obvious that the microstructural orientation of $\varphi^{TVE} = 45^\circ$ behaves much stiffer regarding the applied load compared to the orientation of $\varphi^{TVE} = 0^\circ$, because the former is the optimal orientation and the latter the worst orientation. When all kinematical effects are damped out, the solution for the shear stresses $T_{13} = T_{31}$ is homogeneous, which means that the effects

of higher order already present for the normal stresses do not influence the results. Using ten elements in each direction for the discretization of the cube, the involved error achieves a tolerable value. This investigation shows the disadvantage of the selected element formulation with only one integration point with respect to shear loading.

discretization	$\varphi^{TVE} = 0^\circ$		$\varphi^{TVE} = 45^\circ$	
	$T_{13} = T_{31}$	deviation	$T_{13} = T_{31}$	deviation
2×2×2	7.419e-7	25.70 %	9.578e-3	23.17 %
4×4×4	6.302e-7	6.78 %	8.309e-3	6.85 %
5×5×5	6.156e-7	4.30 %	8.145e-3	4.74 %
8×8×8	5.996e-7	1.59 %	7.959e-3	2.35 %
10×10×10	5.958e-7	0.95 %	7.915e-3	1.79 %
16×16×16	5.870e-7	0.54 %	7.847e-3	0.91 %
20×20×20	5.909e-7	0.12 %	7.816e-3	0.51 %
25×25×25	5.902e-7	—	7.776e-3	—

Table 8.4: Convergence study

In a second step the effect of scaling the microscopical beam length l and the beam radii d_i is analyzed (Fig. 8.26). Thereby, Λ is the scaling factor of the beam length l and Δ the scaling factor of the beam radii d_i . As before for the two-dimensional model using SOH, three different investigations are carried out for both orientations: scaling of the TVE ($\Lambda = \Delta$), scaling of the beam length by factor Λ ($\Delta = \text{const.}$) and scaling of the beam radii by factor Δ ($\Gamma = \text{const.}$).

As expected, scaling of the TVE has no influence on the homogeneous results of the shear stress component T_{13} for the $\varphi^{TVE} = 0^\circ$ orientation as well as for the $\varphi^{TVE} = 45^\circ$ orientation of the microstructure. As a consequence it follows for the parameter identification that it is not possible to determine the size of the TVE.

Scaling the beam length l by a factor Λ the results decrease by order of four for the $\varphi^{TVE} = 0^\circ$ orientation and by order of two for the $\varphi^{TVE} = 45^\circ$ orientation, which can be seen on the diagram in the middle of Fig. 8.26 using double-logarithmic scale. Eliminating the influence of the involved density

change, the density decreases by order two for increasing beam length, it follows, that for the $\varphi^{TVE} = 0^\circ$ orientation the results finally decrease by order two while the results for the $\varphi^{TVE} = 45^\circ$ orientation are independent of the scaling of the beam length.

The same effect can be observed for the scaling of the beam radii d_i by a factor Δ , see the diagram on bottom of Fig. 8.26. Again if one eliminates the effect of density change involved by increasing the beam radii, the results for the $\varphi^{TVE} = 0^\circ$ now increase by order two while the results for the $\varphi^{TVE} = 45^\circ$ orientation are again independent of the scaling of the beam length.

The effect can be explained by taking a look at Eq. 5.15. If the load is carried only by stretch, as it is the case for the $\varphi^{TVE} = 45^\circ$ orientation, the analytical solution of Eq. 5.15 has the form

$$\langle T_{kl} \rangle_S = \frac{1}{V} \sum_{i=1}^n \gamma_i E A_i \varepsilon_{kl} l = \sum_{i=1}^n \gamma_i E \varepsilon_{kl} \frac{\pi d_i^2}{8 l^2}, \quad (8.3)$$

whereby γ_i is a dimensionless factor independent of the beam length and beam radii. A_i is the cross sectional area of the several beam elements. The analytical solution shows that scaling of the size of the TVE has no influence on the results because the beam length l and the beam radii d_i enter the equation quadratically. Furthermore, scaling of the beam length or beam radii has no influence considering the elimination of the density change.

If the load is carried by bending only, as it is the case for the $\varphi^{TVE} = 0^\circ$ orientation, the analytical solution of Eq. 5.15 has the form

$$\langle T_{kl} \rangle_B = \frac{1}{V} \sum_{i=1}^n \gamma_i \frac{E I_i}{l^2} \varepsilon_{kl} l = \sum_{i=1}^n \gamma_i E \varepsilon_{kl} \frac{\pi d_i^4}{32 l^4}, \quad (8.4)$$

whereby I_i is the moment of inertia of the corresponding beam element. That means that in comparison to Eq. 8.3 the length l and the beam radii d_i enter the equation by fourth order. Thus it follows, that the scaling of the size of

the TVE has no influence on the results. If one increases the radii d_i but keeps the length l constant, the values increase by fourth order. Eliminating again the involved density change, the values still increase quadratically. And vice versa in the case of scaling the beam length l but keeping the radii d_i constant it holds that increasing the beam length, while considering the density change, will lead to quadratically decreasing results.

8.2.3 Check of mesh independency

The second example calculated by LS-DYNA has shown that the results are mesh dependent even if the adaptation process has been switched off. The following example demonstrates that the model is not regularized but mesh dependent also in the formulation of the adaptation processes. That means that e. g. the apparent density of a certain region also depends on the discretization, whereby the differences cannot be explained only by the effect observed in the previous example with homogeneous deformation. The differences rather result from stress peaks at locations where discontinuities are present e. g. due to the applied boundary conditions or due to the change of material. If the stress peaks are smeared over a certain range the resulting effective stimulus does not have the same effect on growth and atrophy as the non-smeared solution. The effect is shown in the boundary value problem presented in Fig. 8.27. Therein the loadcurve $f(t)$ is again an S-shaped function as shown in Fig. 8.22, but it is scaled so that the maximum value (1.0) is already reached at time $t = 90$ h. Considering the symmetry of the boundary value problem, the FE calculation is carried out for a quarter of the structure.

Fig. 8.28 shows the average beam thickness $\langle d_i \rangle$ for three different discretizations at time $t = 40$ h. Relating to the boundary value problem presented in Fig. 8.27 the left rear quarter of the sample is presented.

It is clear that the stress distribution beneath the loading on top can be better approximated by a finer discretization than by a coarser discretization. This also results in a better approximation of the influence on growth and atrophy. Intentionally the results on Fig. 8.28 are plotted as the element val-

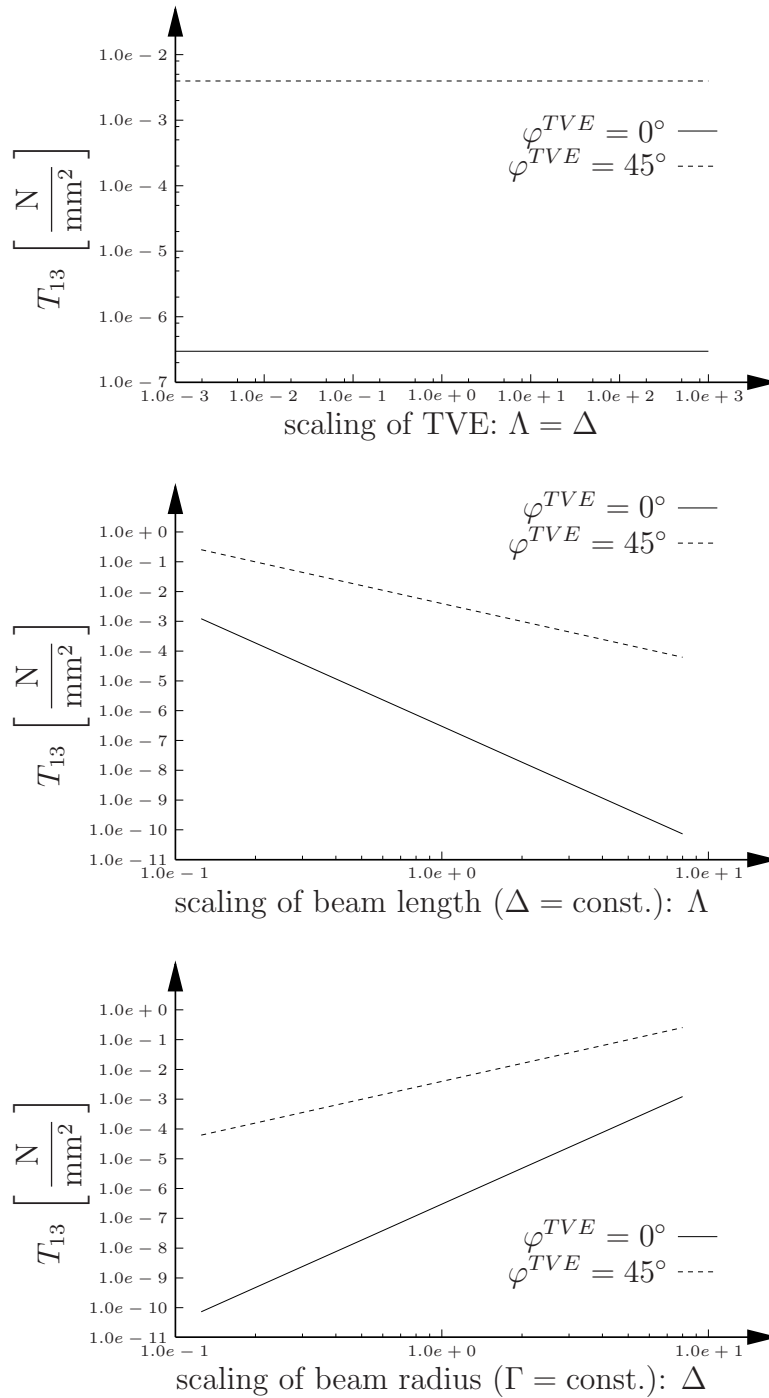


Figure 8.26: Influence of geometrical scaling

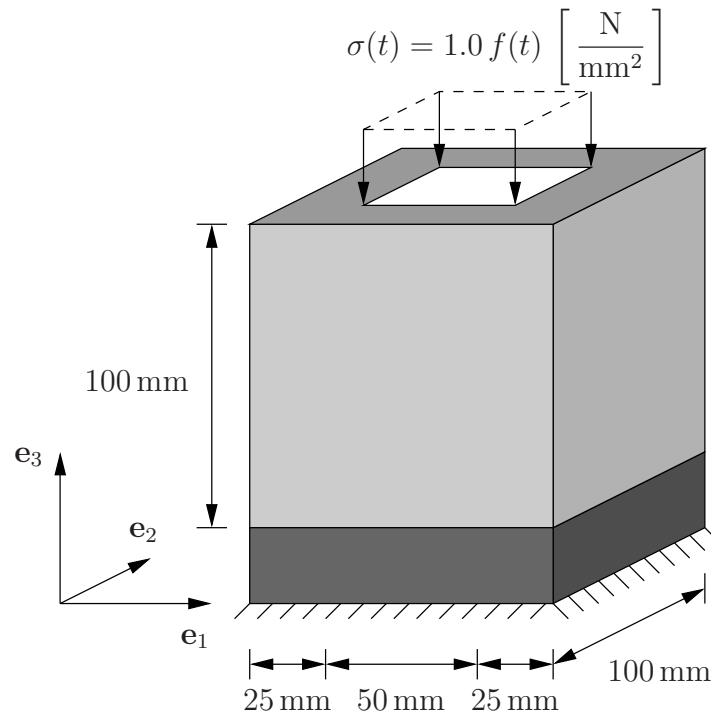


Figure 8.27: Boundary value problem for investigation of size effects

ues without any smoothing. Otherwise the results would seem more similar. While Fig. 8.28 can be interpreted only qualitatively, because a direct comparison of a certain domain is not possible, the average value of the average thickness is calculated for all discretizations. This is done for the cubic domain beneath the loading on top of the sample already marked in Fig. 8.28. The results are presented in Fig. 8.29 plotting the average beam thickness of the domain $\langle d_i \rangle$ over time. At the beginning the stimuli are small so that the beam radii decrease. This is independent of the stimuli so that the beam radii decrease homogeneously for all discretizations under investigation. The differences appear when the stimulus exceeds the upper bound of the dead zone. For a finer discretization this moment is reached earlier due to the better capturing of stress peaks. This effect propagates onward with time so that, in spite of smoothing the effect by division through a larger number of elements for a finer discretization, the average beam thickness for a finer discretization is higher than for a coarser discretization.

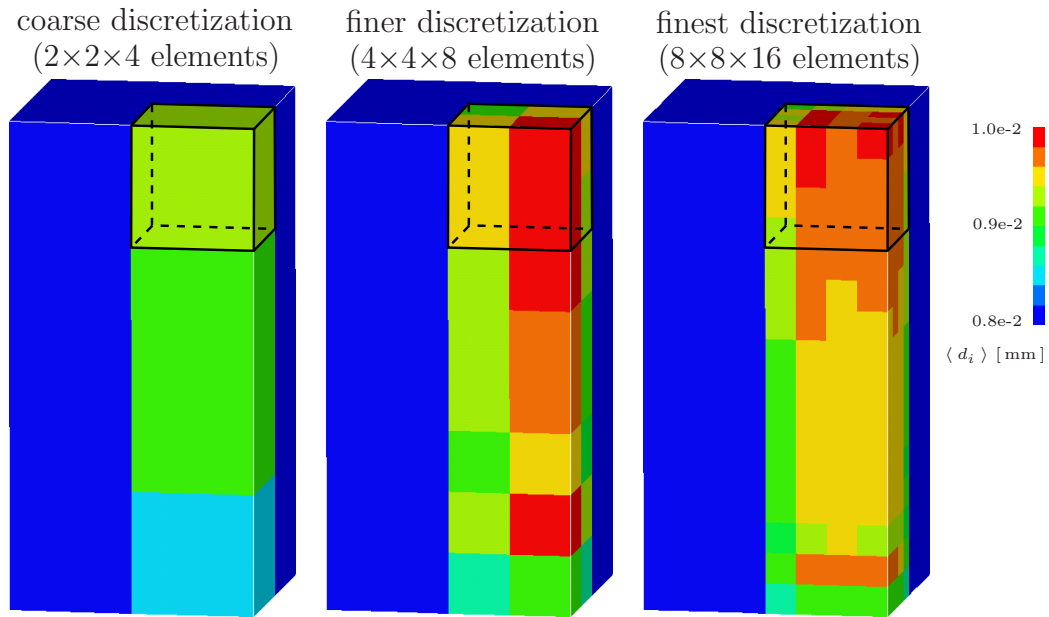


Figure 8.28: Average beam thickness plotted for different discretizations

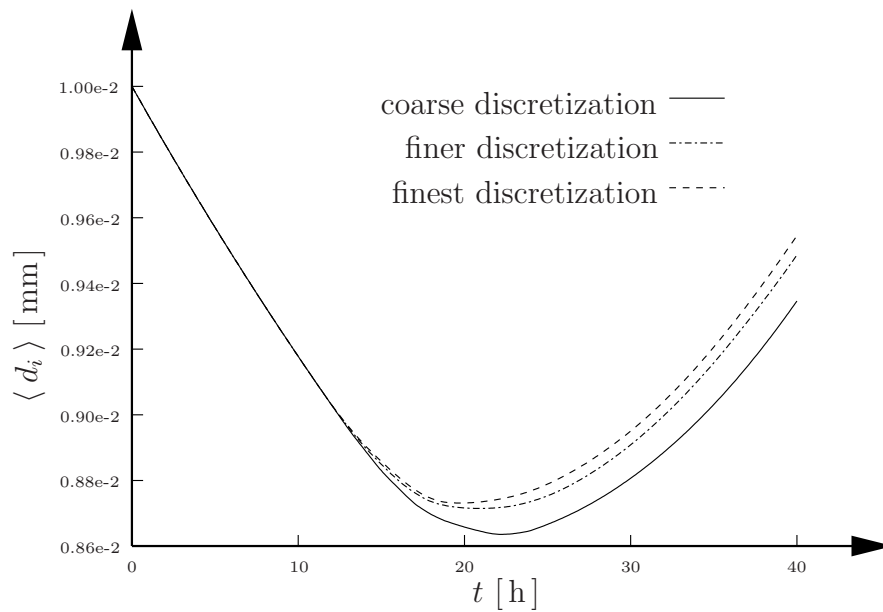


Figure 8.29: Average beam thickness of cubic domain

8.2.4 Application to model geometry

According to the real three-dimensional geometry of the femoral head, the fourth example calculated by LS-DYNA is based upon a simplified geometrical model of the femoral head. Thereby the geometry is approximated by a cylinder representing the spongiosa. The spongiosa is covered by a thin layer of compacta. Furthermore a screw is inserted into the model. The geometry of the rotational symmetric model is shown in Fig. 8.30. The left surface of the compacta is completely fixed and on the right surface of the compacta a constant stress load of $\sigma = 2.387 \text{ N/mm}^2$ is applied corresponding to a resultant force of 3000 N. The femoral head is split into two parts by a cut with the mutable cutting angle α_P . Thus, the model is able to study the differences resulting from different cutting angles as investigated by *Pauwels* [67]. *Pauwels* categorized the fracture of the femoral head into three classes depending on the fracture angle. In case of type 1 fracture only compressive stresses act on the fracture surface. In case of type 3 fracture the surface is loaded mainly by shear stresses. Finally, in case of type 2 fracture the surface is loaded by compressive and shear stresses. The type 1 fracture is good-natured, because the applied load does not lead to a mismatch of the broken femoral head with respect to the rest of the femur. For the other cases the mismatch has to be prevented by nails or screws.

The head of the screw, see e. g. Fig. 8.31, is fixed to the broken femoral head by tied contact. For the other contact areas, the contact between the left femoral part and the screw as well as the contact between the left femoral part and the right femoral part, a penalty-based sliding contact is used (coefficient of static friction $\mu = 0.5$). To get a more realistic loading situation the screw is inserted in a pre-stressed load state ($T_{22} = T_{33} = -0.1 \text{ N/mm}^2$). Thus, compressive stresses act on the contact surface between the screw and the left femoral part, which means that shear stresses too can be transferred at the contact area.

Minimizing the numerical effort for a comparable quality of the results, hexahedral and pentahedral elements are used for the discretization of the geometry. While the spongiosa is loaded mainly by compressive stresses in the horizontal direction (\mathbf{e}_1 -direction), the TVEs are initially aligned with the global coordinate system. That means that the beam radius d_i corresponds

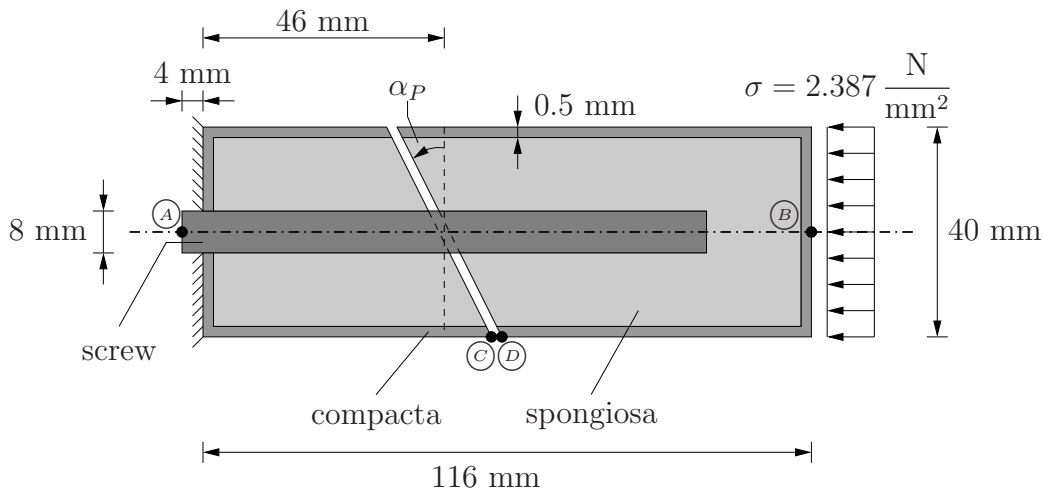


Figure 8.30: Boundary value problem of model geometry

to the beam element initially aligned with the global \mathbf{e}_i -direction. At the beginning all beam elements of the several TVEs have the same radius of $d_i = 0.01$ mm. The kinetic energy is damped out by numerical damping.

Fig. 8.32 shows exemplarily the results for a fracture angle of $\alpha_P = 30^\circ$. The results are presented at time $t = 2000$ h, when the kinetic energy is nearly completely damped out and the adaptation processes came to rest. The several pictures presented therein show the spongiosa only. Taking a look at the normal stresses in horizontal direction T_{11} it is obvious that the compressive stresses are relatively high close to the applied load. Then the load is lead over mainly to the compacta and slightly also to the inserted screw due to their considerably higher stiffnesses. Thus, the rest of the spongiosa is nearly unloaded. This is the well-known effect of stress shielding. Taking a look at the normal stresses in vertical direction T_{22} one can see the influence of stress peaks. Stress peaks appear at edges of the geometry, e. g. at the right end of the screw or at the fracture plane. The higher stresses along the tied contact surface between screw and the right part of spongiosa mainly result from the pre-stressed insertion of the screw. However, it is even pronounced by the external loading. One may argue that the spongiosa participates in load carrying by shear loading. But looking at the *von Mises* equivalent stress

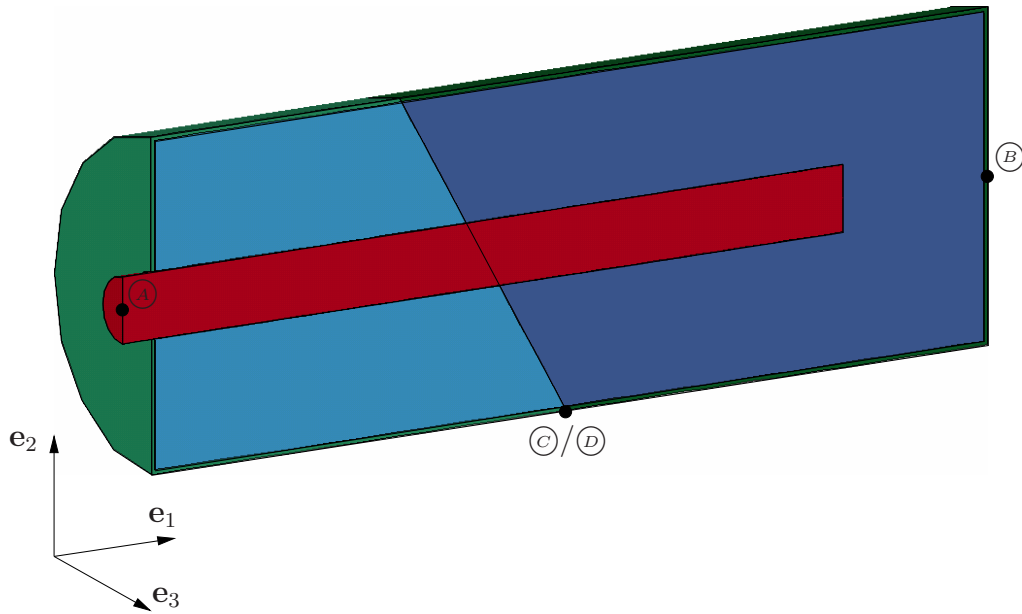


Figure 8.31: Three-dimensional model

T_{eq} demonstrates that the spongiosa located between screw and compacta in radial direction is nearly unloaded except of the effect at the tied contact interface. It is difficult to represent the vector-valued information about the reorientation of the microstructural TVE. Thus, the final orientation of the microstructure is shown in the bottom picture of Fig. 8.32 for five selected elements. Even the loading of the spongiosa is very small between the screw and the compacta in radial direction, the spongiosa is still loaded mainly by normal stresses in horizontal direction. Thus, the change of the orientation relatively small. For very small angles of reorientation $\varphi^{TVE} \ll 1^\circ$ the rotational axes point in arbitrary directions, but for larger angles the rotational axes point at the symmetry plane as expected in the e_3 -direction. From the relatively small rotations it follows that the beam radius d_1 directly corresponds to the normal stress component T_{11} as well as the radius d_2 to the component T_{22} . Furthermore the average of the beam radii $\delta = \langle d_i \rangle$ is presented. The results for the beam radii demonstrate the consequence of stress shielding with respect to the adaptation process. The stress shielding leads to a strong reduction of the density so that the screw loses its footing, which then will lead to failure of the connection between the broken parts.

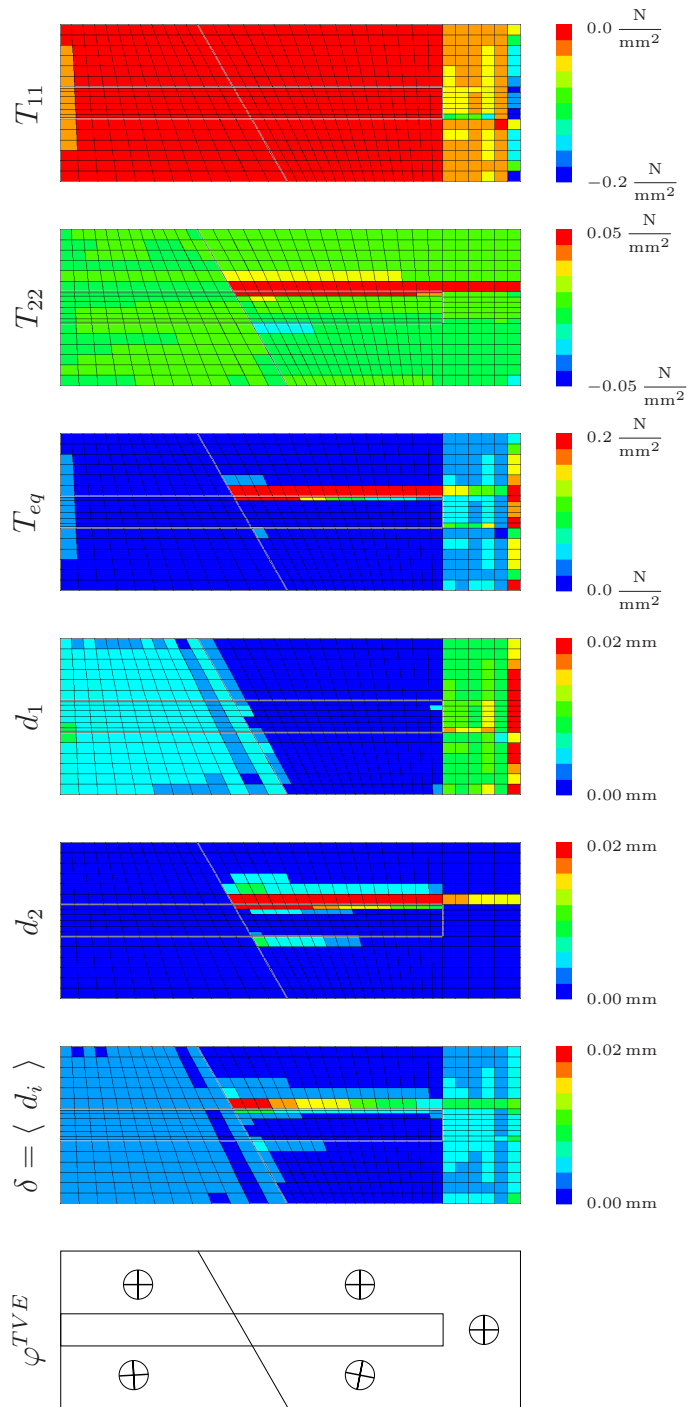


Figure 8.32: Numerical results of model geometry ($\alpha_P = 30^\circ$)

Tabular 8.5 shows a comparison of the displacements of certain points varying the fracture angle α_P again at time $t = 2000$ h. The location of the points is shown in Fig. 8.30 and Fig. 8.31. Point \textcircled{A} is the centerpoint of the left screw end, point \textcircled{B} the centerpoint of the applied load and the points \textcircled{C} and \textcircled{D} are located at the bottom of the fracture plane. Between the points \textcircled{C} and \textcircled{D} there is an initial gap of $1 \mu\text{m}$ in horizontal direction. The horizontal displacements of point \textcircled{A} and point \textcircled{B} are barely influenced by the variation of the fracture angle. However, for the vertical mismatch at the fracture plane the fracture angle has a strong influence. For small fracture angles ($\alpha_P = 0^\circ$ and $\alpha_P = 15^\circ$) the mismatch after the first contact between both parts remains constant, because the shear stresses within the fracture plane are too small for a sliding of the right part. In case of $\alpha_P = 0^\circ$ the value should be zero due to symmetry, but numerical errors result in the value of $-0.3 \mu\text{m}$. The smaller value of $-0.8 \mu\text{m}$ for $\alpha_P = 15^\circ$ results from the prestressed initial state of the screw, which leads to effects in vertical direction due to the non-symmetric tied contact surface between screw and right part of spongiosa. Only in case of $\alpha_P = 30^\circ$ the shear stresses exceed the range of the static friction so that the right part is sliding along the fracture plane in positive \mathbf{e}_2 -direction.

α_P	$u_1^{\textcircled{A}}$	$u_1^{\textcircled{B}}$	$u_2^{\textcircled{D}} - u_2^{\textcircled{C}}$
0°	$-12.8 \mu\text{m}$	$-40.0 \mu\text{m}$	$-0.3 \mu\text{m}$
15°	$-12.1 \mu\text{m}$	$-39.5 \mu\text{m}$	$-0.8 \mu\text{m}$
30°	$-12.3 \mu\text{m}$	$-40.2 \mu\text{m}$	$3.4 \mu\text{m}$

Table 8.5: Displacements in dependency of fracture angle α_P

8.2.5 Sketch of including CT data

In principle the hexahedral mesh derived by interpretation of each voxel as a Finite Element could be used for the numerical simulation. However, the step-like surface of the model would inevitably lead to stress peaks not

present in reality. And while the evolution equation for growth and atrophy is sensitive with respect to such stress peaks, the unnatural stress peaks have to be avoided by an accurate modeling of the surface of the material under consideration. This means that the surface has to be smoothed.

In the present work the hull of the voxel mesh consisting of quadrilateral elements is imported into CATIA. As a start the information about the HU distribution gets lost thereby. Then the surface is smoothed by the algorithms provided by CATIA. After that the domain surrounded by the smoothed hull is meshed by tetrahedral elements. Finally, the distribution of the HU is mapped from the voxel-based hexahedral mesh to the tetrahedral mesh.

For the mapping a very simple algorithm was used. For each tetrahedral element the center of mass is determined. Then it is checked, in which voxel element the center of mass is located. The HU of this element is finally mapped to the tetrahedral element. Of course there exist more advanced mapping algorithms using interpolation functions. But already the initial HU distribution of the voxel mesh is liable to some variation. Thus, improving the mapping algorithm is only reasonable if the tetrahedral discretization is much finer than the hexahedral discretization.

The basic steps of the mapping are shown qualitatively in Fig. 8.33. They are presented for a cut through the femoral head, where the bone material mainly consists of spongiosa and a thin layer of compacta at the boundary, and through the shaft of the femur, where only a thick layer of compacta is present, which surrounds the bone marrow in the inner. The comparison of the HU distribution shows that the information mapped to the tetrahedral mesh can be used as a starting point for the calculation of microscopic material parameters involved in the FE² approach.

According to the quantitative μ CT the osteo calibration and correction factors for the calculation of the bone mineral density (BMD), which depend on the HU distribution, are provided by the manufacturer of the CT device. For the conversion of the BMD into an effective stiffness some relations can be found in literature, see e. g. [17, 71, 72]. A microscopic set of material parameters has to be derived, which is consistent in the sense of having the same effective stiffness. Another possibility is to determine the microscopic

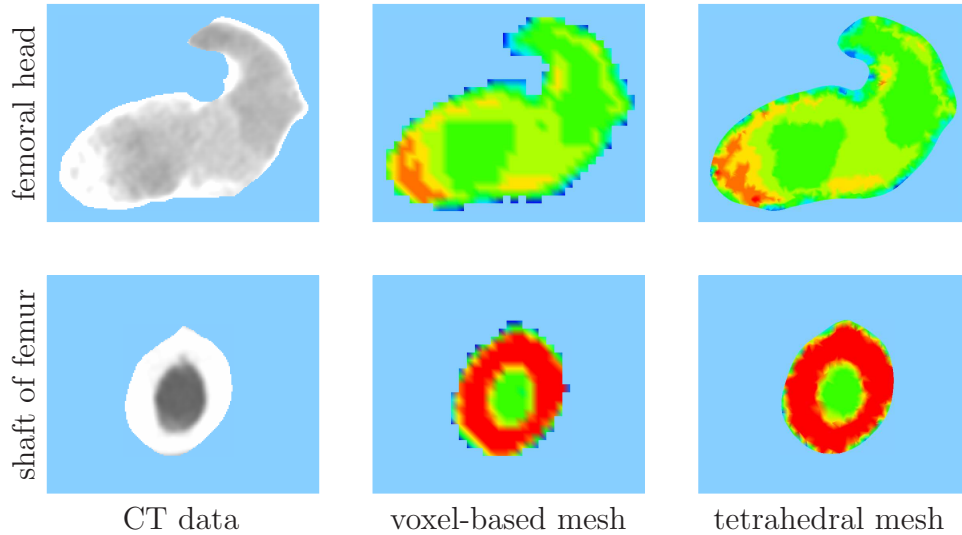


Figure 8.33: Distribution of Hounsfield Unit (HU)

elasticity modulus directly as the elasticity modulus of the hydroxyapatite (see e. g. [37, 48]) so that the BMD is used to determine the microscopic beam radii. However, both approaches assume that the TVE is a reproduction of the real geometry, which is not the case, because it has only to reflect the principal deformation behavior. The relation between microscopic and macroscopic parameters depending on the size and shape of the TVE is still an unsolved question. Thus, the microscopic material parameters may not coincide with the material parameters measured directly on the microscale as mentioned in chapter 6. At last the material parameters have to be determined by parameter identification guaranteeing that the numerical model reflects the actual deformation behavior.

As shown in Fig. 8.34 the present procedure of including CT data is suited for the insertion of implants, screws and nails. When the model is imported into CATIA, they can be inserted by *Boolean* operations. The HU distribution is then mapped to the remaining bone material only.

Numerical simulations for the human femur including CT data are not pre-

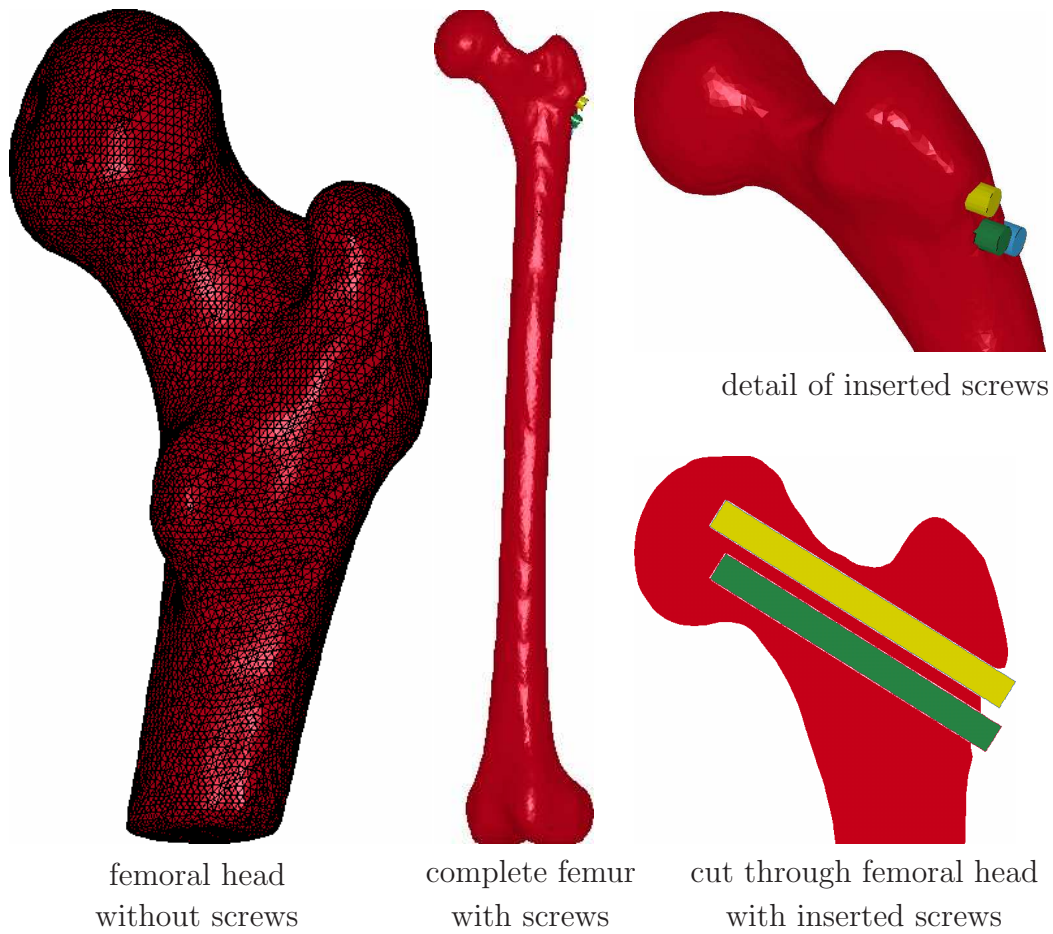


Figure 8.34: FE model of human femur

sented due to the missing parameter identification and the missing accurate loading situations. References to the derivation of accurate loading situations can be found in [30, 56].

Chapter 9

Conclusion

9.1 Summary

This work has focused on the numerical simulation of bone remodeling induced by mechanical loading. The numerical model is based on the FE^2 approach, which combines the advantages of a purely macroscopic continuum model with the advantages of a discrete microscopic model. Macroscopic models are numerically very efficient. However, it is difficult to formulate adequate macroscopic constitutive equations, because the macroscopic effective constitutive relations for remodeling depend not only on the microscopic constitutive equations of the several trabeculae but also on the topology of the trabeculae. Microscopic models are numerically comparatively expensive, but they have the advantage that it is much easier to formulate appropriate constitutive equations. E. g. it is easier to formulate constitutive equations for the several trabeculae instead for a complex arrangement of trabeculae. Thus, combining the advantage of a macroscopic model with the advantage of a microscopic model leads to the FE^2 approach. Within the FE^2 approach the FE calculation is still carried out on a macroscopic level considering the material to be continuous. However, the macroscopic consti-

tutive equations are replaced. This is realized by attaching a microstructure to each macroscopic integration point, the so-called TVE. Then macroscopic strain-like quantities are projected to the boundary of the TVE leading to *Dirichlet* boundary conditions for the TVE. Based on the microscopic topology, material parameters and constitutive equations, the resulting stress-like quantities on the boundary of the TVE can be calculated. Homogenization of these microscopic stress-like quantities yields macroscopic stress-like quantities, which are returned to the integration point. Of course the FE^2 approach reduces the numerical efficiency compared to a purely macroscopic model, but is still more efficient than a microscopic model. Besides the FE^2 approach is well suited for parallelization, because the time-consuming circumvention of macroscopic constitutive equations can be executed in parallel.

Depending on the macroscopic continuum theory forming the basis of the FE^2 approach, a greater or lesser extent of strain-like quantities can be projected on the boundary of the TVE. And also vice versa a greater or lesser extent of homogenized stress-like quantities can be considered on the macroscopic level. This has been demonstrated on the basis of the *Cauchy* continuum and the *Cosserat* continuum. While the *Cauchy* continuum theory only regards the classical strain tensor as strain-like quantity, the *Cosserat* continuum theory in addition regards a strain tensor of higher order, the so-called curvature tensor. The FE^2 approach has been presented for both continuum theories, namely for the *Cauchy* continuum theory using first order homogenization (FOH) and for the *Cosserat* continuum theory using second order homogenization (SOH).

Then the FE^2 model has been extended towards bone remodeling. This has been performed by the formulation of constitutive equations for trabeculae in the inner of the TVE. The constitutive equations describe the adaptation of the TVE with respect to mechanical loading, namely growth and atrophy, considered by increasing or decreasing thickness of the corresponding trabecula, and reorientation, considered by an appropriate rotation of the TVE.

The capability of the model has been demonstrated by numerical examples focusing on the different aspects of interest, e. g. involved size effects and regularization. One set of examples has been computed using the implicit FE code PANDAS. In that case the FE^2 approach has been implemented on the

basis of the *Cosserat* continuum theory applying the second order homogenization. The other set of examples has been computed using the explicit FE code LS-DYNA. Thereby the FE² approach has been implemented based on the *Cauchy* continuum theory using first order homogenization.

The numerical results have shown that the FE² model based on the *Cosserat* continuum theory has several advantages compared to the model based on the *Cauchy* continuum theory. The former is regularized by the *Cosserat* continuum theory leading to mesh-independent results even in the case of remodeling. That does not hold for the latter, which is mesh-dependent. The attached TVE does not have to be representative in a statistical sense, but it has to reflect the principal deformation behavior. Due to the enrichment of the degrees of freedom in case of the *Cosserat* continuum theory by an independent rotational field, the TVE can reflect more deformation modes than in the case of the *Cauchy* continuum theory. Thus, the former can approximate much better the deformation of the TVE and is therefore also able to reflect boundary layer effects and size effects, which is not possible for the latter. From this it follows that the FE² model based on the *Cosserat* continuum theory offers interesting possibilities to extend the constitutive equations depending on quantities being present at the boundary layers. E. g. this enables the consideration of effects at the intersection between screw and bone material. Finally, compared to the classical *Cosserat* model, this model has the advantage that the thickness of the boundary layer and the absolute value at the boundary of the according quantity is driven by two independent material parameters. Thus, when performing a parameter identification it should be easier to approximate the boundary layer effect accurately by adjusting these two parameters, which may be interpreted as internal length scales, than by the single internal length scale provided by the classical *Cosserat* continuum theory. However, also the much simpler FE² approach based on the *Cauchy* continuum theory has its respective merits. Assuming the same discretization for both models, the simpler model is numerically more efficient due to the lower number of degrees of freedom. As long as one is not interested in any boundary layer effects or size effects it yields reasonable results, which may be sufficient for a large number of applications. Furthermore the simpler model has the advantage of being implementable into each FE code providing an user material interface. The more complex model based on the *Cosserat* continuum theory requires the access to the balance of moment of momentum, which is not provided by all

FE codes.

As shown by the analytical investigations the model has to be understood as a phenomenological one due to the involved simplifications. That means that the microstructural parameters, which describe the topology of the TVE and which are determined by parameter identification, do not have to represent the actual topology of the trabecular microstructure.

9.2 Future work

Having in mind the application of the model to the workaday surgery of the femoral neck fracture, a parameter identification has to be carried out. This has to be followed by a validation of the model comparing the numerical results to experimental data. For this purpose it is possible to identify the parameters step by step. In a first step the microstructural parameters can be identified by ignoring the adaptation processes. In a second step the bounds of the dead zone can be identified by ignoring the timescale. Finally the time-dependent parameters can be adjusted.

If the model is adjusted to a realistic time scale, the constitutive equations for growth and atrophy can be enhanced including dynamical effects. This is necessary because experimental data show that applying a quasi-static load, representing the average loading of the material, has not the same influence on growth and atrophy as applying the real dynamical loading situation.

Utilizing the model in clinical application it should be numerically as efficient as possible but it should still fulfill certain requirements like mesh-independency. The FE^2 model based on the *Cosserat* continuum theory fulfills these conditions. However, compared to the FE^2 model based on the *Cauchy* continuum theory it already introduces a vector-valued independent variable, which is the rotational field. Thus, one should investigate FE^2 models getting by with only one additional scalar-valued degree of freedom, e. g. the order parameter model or the pure microstretch model. The pure microstretch model can be derived in analogy to the *Cosserat* continuum

theory by the assumption that the attached directors may uniformly change their length but not their orientation.

Bibliography

- [1] AŞKAR, A. [1986]. *Lattice dynamical foundations of continuum theories*. World Scientific Publication, Singapore.
- [2] AŞKAR, A. & A. ÇAKMAK [1968]. ‘A structural model of a micropolar continuum.’ *Int. J. Engng. Sci.*, **6**, pp. 583–589.
- [3] ADACHI, T., Y. TOMITA & M. TANAKA [1999]. ‘Three-dimensional lattice continuum model of cancellous bone for structural and remodeling simulation.’ *JSME International Journal*, **42**(3), pp. 470–480.
- [4] ADACHI, T., K. TSUBOTA, Y. TOMITA & S. J. HOLLISTER [2001]. ‘Trabecular surface remodeling simulation for cancellous bone using microstructural voxel finite element models.’ *ASME J. Biomech. Engrg.*, **123**, pp. 403–409.
- [5] BAKER, S. [2003]. ‘A surgeon whose hands never shake.’ *Business Week Online*, **4**.
- [6] BARDET, J. & I. VARDOULAKIS [2001]. ‘The asymetry of stress in granular media.’ *Int. J. Solids Structures*, **38**, pp. 353–367.
- [7] BEAUPRE, G., T. ORR & D. CARTER [1990]. ‘An approach for time-dependent bone modeling and remodeling - Application: a preliminary remodeling simulation.’ *J. Orthop. Res.*, **8**, pp. 662–670.
- [8] BEAUPRE, G., T. ORR & D. CARTER [1990]. ‘An approach for time-dependent bone modeling and remodeling - Theoretical development.’ *J. Orthop. Res.*, **8**, pp. 651–661.

- [9] BRAESS, D. [1997]. *Finite element methods*. Cambridge University Press, Cambridge.
- [10] CARTER, D. & G. BEAUPRE [2001]. *Skeletal Function and Form: mechanobiology of skeletal development, aging and regeneration*. Cambridge University Press, Cambridge.
- [11] COSSERAT, E. & F. COSSERAT [1909]. *Théorie des corps déformables*. A. Hermann et Fils, Paris.
- [12] COURANT, R., K. FRIEDRICHS & H. LEWY [1928]. ‘Über die partiellen Differenzengleichungen der mathematischen Physik.’ *Math. Ann.*, **100**, pp. 32–74.
- [13] COWIN, S. [2006]. ‘On the modeling of growth and adaptation.’ In *Mechanics of Biological Tissues*, edited by G. A. Holzapfel & R. W. Ogden, pp. 29–46. Springer-Verlag, Berlin.
- [14] COWIN, S. & D. HEGEDUS [1976]. ‘Bone remodeling I: Theory of adaptive elasticity.’ *J. Elasticity*, **6**, pp. 313–326.
- [15] COWIN, S. & R. NACHLINGER [1978]. ‘Bone remodeling III: Uniqueness and stability in adaptive elasticity.’ *J. Elasticity*, **8**, pp. 285–295.
- [16] CULMANN, C. [1866]. *Die graphische Statik*. Meyer & Zeller, Zürich.
- [17] CURREY, J. [1969]. ‘The relationship between the stiffness and the mineral content of bone.’ *J. Biomech.*, **2**, pp. 477–480.
- [18] DIEBELS, S. & W. EHLERS [2001]. ‘Homogenization method for granular assemblies.’ In *Proceedings of ‘Trends in Computational Structural Mechanics’*, edited by W. Wall, K.-U. Bletzinger & K. Schweizerhof, pp. 79–88. CIMNE, Barcelona, Spain.
- [19] DIEBELS, S. & H. STEEB [2002]. ‘The size effect in foams and its theoretical and numerical investigation.’ *Proc. R. Soc. Lond. A*, **458**, pp. 2869–2883.
- [20] DIEBELS, S. & H. STEEB [2003]. ‘Stress and couple stress in foams.’ *Comp. Mat. Science*, **28**, pp. 714–722.

- [21] EBINGER, T., H. STEEB & S. DIEBELS [2004]. ‘Modeling macroscopic extended continua with the aid of numerical homogenization schemes.’ *Comp. Mat. Science*, **32**, pp. 337–347.
- [22] EBINGER, T., H. STEEB & S. DIEBELS [2005]. ‘Modeling and homogenization of foams.’ *Comp. Assisted Mechanics and Engineering Sciences*, **12**, pp. 49–63.
- [23] EHLERS, W. & P. ELLSIEPEN [1998]. ‘PANDAS: Ein FE-System zur Simulation von Sonderproblemen der Bodenmechanik.’ In *Finite Elemente in der Baupraxis: Modellierung, Berechnung und Konstruktion, Beiträge zur Tagung FEM ’98 an der TU Darmstadt am 5. und 6. März 1998*, edited by P. Wriggers, U. Meißner, E. Stein & W. Wunderlich, pp. 431–400. Ernst & Sohn, Berlin.
- [24] EHLERS, W., E. RAMM, S. DIEBELS & G. A. D’ADDETTA [2003]. ‘From particle ensembles to Cosserat continua: Homogenization of contact forces towards stresses and couple stresses.’ *Int. J. Solids Structures*, **40**, pp. 6681–6702.
- [25] ERINGEN, A. & E. SUHUBI [1964]. ‘Nonlinear theory of simple micro-elastic solids - I.’ *Int. J. Engng. Sci.*, **2**, pp. 189–203.
- [26] ERINGEN, C. [1972]. ‘Nonlocal polar elastic continua.’ *Int. J. Engng. Sci.*, **10**, pp. 1–16.
- [27] ERINGEN, C. [1976]. *Polar and Nonlocal Field Theories*, volume IV of *Continuum Physics*. Academic Press, Boston-New York.
- [28] ERINGEN, C. [1999]. *Microcontinuum Field Theories, Vol. I: Foundations and Solids*. Springer-Verlag, Berlin.
- [29] FEYEL, F. & J. CHABOCHE [2000]. ‘FE² multiscale approach for modelling the elastoviscoplastic behaviour of long fiber SiC/Ti composite materials.’ *Comp. Meth. Appl. Mech. Eng.*, **183**, pp. 309–330.
- [30] FISCHER, K., C. JACOBS & R. CARTER [1995]. ‘Computational method for determination of bone and joint loads using bone density distributions.’ *J. Biomech.*, **28**, pp. 1127–1135.
- [31] FOREST, S. [1998]. ‘Mechanics of generalized continua: Construction by homogenization.’ *J. Phys. IV*, pp. 39–48.

- [32] FOREST, S. & K. SAB [1998]. ‘Cosserat overall modeling of heterogeneous materials.’ *Mech. Res. Commun.*, **25**, pp. 449–454.
- [33] FROST, H. [1964]. ‘Dynamics of bone remodeling.’ In *Bone Biodynamics*, edited by H. Frost, p. 316. Little and Brown, New York.
- [34] FROST, H. M. [2003]. ‘Bone’s mechanostat: A 2003 update.’ *Anatomical Record - Part A Discoveries in Molecular, Cellular, and Evolutionary Biology*, **275**, pp. 1081–1101.
- [35] GEERS, M., V. KOUZNETSOVA & W. BREKELMANS [2003]. ‘Multi-scale first-order and second-order computational homogenization of microstructures towards continua.’ *Int. J. of Multiscale Computational Engineering*. in press.
- [36] GIBSON, L. & M. ASHBY [1997]. *Cellular solids. Structure and properties*. Cambridge Solid State Science Series. Cambridge University Press, Cambridge.
- [37] GILMORE, R. & J. KATZ [1982]. ‘Elastic properties of apatites.’ *J. Mat. Sci.*, **17**, pp. 1131–1141.
- [38] GOLDSTEIN, S. A. [1987]. ‘The mechanical properties of trabecular bone: dependence on anatomical location and function.’ *J. Biomech.*, **20**, pp. 1055–1061.
- [39] GOULET, R. W., S. A. GOLDSTEIN, M. J. CIARELLI, J. L. KUHN, M. B. BROWN & L. A. FELDKAMP [1994]. ‘The relationship between the structural and mechanical properties of trabecular bone.’ *J. Biomech.*, **27**, pp. 375–389.
- [40] HALLQUIST, J. O. [1998]. *LS-DYNA theoretical manual*. LSTC, Livermore.
- [41] HART, R. [2001]. ‘Bone modeling and remodeling: Theories and computation.’ In *Bone Mechanics Handbook*, edited by S. Cowin. CRC Press.
- [42] HEGEDUS, D. & S. COWIN [1976]. ‘Bone remodeling II: Small strain adaptive elasticity.’ *J. Elasticity*, **6**, pp. 337–352.
- [43] HILL, R. [1963]. ‘Elastic properties of reinforced solids: Some theoretical principles.’ *J. Mech. Phys. Solids*, **11**, pp. 357–372.

- [44] HOHE, J. & W. BECKER [2001]. ‘An energetic homogenisation procedure for the elastic properties of general cellular sandwich cores.’ *Composites: Part B*, **32**, pp. 185–197.
- [45] HOLLISTER, S. J., D. P. FYRHIE, K. J. JEPSEN & S. A. GOLDSTEIN [1991]. ‘Application of homogenization theory to the study of trabecular bone mechanics.’ *J. Biomech.*, **24**, pp. 825–839.
- [46] HUET, C. [1997]. ‘An integrated micromechanics and statistical continuum thermodynamics approach for studying the fracture behaviour of microcracked heterogeneous materials with delayed response.’ *Eng. Fracture Mech.*, **58**, pp. 459–556.
- [47] HUISKES, R., R. RUIMERMAN, G. VAN LENTHE & J. JANSSEN [2000]. ‘Effects of mechanical forces on maintenance and adaptation of form in trabecular bone.’ *Nature*, **405**, pp. 704–706.
- [48] KATZ, J. & K. UKRAINCİK [1971]. ‘On the anisotropic elastic properties of hydroxyapatite.’ *J. Biomech.*, **4**, pp. 221–227.
- [49] KOUZNETSOVA, V., W. BREKELMANS & F. BAAIJENS [2001]. ‘An approach to micro-macro modeling of heterogeneous materials.’ *Comp. Mech.*, 37–48.
- [50] KUHL, E. [2004]. *Theory and numerics of open system continuum thermodynamics – spatial and material settings*. Habilitation-thesis, Chair of Applied Mechanics, Technical University of Kaiserslautern.
- [51] KUHL, E. & P. STEINMANN [2003]. ‘Theory and numerics of geometrically non-linear open system mechanics.’ *Int. J. Numer. Meth. Engng.*, **58**, pp. 1593–1615.
- [52] KUMMER, B. [2005]. *Biomechanik: Form und Funktion des Bewegungsapparates*. Deutscher Ärzte-Verlag, Köln.
- [53] LAKES, R. [1995]. ‘Experimental methods for study of Cosserat elastic solids and other generalized elastic continua.’ In *Continuum methods for Materials with microstructures*, edited by H. Mühlhaus, pp. 1–25. John Wiley & Sons, Chichester.

- [54] LARSSON, R. & S. DIEBELS [2007]. ‘A second-order homogenization procedure for multi-scale analysis based on micropolar kinematics.’ *Int. J. Numer. Meth. Fluids*, **69**, pp. 2485–2512.
- [55] VAN LENTHE, G., M. STAUBER & R. MÜLLER [2006]. ‘Specimen-specific beam models for fast and accurate prediction of human trabecular bone mechanical properties.’ *Bone*, **39**, pp. 1182–1189.
- [56] LUTZ, A. & U. NACKENHORST [2007]. ‘Computation of static-equivalent load sets for bone remodeling simulation.’ *Proc. Appl. Math. Mech.*, **7**, pp. 4020007–4020008.
- [57] MARTIN, R. & D. BURR [1989]. *Structure, Function, and Adaptation of Compact Bone*. Raven Press, New York.
- [58] MENZEL, A. [2005]. ‘Modelling of anisotropic growth in biological tissues: A new approach and computational aspects.’ *Biomechan. Model. Mechanobiol.*, **3**, pp. 147–171.
- [59] MENZEL, A. [2006]. ‘Anisotropic remodelling of biological tissues.’ In *Mechanics of Biological Tissues*, edited by G. A. Holzapfel & R. W. Ogden, pp. 91–104. Springer-Verlag, Berlin.
- [60] VON MEYER, G. H. [1867]. ‘Die Architektur der Spongiosa.’ *Archiv für Anatomie, Physiologie und wissenschaftliche Medizin, Reichert und DuBois-Reymonds Archiv*, **34**, pp. 615–628.
- [61] MULLENDER, M. & R. HUISKES [1995]. ‘Proposal for the regulatory mechanism of Wolff’s law.’ *J. Orthop. Res.*, **13**, pp. 503–512.
- [62] NACKENHORST, U. [1997]. ‘Numerical simulation of stress stimulated bone remodeling.’ *Technische Mechanik*, **17**, pp. 31–40.
- [63] NAUENBERG, T., M. BOUXSEIN, B. MIKIĆ & D. CARTER [1993]. ‘Using clinical data to improve computational bone remodeling theory.’ *Trans. Orthop. Res. Soc.*, **18**, pp. 123.
- [64] ONCK, P. [2003]. ‘Scale effects in cellular metals.’ *MRS Bulletin*, **28**, pp. 279–283.
- [65] ONCK, P., E. ANDREWS & L. GIBSON [2001]. ‘Size effects in ductile cellular solids. Part I: modeling.’ *Int. J. Mech. Sci.*, **43**, pp. 681–699.

- [66] PAPKA, S. & S. KYRIAKIDES [1998]. ‘Experiments and full-scale numerical simulations of in-plane crushing of a honeycomb.’ *Acta Mater.*, **46**, pp. 2765–2776.
- [67] PAUWELS, F. [1965]. *Gesammelte Abhandlungen zur funktionellen Anatomie des Bewegungsapparates*. Springer-Verlag, Berlin.
- [68] PETTERMANN, H. E., T. J. REITER & F. G. RAMMERSTORFER [1997]. ‘Computational simulation of internal bone remodeling.’ *Archives of Computational Methods in Engineering*, **4**, pp. 295–323.
- [69] PISTOIA, W., B. VAN RIETBERGEN, A. LAIB & P. RÜEGSEGGER [2001]. ‘High-resolution three-dimensional-pqct images can be an adequate basis for in-vivo μ fe analysis of bone.’ *ASME J. Biomech. Engrg.*, **123**, pp. 176–183.
- [70] POTHUAUD, L., B. VAN RIETBERGEN, C. CHARLOT, E. OZHINSKY & S. MAJUMDAR [2004]. ‘A new computational efficient approach for trabecular bone analysis using beam models generated with skeletonized graph technique.’ *Comput. Meth. Biomech. Biomed. Eng.*, **7**, pp. 205–213.
- [71] RHO, J., R. ASHMAN & C. TURNER [1993]. ‘Youngs modulus of trabecular and cortical bone material: ultrasonic and microtensile measurements.’ *J. Biomech.*, **26**, pp. 111–119.
- [72] RHO, J., M. HOBATHO & R. ASHMAN [1995]. ‘Relations of mechanical properties to density and CT numbers in human bone.’ *Med. Eng. Phys.*, **17**, pp. 347–355.
- [73] ROUX, W. [1881]. *Der Kampf der Teile im Organismus*. Engelmann, Leipzig.
- [74] RUIMERMAN, R., P. HILBERS, B. VAN RIETBERGEN & R. HUISKES [2005]. ‘A theoretical framework for strain-related trabecular bone maintenance and adaptation.’ *J. Biomech.*, **38**, pp. 931–941.
- [75] SANCHEZ-PALENCIA, E. [1980]. *Non-Homogeneous Media and Vibration Theory*. Springer-Verlag, Berlin.

- [76] STAUBER, M., M. HUBER, G. VAN LENTHE, S. BOYD & R. MÜLLER [2004]. ‘A finite element beam-model for efficient simulation of large-scale porous structures.’ *Comput. Meth. Biomech. Biomed. Eng.*, **7**, pp. 9–16.
- [77] TABER, L. [1995]. ‘Biomechanics of growth, remodeling, and morphogenesis.’ *Appl. Mech. Rev.*, **48**, pp. 487–545.
- [78] TEKOGU, C. & P. ONCK [2008]. ‘Size effects in two-dimensional Voronoi foams: A comparison between generalized continua and discrete models.’ *JMPS*, **56**, pp. 3541–3564.
- [79] WARREN, W. & E. BYSKOV [2002]. ‘Three-field symmetry restrictions on two-dimensional micropolar materials.’ *Eur. J. Mech., A/Solids*, **21**, pp. 779–792.
- [80] WOLFF, J. [1892]. *Das Gesetz der Transformation der Knochen*. Hirschwald Verlag, Berlin.
- [81] ZYSSET, P. & L. RINCÓN [2006]. ‘An alternative fabric-based yield and failure criterion for trabecular bone.’ In *Mechanics of Biological Tissues*, edited by G. A. Holzapfel & R. W. Ogden, pp. 457–470. Springer-Verlag, Berlin.